Temperature-Controlled Transient Absorption Spectroscopy and Its Applications

PhD Dissertation

Krisztina Sárosi

Supervisors:

Dr. Viktor Chikán, LIS Technologies Inc., Oak Ridge, TN, USA

Dr. Gergely F. Samu, ELI ALPS, University of Szeged

Doctoral School of Physics

Faculty of Science and Informatics, University of Szeged

Szeged, 2025

Table of Contents

Frequently used acronyms and chemical formulas

TAS	transient absorption spectroscopy
QDs	quantum dots
CPA	chirped pulse amplification
VB	valence band
CB	conduction band
SHG	second harmonic generation
SFG	sum frequency generation
DFG	difference frequency generation
FWM	four-wave mixing
SPM	self-phase modulation
NA	numerical aperture
BBO	β-barium borate
GSB	ground-state bleach
IA	induced absorption
SE	stimulated emission
UV	ultraviolet radiation
IR	infrared radiation
Vis	visible radiation
Yb:YAG	ytterbium-doped yttrium aluminum garnet
XFELs	X-ray free-electron lasers
XUV	extreme ultraviolet
HHG	high harmonic generation
ATAS	attosecond transient absorption spectroscopy
CdSe	cadmium selenide
ZnS	zinc sulfide
ASE	amplified spontaneous emission
TMDs	transition metal dichalcogenides
PL	photoluminescence
2DES	two-dimensional electronic spectroscopy
NIR	near-infrared radiation
HR-TEM	high-resolution transmission electron microscopy
PLQY	photoluminescence quantum yield

1. Introduction

1.1 Theoretical concepts of transient absorption spectroscopy

1.1.1 The ultrasmall and ultrafast story: a brief historical overview

According to J. P. Dowling and G. J. Milburn[1], we are witnessing a second quantum revolution. This is distinguished from the first by a paradigm shift from understanding to applying quantum mechanics to engineering and manipulating material properties and technologies. Indicating the importance of this field of research, the 2023 Nobel Prize in Chemistry was awarded to Moungi G. Bawendi, Louis E. Brus, and Alexei I. Ekimov[2,3] for their pioneering work in synthesizing and characterizing quantum-confined systems, i.e. quantum dots (QDs).

Focusing on lasers[4], the groundbreaking work of James C. Maxwell on electromagnetic radiation in the late 19th century laid the foundations for the laser technology of the 20th century, from Albert Michelson's interferometer[5] (measurement of the speed of light) to Albert Einstein's theory of stimulated emission[6]. The demonstration of the first functioning laser was a crucial milestone by Theodore Maiman[7] in 1960. High-intensity, ultrashort laser pulses were made possible by the development of ultrafast lasers, mainly because of the chirped pulse amplification (CPA) technique[8] developed by Gérard Mourou and Donna Strickland[9]. This technique paved the way for particle acceleration and attosecond science[10]. The latter field was honored by the 2023 Nobel Prize awarded to Anne L'Huillier, Pierre Agostini, and Ferenc Krausz.

George Porter and Ronald G.W. Norrish developed a revolutionary technique in laser technology[11], when they used high-intensity flash tubes to initiate light-activated chemical reactions. This technique was created for aerial photography during World War II. Their results earned them the Nobel Prize in Chemistry in 1967 for exploring the dynamics of ultrafast chemical reactions. Using their stopped flow system, the study of reaction kinetics was confined to the timescales of hundreds of milliseconds. In recent years, we extended our capacity to observe complex photophysical and photochemical reactions in semiconductors and molecular systems from the microsecond to the femtosecond range, so the fastest processes within the realm of atomic chemical physics[12] can now be monitored. The technique suitable for probing physicochemical processes that occur on such a short timescale is called transient absorption spectroscopy (TAS).

Ultrafast reactions, which include some of the fastest events in chemistry, such as charge carrier generation and recombination, absorption, ionization or trapping, take place on timescales ranging from tens of femtoseconds to a few nanoseconds, as shown in Figure **1.**

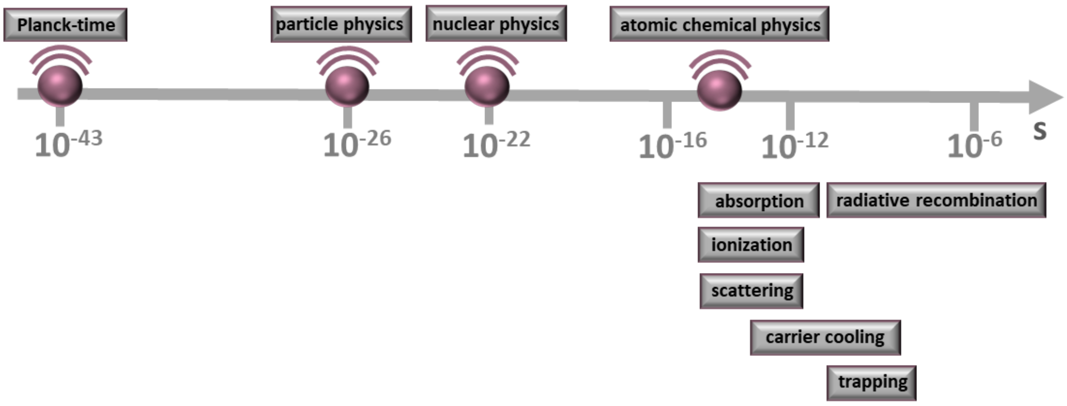

Figure 1. Timescale of ultrafast photophysical and photochemical processes varying from particle interactions to carrier dynamics, ranging from the Planck time (~10^{-43} s) to microseconds. It shows the characteristic time domains of various scientific fields, including particle, nuclear, and atomic chemical physics, as well as the typical photophysical and photochemical processes, such as absorption, ionization, scattering, carrier cooling, trapping, and radiative recombination.

1.1.2 Introduction to transient absorption spectroscopy

Most time-resolved spectroscopic methods are based on pump–probe techniques. In a pump–probe experiment, the ‘pumping’ step uses a short, intense light pulse to excite the sample, which produces various excited states at different energy levels. In the subsequent ‘probing’ step, a delayed, low-intensity, broadband light pulse measures the relaxation of these excited states. The spectrum of the probe beam can be recorded at various time delays (Δt), and contains both the fingerprints and dynamics of the species involved in the processes. The absorption of both the pump and probe beams is governed by the Beer-Lambert law:

$$I(z) = I(0)e^{-\alpha(\lambda)\, c\, z} \quad , \qquad (1)$$

where $I(0)$ is the intensity of light entering the sample, $I(z)$ is the intensity of light exiting the sample, λ is the wavelength, α is the absorption coefficient, c is the concentration, and z is the path length. The exponential term describes the spatial distribution of the electric field within a medium. In this representation, it becomes evident that the absorption coefficient changes with the wavelength of light:

$$A(\lambda) = lg\frac{I(0)}{I(z)} \quad , \qquad (2)$$

where $A(\lambda)$ is the absorbance of each probe/pump pulse.

To better visualize and understand the effect of the pump pulse, the change in absorbance (ΔA) is measured. With a mechanical chopper (operated usually at half the frequency of the pump) the pump pulse is periodically interrupted, and the probe light intensity is recorded both with (I_{on}) and without (I_{off}) the pump. The probe intensities can then be converted to absorbance values utilizing a logarithmic relation. From these, ΔA can be obtained by subtracting the sample absorbance without the pump (A_{off}) from the sample absorbance with the pump (A_{on}).

$$\Delta A(\tau,\lambda) = \; Aon\;(\tau,\lambda) - \; Aoff\;(\lambda) = lg\frac{I_0\;(\lambda)}{I_{on}\;(\tau,\lambda)} - lg\frac{I_0{}'\;(\lambda)}{I_{off}\;(\lambda)} \qquad (3)$$

Semiconductors typically feature a sharp absorption edge, as light with energy below the band gap lacks the required energy to elevate an electron from the valence band (VB) to the conduction band (CB)[13,14]. Electrons can transition between the bands in two main ways: directly and indirectly, as depicted in **Figure 2**. In the case of a direct bandgap, the top of the VB and the bottom of the CB are located at the same momentum value. In this case, both energy and momentum are conserved during an electron transition from the VB to the CB. The energy difference between the photon and the bandgap energy in this situation is given by the following equation:

$$h\nu = E_{direct\,BG} = E_{CB} - E_{VB} \quad , \qquad (4)$$

where E_{BG} is the bandgap energy, E_{CB} is the CB energy, and E_{VB} is the VB energy.

Figure 2A illustrates a semiconductor with a direct bandgap, where the maximum of the VB and the minimum of the CB are located at the same value of momentum (k). An electron can directly transition between these energy levels by absorbing a photon. Since the momentum of the photon is negligible, and the k-points of the initial and final states are the same, momentum is conserved. In the case of an indirect bandgap[15], band edges are situated at different momentum values, and during an electron transition, momentum conservation cannot be satisfied by the absorption or emission of a single photon as illustrated in **Figure 2B**. The difference between photon and the bandgap energy is not equal. A phonon (a quantized vibration of the crystal lattice that carries momentum) is involved in the momentum conservation process, and the difference between the photon and the bandgap energy equals the energy of this phonon. This makes the process a two-step and optically less efficient action.

$$E_{indirect\ BG} = E_{CB} - E_{VB} + \Delta \quad , \tag{5}$$

where Δ is the difference in quasi-momentum between the electron and the hole.

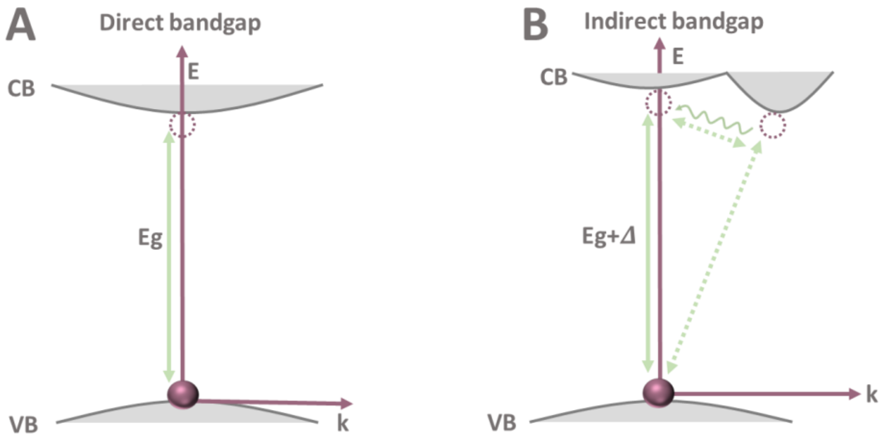

Figure 2. Schematic illustration of electronic transitions in **A:** direct and **B:** indirect bandgap semiconductors. In the direct case, the CB minimum and VB maximum occur at the same momentum (k), allowing vertical transitions via photon absorption while conserving both energy and momentum. In the indirect case, the band extrema are at different k-values, so phonon interaction is required to conserve momentum. As a result, the photon energy differs from the bandgap by the phonon energy.

1.1.3 Measuring Transition Lifetimes

For ultrafast measurements, the pump (excitation) and probe pulses (white light) must arrive at the same point and at the right moment. This spatial and temporal overlap ($\Delta t=0$) ensures that both pulses interact with the same region of the sample during the measurement. If the overlap is not precise, the recorded signal becomes weak or unreliable. Spatial overlap is achieved by aligning the beams to focus on the same spot. Temporal overlap is controlled by adjusting the delay between the two pulses. We can monitor ultrafast changes in the system with high accuracy only when both conditions are met. Figure **3A** shows the case when the time delay between the pump and probe pulses is not zero ($\Delta t \neq 0$), so there is no temporal overlap and no TAS signal is observed on the detector. In **Figure 3B**, after the adjustment of the delay stage, the two pulses arrive at the sample at the same time ($\Delta t = 0$), which is referred to as "time zero". At this point, excitation occurs, and a TAS signal becomes detectable.

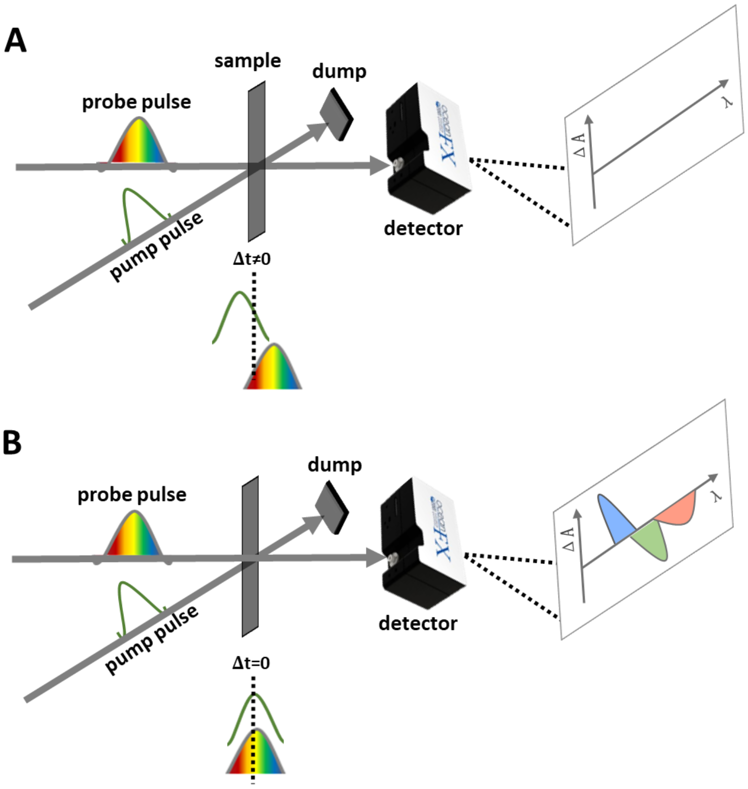

Figure 3. Schematic representation of a typical UV-Vis TAS setup, illustrating the delay of pump and probe pulses and the detection of transient signals, **A:** shows the case when the time delay between the pump and probe pulses is not zero and **B**: shows when the two pulses arrive at the sample at the same time.

Before light excitation (caused by the pump beam), the system under study (e.g., atom, molecule, semiconductor, etc.) is in its lowest energy level (ground state, E_0), depicted in **Figure 4A.** In this case, only the probe pulse is absorbed, and there is no difference between the absorption spectrum with and without the pump beam (there is no transient signal). **Figure 4B** shows that the pump and probe pulses arrive simultaneously at "time zero". The pump pulse excites electrons from E_0 to an excited state (E_1). In turn, the excited-state population gradually builds up, reaching its maximum, which will be observed by the probe pulse. **Figures 4C and 4D** show the situation after an arbitrary time following excitation. In this case, there is some time delay between the pump and the probe pulses, and depending on this delay (time resolution), the probe pulse detects the gradual deactivation of the excited state through multiple processes, as detailed in **Figure 4**.

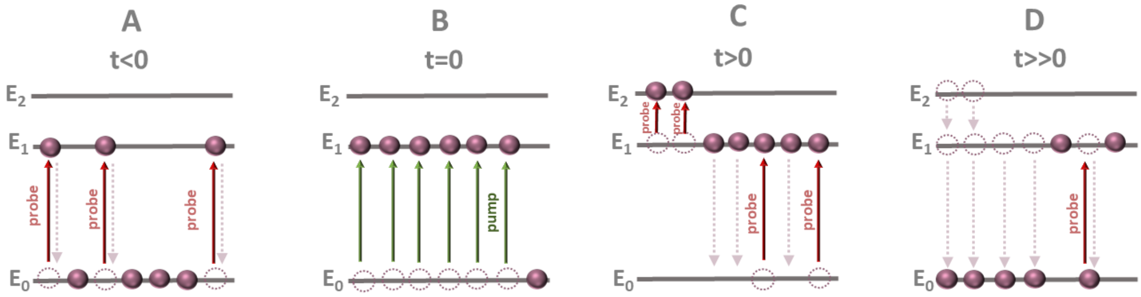

Figure 4. Schematic diagram of the energy levels **A:** before excitation **B:** at the moment of excitation and **C:** after time zero and **D:** at longer time delays.

The depletion of ground-state electrons by the pump pulse after excitation results in a decreased absorption of the probe pulse. This manifests as a large negative *ΔA* signal, termed as the ground-state bleach (GSB) signal, indicated with green in **Figure 5**. The wavelength of the GSB signal corresponds to the energy of the electronic transition (which corresponds to the bandgap energy in the case of semiconductors). Because more time elapses between excitation and probing, the magnitude of the GSB signal decreases, as the excited state gradually relaxes to the ground state. This relaxation usually follows a multi-exponential decay as multiple system-specific pathways can coexist. The newly populated excited state (A-B transition in **Figure 4C**) of the sample can absorb the probe light, resulting in an increase in absorption (positive *ΔA*). The arising spectral feature is termed as induced absorption (IA), denoted in blue in **Figure 5**. Depending on the energy difference between the A and B energy levels, the IA signal can be located either at lower or higher wavelengths with respect to the GSB signal (as positive side wings). The formed excited state can also interact with the probe beam and subsequently emit a photon while returning to the ground state. Consequently, light intensity increases in the given wavelength region, which results in a negative band on the TA spectra. This process is called stimulated emission (SE) and is shown in red in **Figure 5**. At longer time delays, relaxation processes such as internal conversion, vibrational relaxation, or recombination leads to the decay of the excited-state population. The transient signal will be weaker and eventually disappear as the system returns to equilibrium, shown in **Figure 4D**.

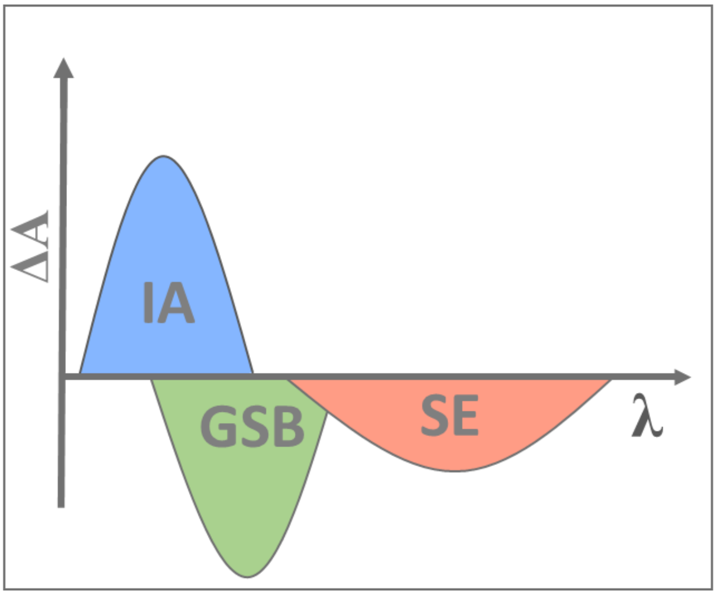

Figure 5. Schematic representation of the spectral features of the photophysical processes that are commonly observable in TAS: GSB, which arises due to the depopulation of the initial electronic state (marked with green); induced absorption (IA) corresponds to transitions from excited states to higher-lying states (marked with blue); and stimulated emission (SE) reflects the radiative decay from the excited state back to the ground state, stimulated by the probe pulse (marked with red).

1.2 Experimental considerations of transient absorption spectroscopy

Figure 6 shows the schematic layout of a TAS instrument. The fundamental beam (shown in the top right corner), typically with a wavelength ranging from 980 nm to 1080 nm. To observe a TA change, two synchronized beams will interact with the sample, so the incoming beam is split with a beamsplitter into two separate paths: the pump arm (directed to the left) and the probe arm (vertically down). Furthermore, the generation of the excited states (pump ON/OFF cycles) must be modulated with a mechanical chopper, as shown in **Figure 6**. The second harmonic from the fundamental beam can be generated with a properly selected nonlinear crystal (located in the same beam path). To preserve the short pump pulse duration, two chirp mirrors are used. The delay between the pump and probe beams is temporally controlled with a delay stage, which is the next element in the same pump arm. **Figure 6** includes a specific section that allows us to generate higher harmonics of the fundamental wavelength, which is important for selecting precise excitation wavelengths that can effectively excite specific electronic transitions in the sample. The second nonlinear crystal in the pump arm facilitates the generation of the fourth harmonic (UV), expanding the range of available excitation wavelengths. In the current configuration, a liquid cuvette sample holder is shown, used to routinely study liquid samples. After interacting with the sample, the pump beam is dumped. Downward from the beamsplitter, we reach the probe beam generation section. A lens focuses the fundamental beam on a sapphire crystal, as indicated in the schematic diagram. The sapphire crystal is a nonlinear optical element, generating a broadband continuum of light in the 400 nm to 700 nm range. This is the useful spectrum where we can monitor the TA features of the samples. The generated white light is then directed and focused on the sample and guided to the spectrometer, where the absorption changes are measured and recorded.

In the next paragraphs, I will highlight the key components of the setup that are necessary to understand how the pump and probe beams interact with the materials under study. Furthermore, details of the fundamental physical processes will be discussed for three key elements: probe beam generation (circled with white), pump beam generation (circled with green), and the role of chirp mirrors (circled with yellow).

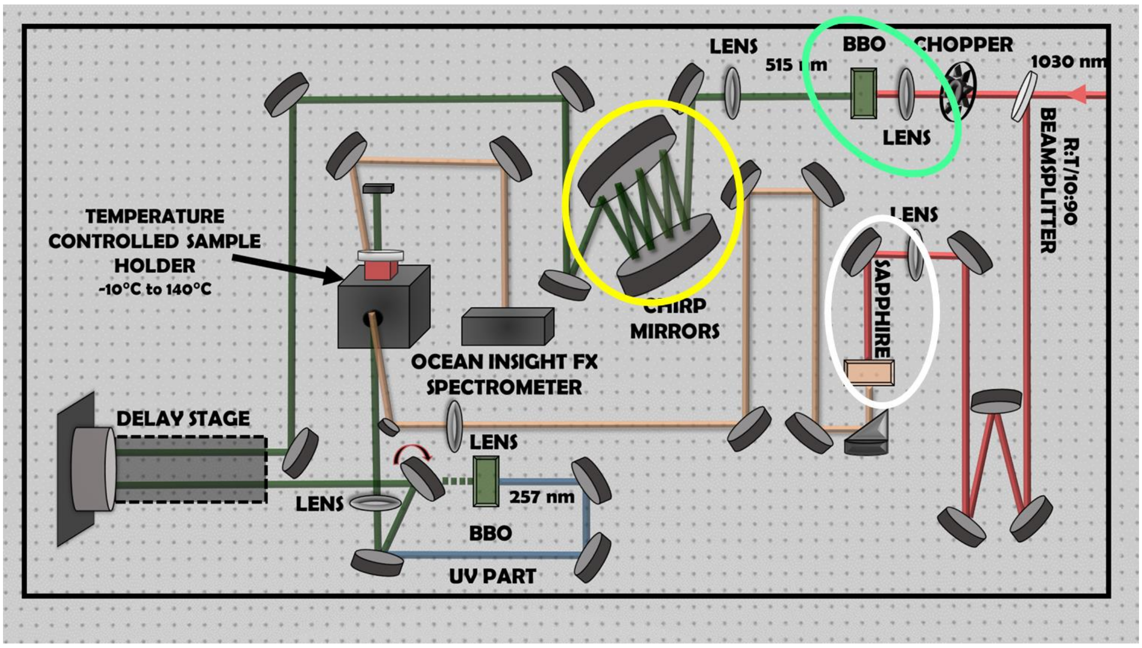

Figure 6. Schematic representation of a TAS setup. It shows the separation of the fundamental beam (red lines) into pump and probe paths with a beamsplitter; the modulation of the pump arm with a mechanical chopper to gain pump ON/OFF states; and the generation of a broadband probe continuum (white lines)

using a sapphire crystal. The setup includes BBO crystals for harmonic generation (green and blue lines), a delay stage for temporal control, and a liquid cuvette sample holder and the detector to record the signal.

1.2.1 Probe beam generation

Due to their extremely short pulse duration, ultrashort laser pulses have low energy, but their peak intensity is high compared to regular white light sources: (i) xenon lamps, which are similar to sunlight, provide a broad spectrum and high intensity, (ii) tungsten-halogen lamps, which emit strong visible and infrared light but are weaker in the UV range or (iii) LEDs but they typically have narrower spectra and lower intensity. When such laser pulses interact with specific materials, the materials' response to laser pulse excitation can be easily pushed into a nonlinear range. One of the most important nonlinear phenomena is harmonic generation, which occurs when ultrashort infrared laser pulses are focused on a birefringent β-barium borate (BBO) crystal. The laser pulse generates a Vis or UV wavelength laser pulse, which appears on the opposite side of the crystal. The second example is when an ultrashort laser pulse is focused on a quartz plate, and the focus spot on the quartz plate shines with white light. This phenomenon is called white light or supercontinuum generation. In this way, white light with (i) a wide spectrum, (ii) high intensity, and (iii) spatial coherence can be generated compared to conventional white light sources. Supercontinuum generation is necessary to study effects across a wide wavelength range. This process transforms an ultrashort laser pulse into a broadband white light source, retaining only some essential laser parameters (e.g., repetition rate), but altering most properties (e.g., pulse duration, pulse energy, wavelength range, beam size). The intensity of the laser pulse before it interacts with the nonlinear medium can be described as:

$$|E(t)^2| \propto I(t) \quad , \tag{6}$$

where $I(t)$ is the intensity, and $E(t)$ is the electric field amplitude at a given time (t). The spectral profile of the pulse $E(\omega)$, which describes the distribution of frequencies in the pulse, can be obtained through the Fourier transformation of $E(t)$.

$$E(\omega) = F\{E(t)\} \tag{7}$$

When an ultrashort laser pulse interacts with a nonlinear medium, the electric field of the pulse induces nonlinear polarization within the medium. Different higher-order terms must be used to describe the material's response to the electric field (polarization, P).

$$P(t) = \epsilon_0(\chi^{(1)}E(t) + \chi^{(2)}E^2(t) + \chi^{(3)}E^3(t)+\ldots) \quad (8)$$

Linear susceptibility ($\chi^{(1)}$) is described by linear birefringence or linear optical activity. These processes do not generate new frequencies, instead, they affect the polarization or phase of the incoming light. The second-order term[16] ($\chi^{(2)}$) becomes important in second harmonic generation (SHG), sum frequency generation (SFG), and difference frequency generation (DFG). The new photon frequency is double that of the original photons in SHG. In case of SFG, the new photon's frequency is the sum of the two original frequencies, and in DFG, the new photon's frequency is the difference between the two original frequencies. This can generate longer wavelength infrared radiation. Second-order nonlinearities are important for frequency conversion and can generate coherent light at new wavelengths. The third-order term ($\chi^{(3)}$) is predominant in white light generation. This can be important for nonlinear processes such as self-phase modulation (SPM) and third harmonic generation (THG). During SPM, the high-intensity laser pulse will propagate through the medium and change the refractive index of the material (Kerr effect). This can cause a time-dependent phase shift, which can generate new frequencies and broaden the spectrum. Four-wave mixing (FWM) is another third-order nonlinear optical process, where three input waves interact within the nonlinear medium to generate a fourth wave through the mixing of their frequencies. This can further broaden the spectrum, especially in optical fibers. The efficiency of FWM depends on phase matching, input power, and dispersion properties. Because of dispersion, the new frequencies in the light pulse travel at different speeds in the material, causing an increase in the original short pulse duration and a broadening of the spectrum. In the derivation of the nonlinear phase modulation expression, the initial pulse $E_0(t)$ is taken as the starting point. The intensity-dependent phase modulation can be expressed as:

$$\phi(t) = \gamma|E_0(t)|^2 \quad , \quad (9)$$

where γ is the nonlinear coefficient, and $|E_0(t)|^2$is the intensity of the initial pulse. After the nonlinear phase modulation, the electric field can be written as:

$$E(t) = E_0(t)e^{i\phi(t)} = E_0(t)e^{i\gamma|E_0(t)|^2} \tag{10}$$

This expression accounts for the modulation of the pulse phase due to the intensity-dependent nonlinear effect. To obtain the spectral distribution, the Fourier transform of the electric field *E(t)* is calculated as:

$$E_{WL}(\omega) = F\{E(t)e^{i\gamma|E(t)^2|}\} \tag{11}$$

This form shows that the intensity profile of the pulse induces phase modulation, which in turn results in spectral broadening. We call this white light or supercontinuum generation. Different methods that can be used to generate white light, as well as the advantages and disadvantages are summarized in **Table 1**.

Table 1. The typical methods for white light generation.

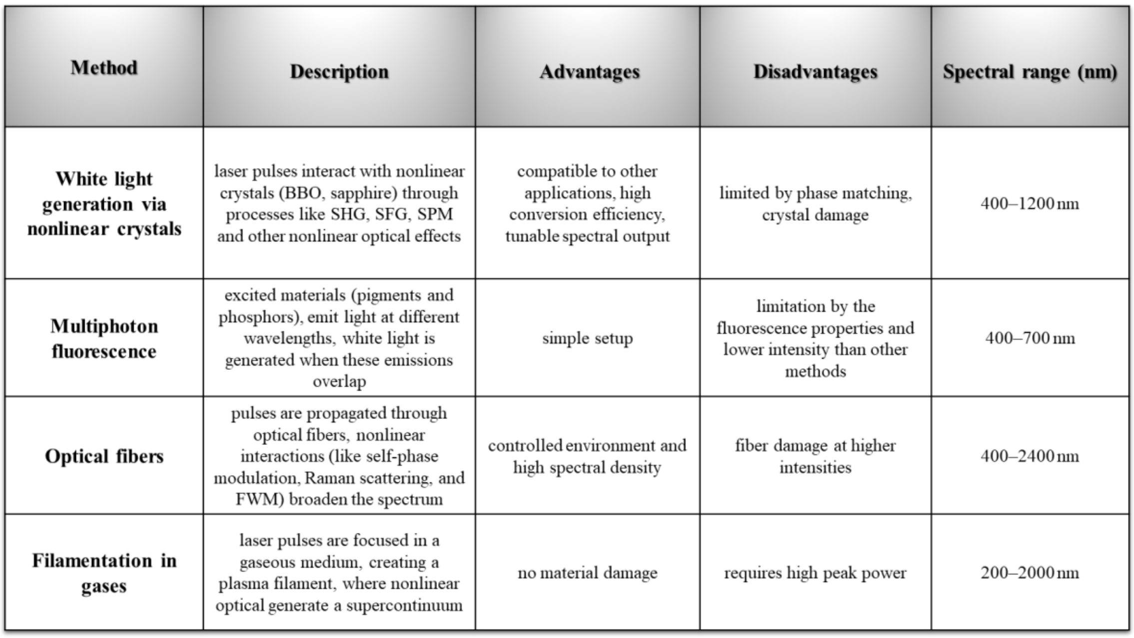

Method	Description	Advantages	Disadvantages	Spectral range (nm)
White light generation via nonlinear crystals	laser pulses interact with nonlinear crystals (BBO, sapphire) through processes like SHG, SFG, SPM and other nonlinear optical effects	compatible to other applications, high conversion efficiency, tunable spectral output	limited by phase matching, crystal damage	400–1200 nm
Multiphoton fluorescence	excited materials (pigments and phosphors), emit light at different wavelengths, white light is generated when these emissions overlap	simple setup	limitation by the fluorescence properties and lower intensity than other methods	400–700 nm
Optical fibers	pulses are propagated through optical fibers, nonlinear interactions (like self-phase modulation, Raman scattering, and FWM) broaden the spectrum	controlled environment and high spectral density	fiber damage at higher intensities	400–2400 nm
Filamentation in gases	laser pulses are focused in a gaseous medium, creating a plasma filament, where nonlinear optical generate a supercontinuum	no material damage	requires high peak power	200–2000 nm

Table 1 compares four common methods for generating white light using laser pulses: (i) nonlinear crystals, (ii) multiphoton fluorescence, (iii) optical fibers, and (iv) filamentation in gases. With frequency mixing techniques, where laser beams with different wavelengths are combined through nonlinear optical processes such as SFG or DFG, broadband white light can be generated. Frequency mixing enables precise control over the output spectrum by adjusting input wavelengths and powers. Despite its efficiency and versatility in accessing various spectral regions (from UV-MIR)[17], it requires multiple laser sources, which increases the system's complexity and cost. The

efficiency of this method also depends on the properties of the nonlinear crystals used. The phase matching ability of the crystal[18] describes the conditions where the phase velocities of the interacting waves (input lasers and generated light) are well matched, while the nonlinear coefficient of the crystal[19] measures the strength of the nonlinear interaction. The dispersion characteristics of the crystal play a role in proper phase matching[20],which determines the efficiency of the frequency mixing process and keeps the transform-limited state of the laser pulse. Crystals with high nonlinear coefficients, such as $LiNbO_3$ and BBO, are often preferred because they can generate high intensity frequency-mixed pulses. A further critical parameter is the transparency range of the crystal at the wavelengths of the incoming beam and the generated light to avoid absorption. The crystal damage threshold is also essential, as it must withstand high intensities without material damage.[21]

Multiphoton fluorescence[22] processes can also be used for white light generation; there are several materials like pigments and phosphors which are excited by laser pulses, and the overlapping emissions produce white light. This method has a simple setup but is limited by the fluorescence properties of the material and generally produces lower intensity light compared to other methods. The spectral range is 400–700 nm.

Intense laser pulses traveling through nonlinear optical fibers[23], such as photonic crystal fibers, can generate white light by broadening the spectrum through nonlinear effects like self-phase modulation and Raman scattering. However, these interactions can cause spectral fluctuations and coherence issues, especially in fibers with high nonlinear coefficients. The fiber's core size and numerical aperture are crucial, tighter focusing increases nonlinear effects but can also cause more scattering and thermal stress. Managing heat through cooling or fiber movement helps maintain spectral stability and prevent damage.

Laser pulses can be also focused in gases[24], creating a plasma filament that generates a supercontinuum. This phenomenon begins with the self-focusing process, where the intense pulse causes a nonlinear change in the refractive index, which in turn can tighten the beam. Once the intensity is high enough, ionization will occur, which will generate a plasma that counteracts self-focusing and stabilizes the filament. Inside the filament, several nonlinear effects can broaden the spectrum. SPM will change the phase of the pulse, generating new frequencies. This method prevents material damage but requires very high peak power. The achievable spectral range is 200–2000 nm.

To sum up, intense laser pulses interacting with a nonlinear medium, such as photonic crystal fiber or bulk materials (e.g., YAG, sapphire)[25], are the most widely used methods to produce white light. **Figure 7** shows the spectral output in sapphire and YAG crystals under high-intensity laser excitation. Sapphire is an effective material for supercontinuum generation due to its broad transparency range and wider spectral output compared to YAG. It also has a higher damage threshold, which makes it more flexible under intense laser pulses and reduces the risk of material damage. Additionally, sapphire provides more stable and intense white light output across a broad wavelength range. Its high nonlinear coefficient and thermal handling capabilities further increase its use in ultrafast laser systems.

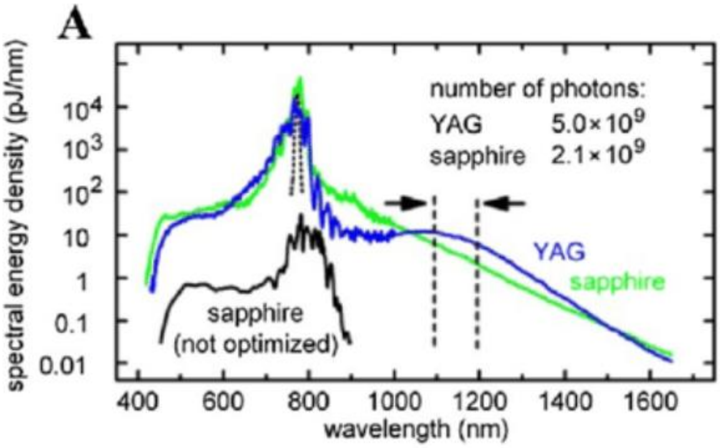

Figure 7. Comparison of supercontinuum spectral output in sapphire and YAG crystals under high-intensity laser excitation, demonstrating sapphire's broader spectral range and higher damage threshold.[25]

Nonlinear interactions broaden the spectrum, but they can be challenging to keep under control[26] because of spectral fluctuations and coherence issues. These problems often arise from the complex nonlinear effects, which can reduce efficiency and distort the output spectrum. Precise positioning (rotation), proper crystal selection, and crystal dimensions (e.g., thickness) can be essential to keep the transform-limited nature of the pulse, while simultaneously achieving optimal white light generation efficiency.

Focusing is critical in white light generation. It depends on beam diameter, lens properties, and the numerical aperture (NA). The spot size ω_0 is calculated as:

$$\omega_0 = \frac{\lambda}{\pi\, NA} = \frac{\lambda}{\pi\, n\, sin\theta} \quad , \qquad (12)$$

where λ is the wavelength, n is the refractive index and θ is the half-angle of the focused cone. A smaller focal spot size increases intensity at the focus, enhancing nonlinear effects. However, tight focusing can cause excessive intensity, leading to spectral distortions or material damage, so balancing spot size[27] and intensity is key.

The defects in nonlinear crystals – crystal or material damage related, such as impurities or burn spots – can further decrease the stability through the uncontrolled variation of the thermal properties (e.g., thermal conductivity, thermal expansion, and thermo-optic coefficient) of optical elements. To avoid thermal issues, a cooling system can be implemented, or the crystal can be continuously moved, which helps distribute the heat over a larger area and prevent localized overheating. The characteristics of the actual output spectrum depend strongly on the specific experiment, and the properties of the optical material (as shown in **Figure 8**). However, the parameters of the fundamental laser are the most crucial ones.

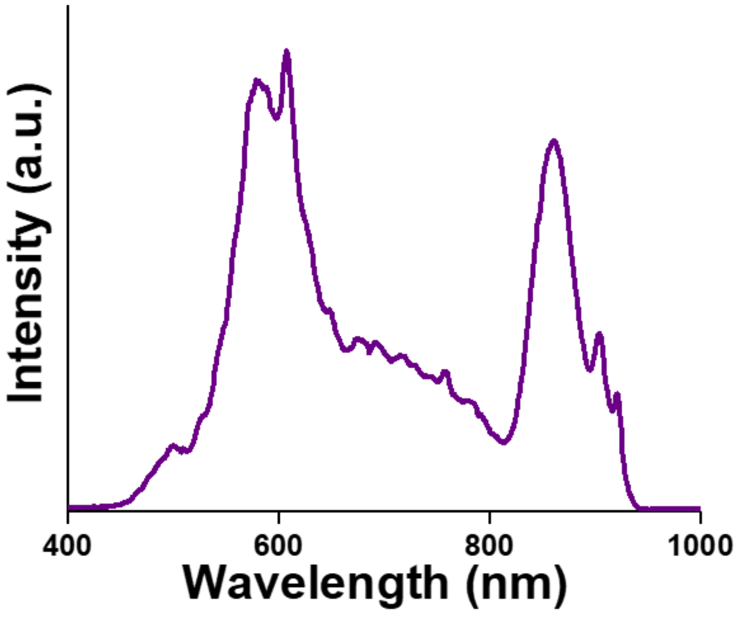

Figure 8. The typical white light spectrum generated with a 2 mm thick, 2.54 mm diameter sapphire crystal via laser pulses with 30 fs duration, 100 µJ energy, 100 kHz repetition rate, and a spectral range of 980–1080 nm.

1.2.2 Pump beam generation

SHG is used across various fields, such as holography, biomedical imaging, and ultrafast spectroscopy[28,29]. It is used to generate new wavelengths of light that are doubled in frequency compared to the fundamental light and not accessible with standard laser sources. During SHG, the laser beam propagates through a nonlinear crystal, for example BBO. This can produce high-intensity, ultrashort pulses that are suitable in TAS experiments for sample excitation, as illustrated by **Figure 9**. The efficient generation of pump pulses is crucial for performing TAS experiments, requiring careful consideration of several parameters that will be discussed in the following section. In parallel, we must achieve a short time duration (high resolution), exceptional pulse stability (repeatability), and find an ideal wavelength for sample excitation. This wavelength must always align with the absorption bands of the light-active material under study, which puts a strain on the experimental design of the setup.

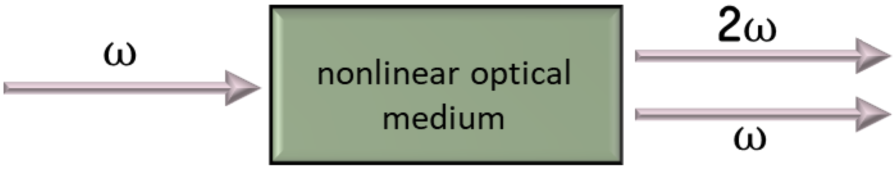

Figure 9. The schematic diagram of second harmonic generation shows how a laser beam interacts with a nonlinear crystal and generates a frequency double the original one.

As discussed in the previous section dedicated to white light generation, second-order nonlinear susceptibilit $\chi^{(2)}$ is important for SHG. This process is important for frequency conversion and leads to the generation of coherent light at new wavelengths. The electric field of the light $E(\omega,z)$ with the fundamental frequency (ω) as a function of the propagation distance (z) in the nonlinear crystal can be described as:

$$E(\omega, z) = E_0(\omega) \cdot e^{(-i \cdot k(\omega) \cdot z)} \tag{13}$$

Here, $E_0(\omega)$ is the amplitude of the electric field at the fundamental frequency, $k(\omega)$ is the wavevector of light in the medium, and z is the propagation distance in the nonlinear crystal. We can generate the second harmonic light pulse with a frequency of

2ω after the fundamental pulse interacts with the nonlinear crystal. In this case, the electric field $E_{2\omega}(2\omega, z)$ can be described as:

$$E_{2\omega}(2\omega, z) = \chi^{(2)} \cdot E_0^2(\omega) \cdot e^{(-2i \cdot k(\omega) \cdot z)} \tag{14}$$

Second-order nonlinearity changes the frequency of the light pulse while keeping the phase consistent during propagation through the crystal. The intensity of the second harmonic light depends on the fourth power of the original light's electric field:

$$I_{2\omega} \propto \left|\chi^{(2)} \cdot E_0^2(\omega)\right|^2 = \left|\chi^{(2)}\right|^2 \cdot E_0^4(\omega) \tag{15}$$

This shows that the SHG strongly depends on the input light properties and the intensity of the generated SHG light is proportional to the square of the original light's intensity. Even small changes in the parameters of the input light can cause major changes in the SHG intensity.

From the aspect of the nonlinear crystal, under optimal phase matching conditions (highest conversion efficiency), the SHG power increases with the square of the crystal length:

$$P_{2\omega} \propto (\chi^{(2)} \cdot I_\omega \cdot l)^2 \quad , \tag{16}$$

where $P_{2\omega}$ is the generated SHG power, I_ω is the intensity of the pump, $\chi^{(2)}$ is the second-order nonlinear polarization susceptibility and l is the crystal length. At higher intensities, the SHG efficiency does not increase linearly; there is a saturation point due to energy depletion. This saturation behavior can be expressed as:

$$P_{SHG} = \frac{\gamma I^2 l}{1+(\frac{I}{I_{trs}})^2} \quad , \tag{17}$$

where γ is the nonlinear gain coefficient (and depends on the second-order nonlinear susceptibility $\chi^{(2)}$), I is the intensity, l is the crystal length, and I_{trs} is the saturation threshold.

When phase matching is not optimal, the SHG power becomes sensitive to the angle between the incoming light and the crystal orientation, as well as the polarization of the incoming light:

$$P_{SHG} \propto {I_{pump}}^2 \cdot sin^2(\theta) \cdot \left|\chi^{(2)}\right|^2 \quad , \tag{18}$$

where θ is the angle between the incoming light and the crystal orientation. This angular dependence arises due to phase mismatch, resulting in reduced SHG efficiency as the generated second harmonic waves start to dephase relative to the fundamental waves. By optimizing the phase matching angle, it is possible to maximize the SHG. When phase matching is not optimal, the SHG power becomes sensitive to the angle between the incoming light and the crystal orientation, as well as the polarization of the incoming light. Phase matching is crucial not only for maximizing SHG efficiency but also for effectively controlling dispersion, which plays a crucial role in keeping the transform-limited state of the laser pulse.

1.2.3 Chirp mirrors and light dispersion

Different wavelengths propagate with different speeds in matter, due to which the light pulse spreads out in time and space.[30] This causes the refractive index of a material to change with the wavelength of light. This phenomenon is called dispersion. We can describe the dispersion of light in a medium with the relationship between the wavevector (k) and the refractive index ($n(\omega)$):

$$k(\omega) = \frac{n(\omega)\omega}{c} \ , \tag{19}$$

where c is the speed of light in vacuum.

The wave vector $k(\omega)$ can be expanded around the central frequency (ω_0) using a Taylor series expansion:

$$k(\omega) = \sum_{n=0}^{\infty} \frac{1}{n!} \left.\frac{d^n k}{d\omega^n}\right|_{\omega_0} (\omega - \omega_0)^n \ , \tag{20}$$

where $k(\omega_0)$ is the wave vector at the central frequency and describes the fundamental propagation behavior of the pulse. To highlight how each derivative influences the pulse distortion, the previous expression can be expanded, where the higher-order terms significantly impact the dispersion analysis.

$$k(\omega) \approx \ k(\omega_0) + \left.\frac{dk}{d\omega}\right|_{\omega_0} (\omega - \omega_0) + \frac{1}{2} \left.\frac{d^2 k}{d^2\omega}\right|_{\omega_0} (\omega - \omega_0)^2 + \tag{21}$$

$$\frac{1}{6}\frac{d^3k}{d^3\omega}\bigg|_{\omega_0}(\omega-\omega_0)^3+\frac{1}{24}\frac{d^4k}{d^4\omega}\bigg|_{\omega_0}(\omega-\omega_0)^4+\dots\quad ,$$

where $\frac{dk}{d\omega}\big|_{\omega_0}$ is the first-order dispersion. It represents how the pulse travels through the medium, and is called group velocity dispersion (GD). Group-delay dispersion (GDD) $\frac{d^2k}{d^2\omega}\big|_{\omega_0}$ is the second-order dispersion, which is responsible for spreading the pulse in time due to the different velocities of the frequency components and can introduce chirp. Third-order dispersion $\frac{d^3k}{d^3\omega}\big|_{\omega_0}$ (TOD) causes asymmetry in the pulse shape as well as spectral distortions. Fourth-order dispersion (FOD) $\frac{d^4k}{d^4\omega}\big|_{\omega_0}$ creates shoulders in the pulse spectrum by introducing subtle phase shifts at the spectral edges.

The n-th order derivatives $\frac{d^nk}{d^n\omega}\big|_{\omega_0}$, commonly mentioned as β_n, express the spectral phase $\varphi(\omega)$ of a pulse after propagation through a dispersive medium of length L. These β_n parameters describe the phase evolution of the pulse:

$$\phi(\omega)=k(\omega)\,L=\sum_{n=0}^{\infty}\beta_n\,(\omega-\omega_0)^n\ , \tag{22}$$

where β is the temporal chirp parameter, which describes the time-dependent frequency fluctuation of the pulse. The time-dependent frequency of a chirped pulse can often be described by a quadratic phase:

$$\phi(t)=\phi(0)+\beta^2\ , \tag{23}$$

where $\phi(t)$ represents the time-dependent phase of the pulse, and $\phi(0)$ is the initial phase.

If $\beta > 0$, the pulse is positively chirped: the lower frequency components arrive first, followed by the higher frequencies. This causes a temporally stretched pulse. If $\beta < 0$, the pulse is negatively chirped, i.e. the higher frequency components arrive earlier, causing the pulse to compress over time.

Figure 10 shows the influence of the different β_n terms on the spectral phase of an ultrashort high intensity coherent beam.[31] **Figure 10a** shows the undistorted reference pulse, with no dispersion effects applied to β_0. **Figure 10b** shows the effect of β_1, which introduces a time delay in spectral components, shifting the entire pulse in time without changing its shape or introducing chirp. In **Figure 10c**, the β_2 parameter introduces GDD, causing different spectral components of the pulse to propagate at different group velocities in the medium. This leads to pulse broadening. If $\beta_2>0$, normal dispersion occurs, where lower frequencies travel slower compared to higher frequencies, resulting in a positively chirped pulse. **Figure 10d** demonstrates the effect of β_3, which causes TOD. This makes the pulse asymmetric, producing shoulders and oscillations due to the cubic dependence of the phase on frequency. Further distortion is shown in **Figure 10e**, where the β_4 term causes FOD, adding even more complexity to the pulse shape, including multiple peaks and temporal oscillations.

In laser-based experiments, pulse dispersion must be controlled and compensated. This can be achieved using chirped mirrors.[8] These multilayer mirrors consist of alternating high- and low-refractive-index layers precisely engineered to reflect different wavelengths at varying depths and mitigate the effect of optical dispersions.

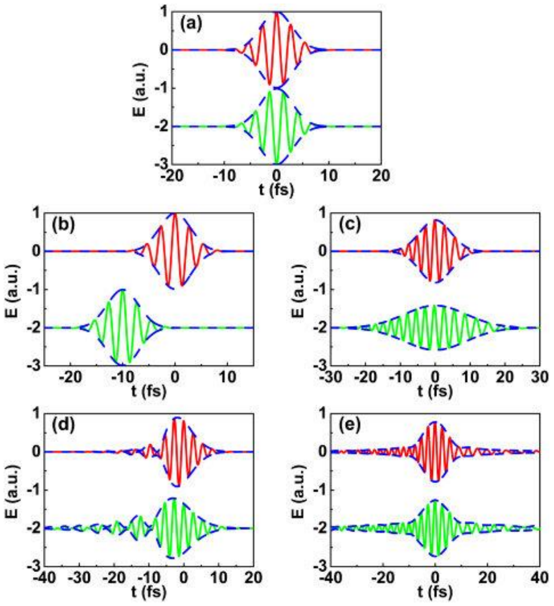

Figure 10. The temporal effects of the spectral phase derivatives in a schematic manner. **A:** shows the reference pulse without any dispersion. **B:** shows the first-order spectral phase derivative (GD), which introduces a linear time shift without altering the pulse shape. **C:** shows the effect of the second-order spectral phase derivative GDD, which causes pulse broadening and chirp. **D:** shows the third-order spectral phase derivative TOD, which creates asymmetry and leads to the formation of shoulders or oscillations in the pulse, and **E:** demonstrates the effect of the fourth-order spectral phase derivative (FOD), causing further distortion, multiple peaks, and a more complex temporal structure.[31]

1.2.4 State of the art in TAS

TAS can be extended to study complex biological systems (light-harvesting complexes in photosynthetic organisms, protein folding dynamics, or photoactivated ion channels), where ultrafast processes are crucial, e.g. during energy transfer between chromophores, rapid conformational changes in proteins, or the isomerization of photoactive molecules. Capturing these events is essential for understanding how biological functions arise from molecular motion, how proteins respond to light stimuli, or how organisms efficiently convert light into chemical energy. From the spatial dimension point of view, TAS typically follows kinetics at a particular point of the sample. An exciting direction of TAS is the extension of this method to obtain temporal and spatial information simultaneously when combined with time-resolved imaging techniques.[32] TAS for in situ and operando investigations can gain real-time insights into dynamic processes in various applications (e.g., catalysis, materials science, and energy storage). Further development [33–35] of TAS for studying biological systems can contribute to our understanding of photobiological processes, which have relevance in areas like photosynthesis and disease mechanisms. In general, TAS is typically used to investigate an ensemble of molecules and particles. The advancements in TAS as a single-molecule technique can provide detailed insights into individual molecules' behavior (absorption and relaxation after photoexcitation, differences in conformational states, local environments, or reaction pathways), offering a deeper understanding of heterogeneity within a sample.[36]

Different measurement techniques are available for ultrafast timescale studies. These techniques can be classified according to the types of light–matter interactions (e.g., emission and absorption techniques) or by the type of interactions between the light pulses (e.g., coherent and incoherent techniques). For instance, two-dimensional electronic spectroscopy (2DES), which is a coherent spectroscopic technique, uses multiple laser pulses to construct a two-dimensional map of molecular electronic transitions and the coherent interactions between various vibrational modes. This approach facilitates the examination of ultrafast energy transfer processes. Ultrafast techniques can also be classified according to the frequency of light used.

Despite its straightforward concept, TAS is a versatile technique and can be operated in a broad range of excitation and probing frequencies, extending from X-rays to terahertz (THz) pulses. These broad frequency ranges allow for tracking various physical processes in materials, as summarized in **Table 2.** With X-ray Free-Electron Lasers (XFELs), which produce intense and rapid X-ray pulses, we can track the ionization state of matter. XFELs are instrumental in enabling scientists to explore atomic and molecular processes (e.g., capturing images of ultrafast phenomena in structural biology and chemistry) on femtosecond timescales.

Table 2. The typical physical processes by different pump–probe: UV, Vis, IR, THz, and XUV/X-ray pulses can serve as pump or probe to study phenomena ranging from electronic excitations and vibrational dynamics to ultrafast electron motion. The choice of wavelengths defines the accessible timescale (fs–as) and the type of dynamics observed.

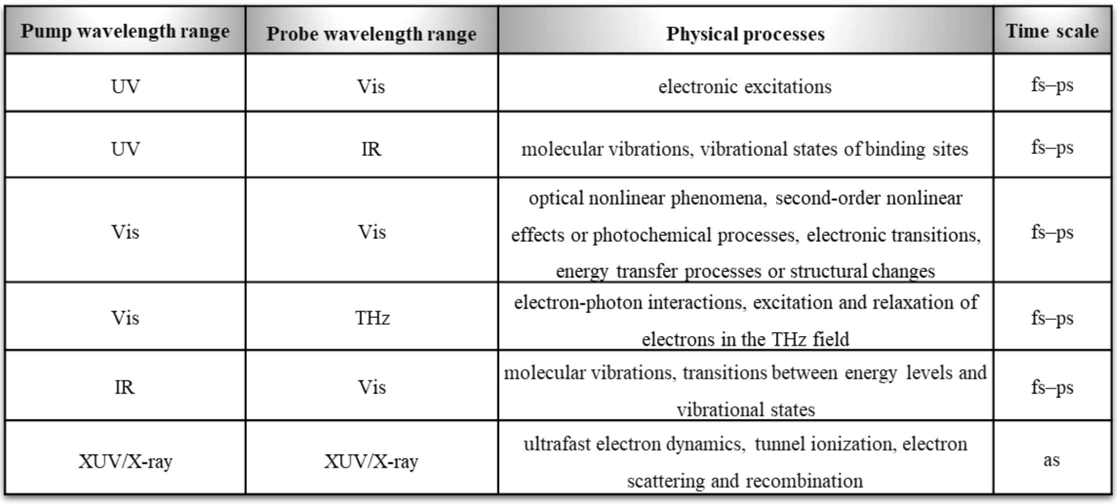

Pump wavelength range	Probe wavelength range	Physical processes	Time scale
UV	Vis	electronic excitations	fs–ps
UV	IR	molecular vibrations, vibrational states of binding sites	fs–ps
Vis	Vis	optical nonlinear phenomena, second-order nonlinear effects or photochemical processes, electronic transitions, energy transfer processes or structural changes	fs–ps
Vis	THz	electron-photon interactions, excitation and relaxation of electrons in the THz field	fs–ps
IR	Vis	molecular vibrations, transitions between energy levels and vibrational states	fs–ps
XUV/X-ray	XUV/X-ray	ultrafast electron dynamics, tunnel ionization, electron scattering and recombination	as

With the UV pump–probe combination we can observe electronic excitations to understand the electronic properties of materials with strong absorption in the UV region, such as nucleic acids, aromatic amino acids, and conjugated organic molecules. The high photon energy of UV light enables the excitation of electrons from deep VB states to the CB in semiconductors. Time-resolved UV TAS is suitable for monitoring the internal conversion processes in pyrene, revealing sub-100 fs dynamics.[37]

UV pump and IR probe combination can aid in studying molecular vibrations, providing valuable insights into the structure and dynamic properties of molecules. IR pump pulses selectively excite specific vibrational modes, and thus allow for monitoring the intramolecular energy transfer and relaxation processes. Using optically heterodyne-detected UV-IR transient gratings, detection sensitivity can be enhanced and detailed information on molecular dynamics can be obtained.[38]

Visible light pump–probe spectroscopy has several advantages over UV and IR techniques, because it allows for tuning the photon energy across a broad spectral range and for investigating both resonant and nonresonant excitations, including hot carrier dynamics. This flexibility also helps minimize sample degradation, especially in organic and biological samples, because visible light is less energetic than UV radiation. Furthermore, visible detectors, such as charge-coupled devices (CCDs) and silicon photodiodes, are sensitive and more readily available in this wavelength region. Visible pump–visible probe spectroscopy effectively demonstrates how free carrier absorption, state filling, and lattice heating impact reflectivity in semiconductors such as Si, Ge, and GaAs.[39]

The combination of visible light pump and THz probe allows for the study of electron–phonon interactions. It can control electronic excitation by the detection of carrier dynamics and conductivity changes and provide selective sensitivity to free carriers over excitons. Unlike UV or visible probes, the THz probe directly captures low-energy excitations and offers a noninvasive view of carrier mobility and lattice responses. The THz probe enables direct observation of the relaxation dynamics of the photoexcited carriers, specifically the transition between insulating and conducting phases on ultrafast timescales. It provides direct information about conductivity changes induced by visible pump excitation.[40]

The vibrational-pump and visible-probe (VPVP) combination uses an IR pump to selectively excite specific vibrational modes in a material and a visible light probe to monitor the resulting changes in electronic or optical properties, e.g. vibrational-electronic coupling. It is also possible to measure thermal conductivity in metal-halide perovskites by inducing vibrational excitations and probing their impact on visible light transmission.[41]

Another example is the use of High Harmonic Generation (HHG) as a probe to broaden the scope of TAS into the XUV region.[42] Directing intense femtosecond laser pulses into a gas target can create individual attosecond pulses within the XUV range[43]. The temporal confinement and broad spectral bandwidth of attosecond pulses enable the exploration of ultrafast electron dynamics in atoms and molecules, such as ionization, charge migration, and electron correlation effects.

Currently, the highest time resolution TAS measurements can achieve is in the range of a few tens of attoseconds[44–48]. In Attosecond Transient Absorption Spectroscopy (ATAS) experiments, ultrashort laser pulses within the attosecond regime are utilized to induce photoexcitation or ionization processes in the sample under study. Subsequently, a synchronized probe pulse, typically in the XUV or soft X-ray region, is employed to probe the electronic and structural response of the sample with femtosecond or subfemtosecond time resolution. Through the analysis of the changes in the probe pulse induced by the sample interaction, ATAS provides insight into fundamental processes such as electron relaxation, charge transfer, and energy transfer at the atomic and molecular level.

2DES[49] is a technique used to track ultrafast coherent and incoherent processes in real time.[50] By precisely tuning the interactions between light and matter concerning time, phase, and amplitude between the three pulses (excitation pulse, probe pulse, local oscillator pulse) 2DES allows for the observation of the nonlinear signal's temporal changes in relation to two frequencies, and provides spectral information on both the excitation and detection pulses. In comparison to conventional one-dimensional spectroscopy, 2DES can depict electronic and vibrational transitions in two dimensions, enabling detailed analysis of the complex internal dynamics of molecules or materials. Furthermore, it offers more precise insights into vibrational and electronic movements, interactions, couplings, and relaxation processes. [42]

With these techniques, we can thoroughly investigate the dynamic behavior of these complex systems, shedding light on their previously unexplored aspects and potentially unlocking their full potential for a wide range of applications.

1.2.5 Temperature-dependent TAS

Temperature can influence the optical and electronic properties of materials, and is hence a major factor in materials science, semiconductor physics, and photovoltaics.[51–53] Temperature-dependent studies on metal-halide perovskite thin films show significant changes in charge carrier mobility and recombination dynamics, which provides information on phase transitions and alterations in trap state distributions.[54] Temperature has a direct or indirect impact on the charge carrier dynamics of materials on a wide timescale (fs to ms). We can observe the direct effect on the determined charge carrier distributions between different energy levels (e.g., trap states, impurity states etc.), kinetic parameters (e.g., excited-state lifetimes), and activation energies of different photophysical processes. A study on $FAPbI_3$ perovskite thin films shows that temperature can significantly modify excited-state lifetimes and activation energies.[55] The indirect effect is related to the impact of temperature on material properties or coupled reactions. Variations in temperature may induce phase transitions in materials, or alter the solvation dynamics of a molecular complex. Theoretical simulations suggest that ultrafast TAS spectra are highly sensitive to temperature variations, affecting both charge carrier cooling dynamics and recombination processes.[56]

Generally, temperature-dependent TAS studies focus on the low-temperature regime. [57–59] These measurements offer several advantages, such as slowing down (or even freezing) the vibrations of molecules and solids. From the perspective of TAS, this will slow down the relaxation of the excited state as direct recombination pathways become more favored in these cases. Furthermore, low temperatures enhance experiment stability, reproducibility, and decrease environmental noise, allowing for more precise measurements.[13–15] Temperature-dependent TAS measurements were performed for CdS and cadmium selenide (CdSe) nanorods between 160 to 294 K, to elucidate the exact mechanism of charge carrier dynamics. These measurements reveal weak electronic coupling between neighboring trap states and suggest that surface-localized trapped holes couple strongly to phonons, leading to slow charge carrier diffusion. At near room temperatures, trap-to-trap hole hopping behaves classically, while phonon-assisted tunneling becomes observable at low temperatures. Furthermore, the role of thermally activated pathways in the recombination mechanism can also be studied. [59]

High-temperature TAS can provide insights into the behavior of materials at extreme conditions, offering critical information for materials science and engineering that are used or processed at elevated temperatures. However, the field of high-temperature TAS has not received as much attention as other areas of spectroscopy. There are some challenges associated with performing high-temperature, in situ TAS measurements. They require specialized equipment (temperature-controlled sample holders with stirring), and the thermal stability of the material and the solvent in the case of dispersions (boiling point) must be considered. It has been found that at higher temperatures, certain crystal defects can transform into electron traps, reducing optical gain and increasing the lasing threshold. This phenomenon is particularly relevant for continuous-wave lasing, where temperature changes can significantly impact performance.

At high temperatures, electron trapping occurs very fast in colloidal CdSe/CdS QDs.[60] This process starts within about 350 femtoseconds after excitation. At 413.15 K, the GSB amplitude decreases by up to 50%, showing a rapid loss in excited carriers. At elevated temperatures, vibrations force defect states to shift and overlap with the CB. These shifting defect states capture electrons efficiently. As a result, this trapping limits the number of carriers available for optical gain and weakens the performance of QD lasers during continuous operation. **Figure 11A** shows that the temperature-dependent linear absorption spectra decrease by 30% in case of biaxially strained colloidal QDs, and

Figure 11B shows that the same decrease is about 50% in case of hydrostatically strained QDs.

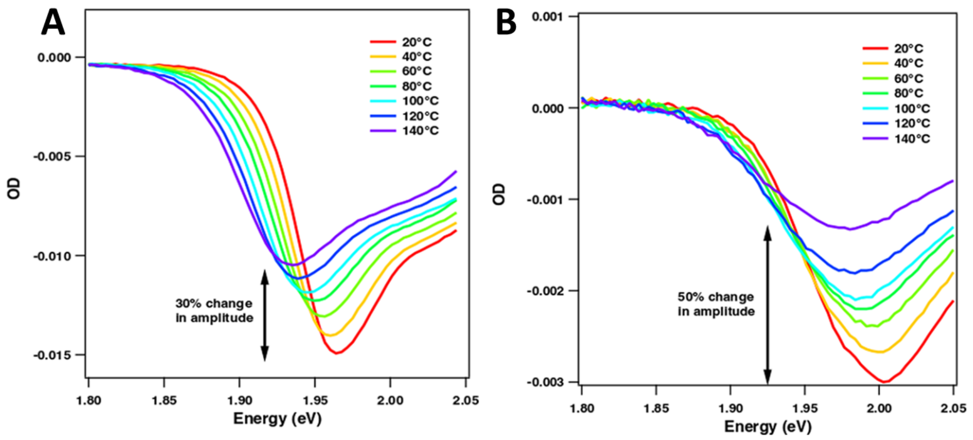

Figure 11. A: The temperature-dependent linear absorption spectra of biaxially strained colloidal QDs between 20 and 140 °C centered around 630 nm wavelength.[60] **B:** Ultrafast TA spectra following a 25 ps delay for hydrostatically strained QDs.

At temperatures up to around 500 K, electrons stay excited for several nanoseconds.[61] TA measurements clearly show this long-lived signal. At the same time, PL fades much faster, especially above 400 K. This means that holes disappear quickly before they can recombine with electrons. Heat activates hole traps that capture holes on subnanosecond timescales. As a result, light emission drops significantly, even though electrons are still present. Nanoplatelets with thicker CdS shells, such as the 6/4/6 monolayer sandwich structures, show more stable behavior and slower changes in signal. These thicker shells help block trapping and protect the excited carriers at high temperatures.

1.3 Low-dimensional materials systems

1.3.1 Introduction to CdSe quantum dots

QDs are semiconductor nanocrystals with sizes ranging from individual molecules to bulk substances. QDs are small (< 10 nm) semiconductor nanocrystals, with altered light-absorbing and emitting properties compared to larger nanocrystals and bulk materials. When the size of these nanocrystals is reduced to dimensions smaller than the bulk exciton Bohr radius, a phenomenon called quantum confinement occurs.[2,62] This confinement affects the motion of both electrons and holes in all three dimensions, resulting in an increase in the effective bandgap of the material as the crystallite size decreases, as shown in **Figure 12**. Therefore, the optical properties – including light absorption and emission – of QDs exhibit a blueshift to higher energies with decreasing size. Smaller QDs emit light with higher energy (shorter wavelengths), typically in the blue or UV range. Conversely, larger QDs emit light with lower energy (longer wavelengths), typically in the red or near-infrared (NIR) range. By controlling the size of QDs during synthesis, the optical properties can be precisely controlled. The corresponding photoluminescence (PL) spectra of the colloidal CdSe quantum dots are shown in **Figure 12**, where the color variation reflects the size-dependent emission shift. Different complex materials can be prepared as QDs, such as CdSe indium arsenide (InAs), and recently metal-halide perovskites ($CsPbBr_3$). Despite their small size, structural studies indicate that these nanocrystals maintain the crystal structure and lattice parameters of their bulk counterparts.[63] The special properties of QD systems make them useful in nanoelectronics (display technologies), medical imaging applications, solar cells, and quantum computing. Colloidal QDs are intriguing substances for creating laser diodes that can be processed in solutions.[64] These diodes offer the advantages of customizable emission wavelengths through size control, low thresholds for optical gain, and seamless integration with photonic and electronic systems. Utilizing these colloidal QDs, Amplified Spontaneous Emission diodes display robust and broad optical gain and emit strong, edge-based light with an instantaneous power output of up to 170 µW.

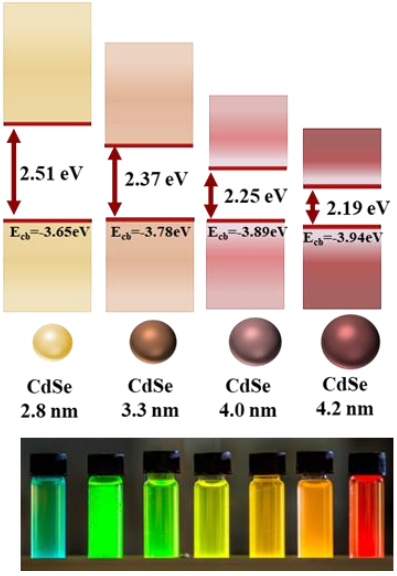

Figure 12. The bandgap energies and corresponding PL of colloidal CdSe QDs as a function of size and composition. The top panel illustrates the bandgap energy (E_{cb}) of CdSe QDs with varying diameters,

demonstrating a shift in energy levels as the particle size decreases. The bottom panel shows vials of CdSe QDs emitting in distinct colors[65] under UV illumination, corresponding to the different sizes and bandgap energies.[66]

The backbone of QD research is CdSe, which is a well-investigated material system both in terms of its synthesis and optical properties. CdSe QDs possess rich excited-state dynamics, with exotic quasi-particles (e.g., dark, bright excitons, trions), where several intertwined processes can occur.[67–71] This is partially caused by the electronic structure of CdSe, where both the CB and VB are formed from the Cd 5s and Se 4p orbitals.[72] After excitation, the holes have both spin and angular momentum; these properties are also transferred to the forming quasi-particles, thus optically allowed and forbidden transitions coexist.[68] The complexity deepens in QDs, where their significant surface-to-volume ratio encourages surface trapping. This process is size-dependent and occurs faster in smaller QDs because of the larger charge carrier overlap with the surface.[73] After excitation, the intraband relaxation of holes is coupled to the thermalization of electrons, where the initial hole relaxation occurs in the range of 500 fs – 2 ps, depending on QD size, but independent of surface properties. Typically, hole trapping occurs in the first few ps after excitation, and electron trapping in 20–50 ps in CdSe nanocrystals.

1.3.2 Doping/alloying quantum dots

Incorporating various elements into the QD lattice, through doping or alloying, alters their physicochemical attributes (e.g., size, energy levels, and surface termination of QDs, conductivity, Fermi energy, etc.), which affects the observed properties of the excited state.[74–77] Alloying in semiconductor preparation is the process when two or more constituent elements of the material (e.g., Cd in CdSe or Zn in ZnSe) are mixed in comparable quantities to create a new material with gradient (or combined) properties (e.g., Cd_xZn_ySe). In contrast, doping is the process where only small amounts of impurity elements are incorporated in the semiconductor to change its electronic properties (~ppb quantities). Many studies confuse the terms doping and alloying, but they are different processes. **Figure 13** shows the schematic diagram of the n-type and p-type doping/alloying process. In the case of n-type doping/alloying, an additional energy level is introduced, shifting the Fermi level closer to the CB. In p-type doping/alloying, this shift occurs in the opposite direction, the Fermi level will be closer to the VB and will introduce an extra energy level close to the VB. With this modification, it is possible to fine-tune their optoelectronic properties — including light emission and absorption characteristics, emission wavelength, energy levels, and conductivity.[78–82] Doping or alloying not only improves the conductivity of QDs (which is important for electronics and solar cells) but also makes them more durable, which can help them resist environmental stress and perform better in various applications.[83]

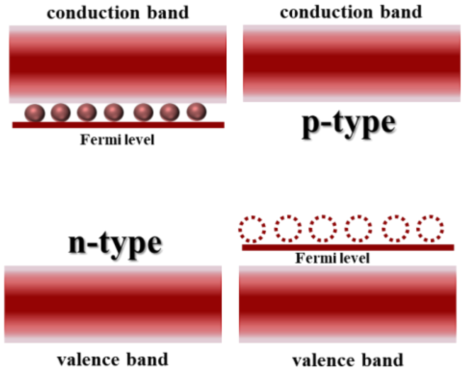

Figure 13. Schematic illustration of n-type and p-type doping/alloying in semiconductor QDs. In the n-type process, dopant atoms introduce electronic states near the CB, shifting the Fermi level upward. In the p-type process, acceptor states form near the VB, lowering the Fermi level. These adjustments enable control over charge carrier dynamics and optical properties, relevant for applications in light harvesting and optoelectronics.

1.3.3 Core-shell quantum dots

Core-shell QDs are prepared by depositing a layer of a larger bandgap semiconductor material on the surface of QDs. This passivates the surface defects that form during synthesis and act as recombination pathways, ultimately enhancing the PL efficiency by mitigating surface-related nonradiative recombination pathways.[84] Generally, core-shell heterostructures can be classified based on the relative position of the energy bands of the constituent semiconductor materials, and type-I, type-II and quasi-type-II arrangements can be realized, as shown in **Figure 14**.

In type-I band alignment, the shell surrounds the core with a larger bandgap, so it can trap both electrons and holes inside the core. The two carriers stay close together and can recombine easily, which produces strong light emission (useful in LEDs). In the type-II band, the electron and the hole end up in different regions. One in the core, the other in the shell. This separation slows down their recombination and prolongs the exciton lifetime. Such structures are useful for devices where charge separation is important, like solar cells or photocatalysts. In the quasi-type-II alignment, one carrier (usually the electron) spreads across both the core and the shell, while the hole stays in the core. This partial separation changes how the QD emits light and allows for tuning the radiative properties.[85]

Core-shell QDs with inorganic shells exhibit greater resilience (temperature, pressure, or chemical exposure) compared to those with organic compounds and can better withstand the processing conditions required for their integration into solid-state devices.[86,87] A wide variety of semiconductor materials can be used to prepare QDs with a core-shell structure. Heterojunctions from CdS QD cores with CdSe shells and the inverse CdSe QDs with CdS shells[86] can be both realized. It is not a requirement for the core-shell materials to share the same metal ions in their structure, and CdS/CdSe QD cores can be passivated by ZnS shells.[79,88,89]

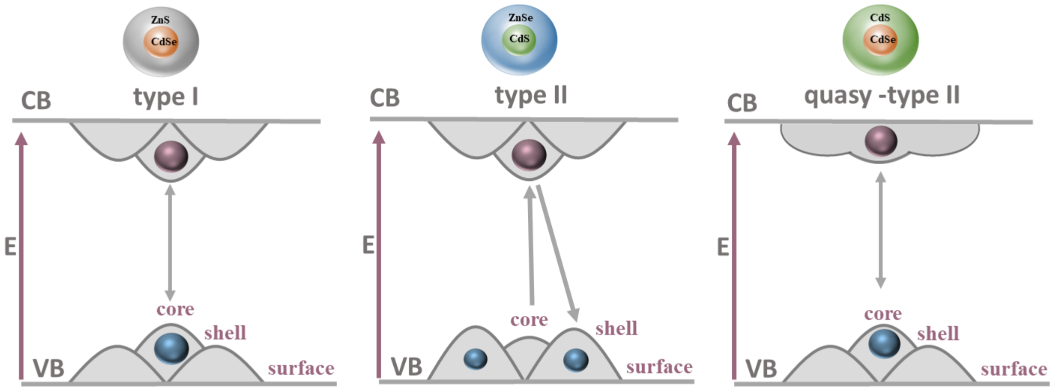

Figure 14. Schematic representation of core-shell quantum dot energy structures, type I structure, where both electrons and holes are confined in the CdSe core with a ZnS shell, type II showing the spatial separation of electrons and holes in different systems and quasi-Type II structure, where one carrier is partially delocalized across the core and shell (CdS/CdSe).[85]

The shell thickness in core–shell QDs strongly influences their PL efficiency and stability. In CdSe/CdS systems, thicker shells (0.5–2 nm) improve PL by better passivating surface defects. Optimized ZnS shells on CdSe cores can yield up to 88% PL quantum efficiency and enhanced thermal and UV stability.[90,91]

1.3.4 Charge carrier dynamics in CdSe/ZnS core-shell QDs

Manipulating and comprehending the dynamics of transient hot carriers is crucial for surpassing the efficiency boundaries of traditional solar cells.[90–93] These hot carriers rapidly relax (sub-ps) through various scattering events (carrier-carrier, carrier-phonon or carrier-impurity), which makes their extraction quite challenging. Prolonging hot carrier lifetime in these materials is either possible through the use of (i) high excitation [94,95] densities or (ii) different bottleneck or blockade effects.[69,96] The former strategy (i.e. hot-phonon bottleneck) was recently utilized in lead halide perovskites to achieve longer hot electron lifetimes.[97–101] In the case of Cd chalcogenides, the band structure with the various selection rules allows to prolong carrier lifetimes by forming blockade events (e.g., spin, Coulomb blockade) or by encouraging the formation of exotic quasi-particles (e.g., trions) that have a longer lifetime.[68] These processes require additional electron density in the band structure of the semiconductor as multiple carriers participate in them. Doping or alloying CdSe QDs with 'foreign' (nonnative elements to the host) elements (e.g., Sn, In, Ga, Cu)[75,102–106] can introduce filled states within the bandgap of the semiconductor, which in turn can significantly alter the decay of the excited state. Colloidal QDs with n-doped character can be potentially used for harvesting hot electrons.[102] Depending on the foreign element used, markedly different energy levels can be introduced into the semiconductor band structure. In case of Sn or In doped CdSe QDs, the introduced donor electrons are not excited into the CB at room temperature.[75,102,104] In stark contrast with Ga doping, here an increased donor electron occupation can be observed even close to room temperature.[107] It has also been demonstrated that Ga doped CdSe QDs have stronger temperature-dependent PL quenching and a shortened excitonic lifetime due to the increased dopant ionization above room temperature.[75] CdSe QDs with a similar n-type character were also achieved using a photochemical approach in the presence of a hole-scavenger under inert atmospheric conditions.[96] Under light doping conditions with above bandgap excitation, the presence of a Pauli spin blockade prolongs the hot electron lifetime to ~10 ps. In this case, an electron occupies the $1S_e$ state in the CB of CdSe. When this electron is subsequently excited with resonant light, the decay of the developing trions can be easily distinguished, which suggests a characteristic lifetime of ~460 ps. This lifetime agrees well with that of PL lifetime measurements (in the range of 740 ps).[108] In case of higher-level doping, the $1S_e$ state is filled by two electrons, and the resulting Coulomb blockade further increases the hot-carrier lifetime to 300 ps. It is worth noting that not only filled midgap states, but also unfilled energy levels can be introduced into the CdSe band structure. By using Cu^+ doping, the hot-electron lifetime is prolonged from ~0.25 ps to ~8.6 ps in doped CdSe QDs.[106] In this case, the introduced impurity-level lies closer to the VB of the semiconductor and participates in the hole capture process. In this manner, electrons are efficiently decoupled from the holes and hot electron relaxation is inhibited.

It is important to note that a complementary technique, temperature-dependent PL spectroscopy, is widely used to study photophysical processes in low-temperature regimes due to the prevalence of direct radiative recombination pathways (increased quantum yield) and prolonged lifetimes (>ns). For QD systems with multiple interfaces, often complex behavior can be observed, where thermal escape channels through the different interfaces must also be considered.[109] Temperature-dependent PL spectroscopy can be used to investigate the excited-state lifetime of organic ligand-capped CdSe QDs in the 1.3–300 K temperature range.[110]

1.3.5 Transition metal dichalcogenides

Transition metal dichalcogenides (TMDCs) based systems are also at the forefront of materials science. TMDC materials (e.g., MoS_2, WS_2) are layered 2D semiconductors with tunable electronic properties (transistors, photodetectors, LEDs, and solar cells, and show promise in sensing, catalysis, and quantum technologies like spintronics). TMDCs consist of layers with a structure of MX_2, where M is a transition metal (e.g., Mo^{4+}, W^{4+}) and X is a chalcogen (e.g., S^{2-}, Se^{2-}, or Te^{2-}). These layers are easy to exfoliate into monolayers or few layers because the van der Waals forces that hold them together are weak (noncovalent interactions between atoms or molecules). Monolayer TMDCs have direct bandgaps and have a bright PL emission. In contrast, multilayer structures have indirect bandgaps and emit less light. **Figure 15** shows this effect in WSe_2.

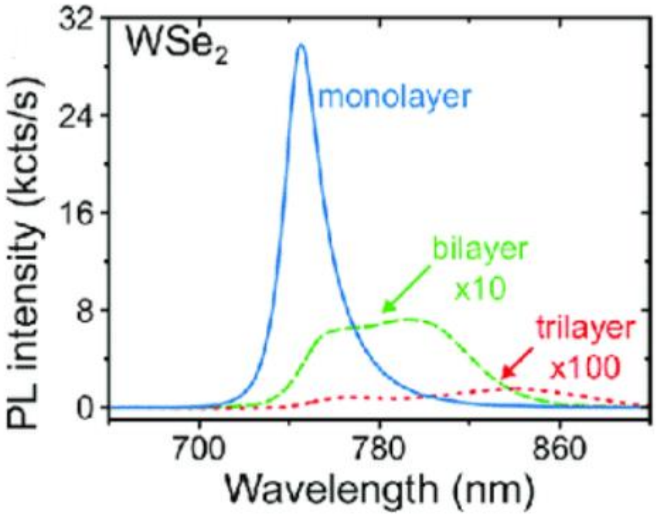

Figure 15. PL spectra of monolayer (blue), bilayer (green), and trilayer (red) Wse_2, showing how layer thickness affects optical emission. The bilayer and trilayer intensities are scaled by factors of 10 and 100, to emphasize the contrast with the monolayer.[111]

The bandgap tunability with layer thickness is crucial for optoelectronic applications. Monolayer TMDCs show two peaks in their PL spectra. These are referred to as the A and B excitons. They come from the spin–orbit splitting of the VB at the K point of the Brillouin zone. The A exciton has lower energy, while the B exciton appears at higher energy because the second VB is split by spin–orbit coupling.

TAS studies have revealed that carrier cooling in TMDCs occurs on extremely short timescales, but at high excitation densities, the hot-phonon bottleneck effect can significantly slow down this process.[112] Rapidly generated optical phonons reabsorb energy from carriers, slowing down carrier cooling. This impacts applications in hot-carrier photovoltaics and thermoelectric devices, photodetectors, field-effect transistors (FETs), and sensors. The large surface-to-volume ratio and tunable optical properties make them especially effective in these applications. Although monolayer MoS_2 absorbs mainly in the visible range, it can also show TA below its bandgap. Exciton A appears in the visible range around 660 nm, and exciton B at 610 nm. It is showed[113], that TA signals appear in the near-infrared region (0.86–1.4 μm). At shorter wavelengths (e.g., 0.92 μm), the signal rises rapidly due to free carriers. At longer wavelengths (e.g., 1.26 μm), the rise is slower, which suggests exciton formation. These results indicate that excited states in MoS_2 can absorb light well below the bandgap, not only in the visible range. This could enable the development of new NIR devices based on 2D materials.

In monolayer Wse_2, the A exciton appears at around 750 nm, while the B exciton appears near 630 nm. Monolayer Wse_2 also exhibits fast and efficient exciton dynamics, which can be investigated by using femtosecond TA microscopy.[114] The sample can be excited with a 405 nm pump pulse. In the monolayer, the excitons lived for about 18 ps. In bulk Wse_2, the excitons lived longer, for ~160 ps. These results demonstrate that excitons exhibit distinct behavior in monolayers and bulk materials. The monolayer supports faster and more mobile excited states. Together with the MoS_2 results, this shows that monolayer TMDCs have rich and ultrafast photophysics.

2. Aims

During my research, I aimed to find answers to the following questions and solve the following scientific/development problems:

- *Is it possible to develop a measurement setup that allows temperature control while performing TAS experiments at high temperatures?*
- *What role does temperature play in the charge carrier dynamics of CdSe/ZnS QDs? How will the recombination pathways be affected at high temperatures?*
- *What is the impact of Ga-alloying on the excited-state lifetime of CdSe/ZnS QDs?*
- *Can the TAS setup be modified to perform TRS measurements? Can this technique be used to investigate the impact of a pentacene film on the decay kinetics of A and B excitons in transition-metal-dichalcogenide/pentacene thin films?*
- *How can preliminary findings related to the effects of fundamental beam dispersion on THz radiation generation be used to develop a new THz probe path in the TAS setup?*

As a first step, I aimed to extend the capabilities of the TAS setup at ELI ALPS by incorporating temperature control to investigate the temperature-dependent charge carrier dynamics in CdSe-based QDs. The developed system enabled TAS measurements across the 30–130 °C temperature range, using liquid samples to probe the effects of temperature changes on charge carrier behavior. Initial measurements in CdSe/ZnS QDs showed that temperature had negligible effect on excited-state lifetime but strongly influenced carrier recombination, which suggest trion formation. Then, I explored the impact of Ga incorporation into the structure of CdSe/ZnS QDs, which further promotes the formation of trions and induces a Coulomb blockade in the relaxation dynamics, effectively prolonging the hot-carrier lifetime. In the next phase, I modified the detection geometry of the TAS setup to enable transient reflection measurements. This technique was employed to study the exciton dynamics in TMDC/pentacene thin films deposited on gold substrates. Specifically, in MoS_2/pentacene and WSe_2/pentacene heterojunctions, the presence of the pentacene film was found to have a moderate influence on the decay kinetics of A and B excitons. Furthermore, I set a more distant goal to develop a THz probe path in the TAS setup, building on previous work, where I investigated the effects of fundamental beam dispersion on THz generation.

3. Materials and Methods

3.1 Measurement methods

3.1.1 Transient absorption spectrometer

The TAS measurements were conducted using a dedicated experimental endstation at ELI ALPS Laser Research Institute.[115] **Figure 16** shows the schematic illustration of the experimental setup.

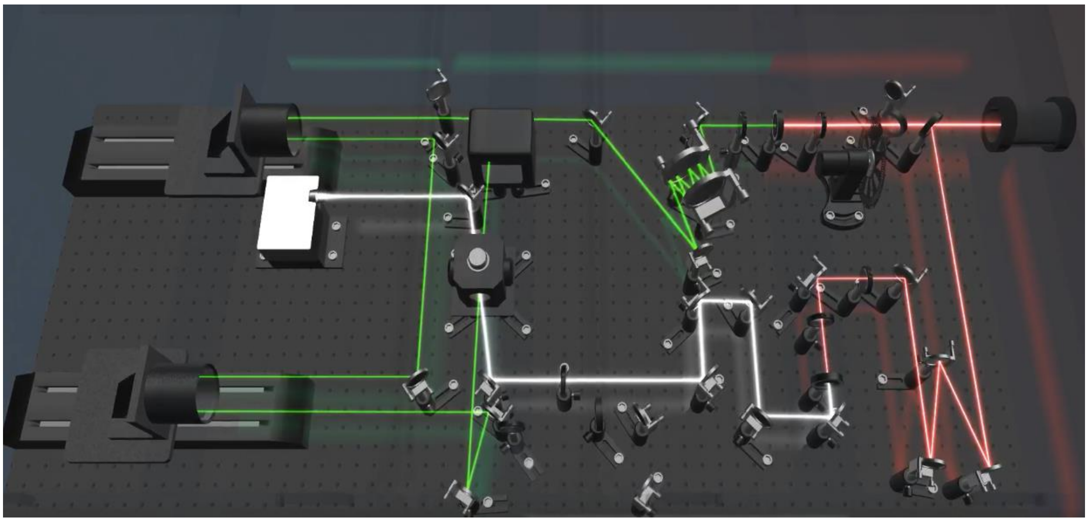

Figure 16. The 3D layout of the TAS setup: the fundamental beam (red) is split into pump (green) and probe (white) beams. The chopper and a delay stage are integrated for recording the PUMP ON/OFF states and for temporal control. The liquid sample holder and detector can be seen at the end of the beamlines.

The light source was the HR-1 laser[116], a few-optical-cycle laser system, which generates 6–30 fs pulses at a repetition rate of 100 kHz. Its central wavelength is centered at 1030 nm, and the pulse energy is approximately 1 mJ. The ytterbium fiber chirped-pulse amplifier outputs 250 W. There are two postcompression stages based on the multipass cell technique, which compress the original 270 fs pulses to 30 fs and then to 6 fs pulses. This laser system has outstanding stability with the following parameters: average power fluctuation of 0.1%, peak-to-peak energy variation of 0.7%, and pointing stability of 2.3 μrad (M^2=1.1 and S=0.98). A part of the full beam was directed to the TAS setup with a beam splitter placed after the first postcompression stage. This beam had specific characteristics, with a pulse energy of 100 μJ and an average power of 10 W. The spectral bandwidth ranged from 980 to 1080 nm, and the transform-limited pulse duration was 30 fs. To optimize this pulse, additional chirp mirrors were used at the entrance of the experimental setup, and the incoming pulses were checked with a commercial APE PulseCheck autocorrelator. To fine-tune the power within the range of 0 to 10 W without impacting the spectrum and pulse duration, we implemented a distinct power control mechanism comprising of a thin-film polarizer and an achromatic half-wave plate.

The laser pulse entered the experimental setup, where it was divided in a 90/10 ratio using a beamsplitter (BS). Here, 90% of the beam was allocated for the generation of the pump beam, while the remaining 10% was used for the probe beam. The pump beam was generated by frequency doubling with a Type-I BBO crystal (Eksma optics, 0.2 mm). The resulting pulse had a wavelength centered at 515 nm. To compensate the GDD effects caused by transmissive optical elements in the frequency-doubled beam path, the pump beam travelled along a path including chirped mirrors (Ultrafast Innovation HD1820) eight times. This step was important to maintain the pulse duration until it reached the sample, which could be monitored with an autocorrelator (APE PulseCheck-50). Ultrafast mirrors with low GDD (Thorlabs UM10-45G) were used to split the green and IR components of the beam. Notably, the temporal resolution of the instrument at the sample holder was approximately 60 fs. This value was influenced by the transmission optics, resulting in a slightly longer pulse duration and a lower temporal resolution. The pump beam was focused to achieve an excitation fluence of 0.2 mJ/cm^2, with its focal point positioned after the sample, while the probe beam was focused directly inside the cuvette. The white light in the probe path was generated by focusing the beam on a 2 mm thick sapphire crystal. The focused probe beam had a smaller size (60 µm × 50 µm) than the pump beam on the target. This setup is flexible because it can use different light sources both for the pump and probe beams: 1030 nm, 515 nm, 343 nm, 257 nm, white light, and THz radiation. These combinations are common in pump–probe experiments.

The setup used an Ocean Insight FX fiber optic spectrometer, which could record up to 2,000 spectra every second. The spectrometer was triggered at 4000 Hz and had a 30 µs integration time and averaged 2,000 to 10,000 spectra. This allowed for the quick and accurate recording of the TAS spectra during the experiment. An optical chopper running at 2000 Hz ensured the recording of the pump OFF state. By subtracting the spectra recorded in the pump-on and pump-off states, we obtained the TAS signal. We controlled the sample temperature using a QPod sample holder, which works in the range of –10 °C to 130 °C.

In case of the QD dispersions, we heated the samples to 130 °C under an argon flow to avoid reaction with oxygen at high temperatures. Before recording the TAS spectra, we allowed the temperature to stabilize for at least five minutes and kept stirring the sample with a magnetic stirrer. After measuring the TAS spectra, we gradually lowered the temperature to the next set point. We limited the maximum temperature based on the boiling point of xylene, which is around 140 °C. We kept the flow of argon low to avoid solvent evaporation.

3.1.2 Transient reflection spectrometer

A notable feature of this equipment is its adaptability, allowing swift transitions between the TAS and transient reflection spectroscopy (TRS) modes based on the specific requirements of the sample or material under observation. **Figure 17** shows the TRS layout with the spatial filtering pinhole and the alternative beam path of this configuration.

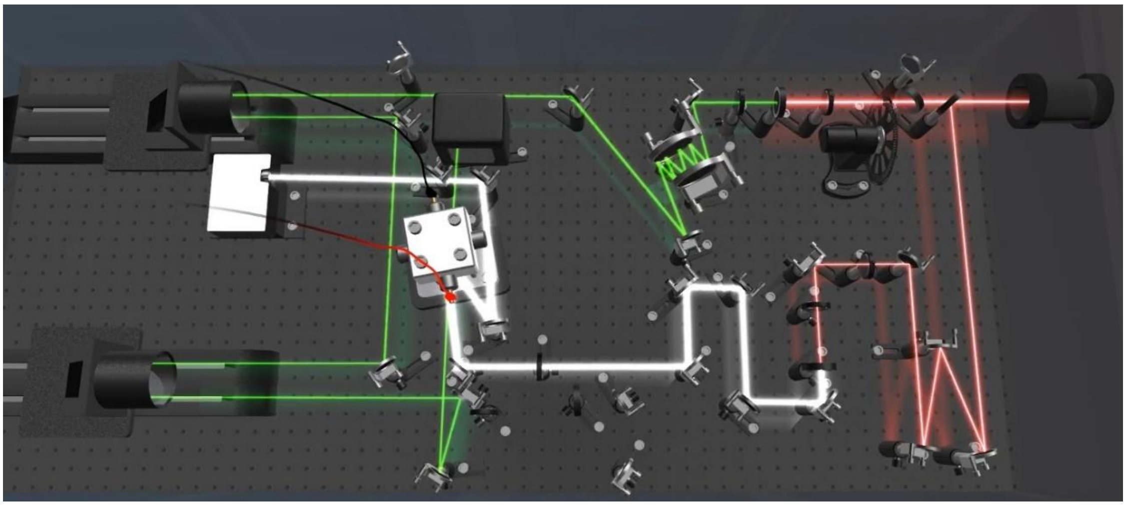

Figure 17. The 3D layout of TRS setup: The fundamental beam (red) is split into a pump (green) and a probe (white) beam. The thin film sample holder with the reflection beam path and detector can be seen at the end of the beamlines.

In this configuration, we changed the temperature-controlled liquid sample holder for a 3D linear stage, designed for thin film samples with good reflectivity. To switch to TRS, we collected the light after it was reflected from the sample surface and guided it into the detector. This maneuver requires an adequate amount of reflected light from the sample surface. Furthermore, multiple reflections can also occur (e.g., thick substrates, cuvette, or cell walls etc.). As these extra reflections can interfere with the signal, we carefully adjusted the setup to only collect the reflections originating from the front sample surface. We used a 10 µm pinhole to perform spatial filtering, which helped us select only the focused spot of interest. Spatial filtering is important in TRS because it reduces background noise and ensures that we detect the signal from the exact region we want to study.

3.1.3 Visible pump – THz probe TAS setup

The primary goal of this project was to generate THz radiation for ultrafast experiments and improve the TAS setup by incorporating the capability for THz probing. Although THz radiation can be produced with various methods, optical rectification (OR) and the linear electrooptic (EO) effect (Pockels effect) are the most common for broadband generation and the detection of THz radiation through EO sampling. OR involves the generation of a direct current or polarization when intense laser beams pass through a crystal. On the other hand, the linear EO effect describes the change in the polarization of a crystal due to an applied electric field. The optical layout of our group's THz setup is illustrated in **Figure 18.**

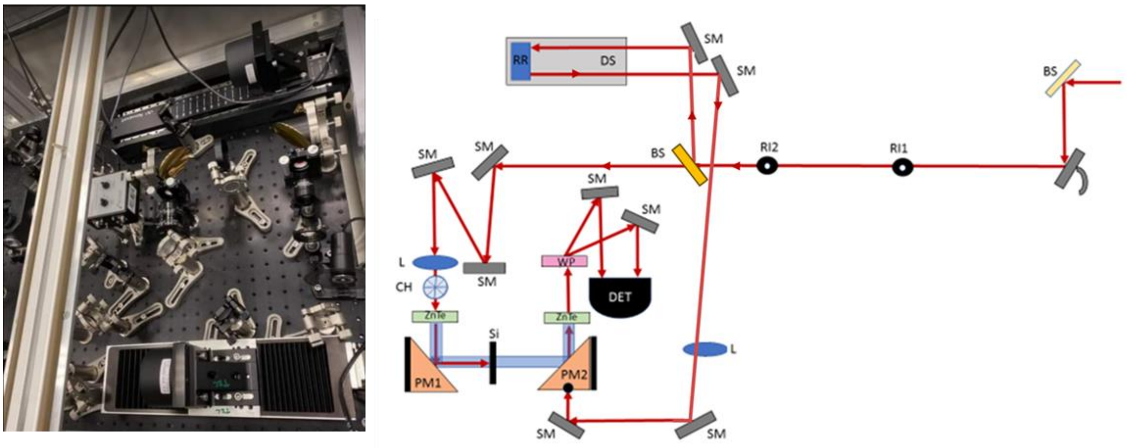

Figure 18. Photograph and schematic layout of the THz probe generation setup. The fundamental beam is split and directed through a delay stage (DS) and a retroreflector (RR) for temporal adjustment. The beam path includes beamsplitters (BS), silver mirrors (SM), and relay irises (RI1, RI2) to maintain spatial and temporal alignment. The THz probe is generated via optical rectification in a ZnTe crystal, with the pump beam focused using parabolic mirrors (PM1, PM2). Electrooptic sampling is performed using a second ZnTe crystal and a silicon (Si) wafer to separate the probe. After the Wollaston-prism (WP) and polarizer,

the beam is directed to the detector (DET). Lenses (L) and a chopper (CH) are used for beam shaping and modulation.

In this configuration, two reference irises (RI1 and RI2) come into play after the beamsplitter divides the beam into two equal parts, crucial for connection with the TAS setup. After the irises, another beamsplitter (BS) divides the beam into a probe and pump arm. The probe arm utilizes about 10% of the incoming energy, while the pump arm employs the remaining 90%. To scan the temporal overlap, a delay stage (DS) is integrated into the probe arm, incorporating a retroreflector (RR) and two 1-inch silver mirrors (SM). The beam is focused by a 170 mm fused silica lens (L). In the pump arm, the beam is focused on a ZnTe crystal using a fused silica lens with a 5 mm focal length. Then, it is led through the chopper. THz radiation is generated by OR in the pump arm. The beam is collimated using 2-inch and 5-inch focal length gold parabolic mirrors, and a silicon plate (Si) is utilized to filter out specific THz spectral components. The probe and pump beams converge on the second parabolic mirror (PM2) with a hole. Both beams are then focused on the second ZnTe crystal. Subsequently, the beam passes through a block containing a Wollaston prism (WP) and a λ/2 waveplate. EO sampling is employed using a balanced detector and Labview software for THz signal scanning.

The sampling process relies on the static EO effect, where the application of a direct current field in an EO crystal induces a change in the refractive index. Zinc-blende crystals, including ZnTe and GaP (to be used later in our research), exhibit the largest EO for the direct current field, causing the most significant difference in the refractive index. The signal from the photodetector is led into the lock-in amplifier for phase-sensitive detection. Phase-sensitive detection requires signal tagging or modulation at a specific frequency, accomplished with an optical chopper operating at 6 kHz.

3.1.4 Data analysis and fitting protocol

We fitted the GSB decay curves from the TA/TR measurements using a multiexponential model:

$$y(t) = y(0) + \sum_{i=1}^{n} A_i e^{\frac{-t}{t_i}} \quad , \tag{24}$$

where t is the pump–probe delay time, and $y(t)$ is the time dependent TA signal at the GSB maximum. A_1 and A_2 are the relative contribution of each decay channel to the total signal and are therefore proportional to the fraction of excited charge carriers undergoing relaxation through the respective processes characterized by lifetime t_i. The interpretation is system-dependent. In case of QD dispersions or solid-state heterojunctions, the decay components can be associated with entirely different processes, such as surface trapping, energy transfer, or interfacial charge separation, depending on the material structure and measurement conditions. Therefore, in each chapter and for each material system presented in this work, we explicitly state how the fitted components are assigned to the relevant physical processes.

3.1.5 Material characterization

Transmission electron microscopic (TEM) investigation was performed using a FEI Tecnai™ G2 20 X-Twin type instrument, operating at an acceleration voltage of 200 kV. Steady-state and time-resolved photoluminescence (TRPL) measurements were carried out using a Horiba DeltaPro with a 467 nm laser source.

3.2 Chemicals

3.2.1 QD dispersions

The CdSe QD samples used in these studies were prepared in the laboratory of my supervisor, Dr. Viktor Chikán, as part of the PhD research of his former student, Christopher Tuinenga. The samples provided an excellent model system for the detailed investigation of charge carrier dynamics.

The chemicals were used in their commercially available forms, except for hexadecylamine (HDA), tri-n-octyl phosphine (TOP), and tri-n-octyl phosphine oxide (TOPO), which underwent purification through distillation at 2 torr. $GaCl_3$, diethylzinc, hexamethyldisilithiane, and tri-n-octyl phosphine (TOP) were stored in an inert atmosphere glovebox for optimal conditions.

Toluene (spectrosol grade, Carlo Erba) and xylene (a mixture of isomers, Lachner) served as the solvents for diluting the samples, and these mixtures were frozen in HDA. The single source precursor $Li_4[Cd_{10}Se_4(SPh)_{16}]$ was prepared following Cumberland's method. The synthesis and handling procedures ensured the purity and integrity of the chemicals used in the experiments.[117]

Synthesis of the CdSe core

Ga-alloyed and pure CdSe cores were synthesized from $Li_4[Cd_{10}Se_4(SPh)_{16}]$ single-source precursor in HDA with $GaCl_3$ as the doping agent. During the process, 50 g of distilled HDA and 0.6 g of the single-source precursor were loaded into a three-neck flask and transferred into a glovebox, where the $GaCl_3$ was added. The loading percentages of foreign elements are based on the total cadmium content of the reaction. In our case, the reaction flask was purged with Ar for 20 minutes before it was carefully heated to 120 °C to minimize temperature overshoot. The solution was stirred at 120 °C for 12 hours. Then, the temperature was increased to 240 °C, and the particles grew to their final size over 3 hours.[104]

The growth of a protective ZnS shell

The Zn/S stock solution is prepared by combining 7 mL of diethylzinc with 1 mL of hexamethyldisilithiane and 32 mL of distilled TOP. Both TOPO and 2-aminopropanol are used directly without any purification. The process for ZnS shell growth involves the following steps: a solution containing 2 mL of the Zn/S stock solution, diluted with 8 mL of TOP, is dispensed using an automated syringe pump over 30 minutes. Subsequently, shell growth occurs for one hour at 250 °C. After a cooling phase, another layer of shell material is grown by repeating the dropwise injection at 250 °C. This sequential shell growth process is iterated four times. The samples are then stored at room temperature and can be further diluted with toluene or xylene for subsequent measurements.

3.2.2 TMDC samples

The TMDC samples were provided by our user group from the MESA+ Institute for Nanotechnology, University of Twente, led by Pavel A. Markeev and Michel P. de Jong. They provided the model system for investigating thin-film samples and enabled the detailed study of charge carrier dynamics in layered molecular-semiconductor heterojunctions in TRS.

Single-layer MoS_2 and WSe_2 crystals were grown using a modified chemical vapor deposition method. We used thermally oxidized silicon substrates with a 300 nm SiO_2 layer and low surface roughness. To introduce the sulfur and selenium precursors, a Knudsen-type effusion cell was applied, which ensured controlled delivery during growth.

After synthesis, the monolayer crystals were transferred on a gold substrate using a poly methyl methacrylate-assisted (PMMA) protocol. A 200 nm thick PMMA film was spin-coated on top of the original TMDC samples. Then, the substrate was floated in a potassium hydroxide solution to dissolve the SiO_2 layer and release the PMMA-supported TMDC film. The floating layer was washed with ultrapure water, transferred on the gold substrate, baked at 90 °C, and the PMMA was removed with acetone and isopropanol rinsing.

To prepare the organic layer, a 20 nm thick pentacene film was deposited on a water-soluble poly(acrylic acid) (PAA) layer, which was previously spin-coated on borosilicate glass. A low evaporation rate was used (0.1 Å/s) to achieve highly ordered nanosheets. After deposition, the PAA was injected under water to delaminate the pentacene film, which floated to the surface. This film was transferred on the gold substrate with the TMDC layer and was allowed to dry under ambient conditions.

4. Experimental results

4.1 Temperature-dependent TAS measurements of Ga-alloyed CdSe/ZnS QDs

4.1.1 Optical and morphological characterization

Readily received CdSe/ZnS core-shell QDs were used for the temperature-dependent TAS studies, where the CdSe core was subjected to sequential ZnS shell growth as detailed in our previous study.[74,75] The sequential growth process ensures that the surface traps on the CdSe are filled and covered with ZnS.[79] To avoid self-purification of the QDs, the Ga atoms were incorporated at a low temperature (120 °C) into the CdSe cores before growing the ZnS shell. For this alloying process, the CdSe synthesis was modified by adding an appropriate quantity of $GaCl_3$. Consequently, samples with nominal Ga contents of 2.5%, 7.5%, and 15.0% were studied. The primary function of the ZnS shell in each case was to minimize the impact of nonradiative recombination on overall charge carrier dynamics by passivating surface trap-states within these materials.[79] The full range of the static UV-Vis absorption spectra of the QD samples is shown in **Figure 19A**. The presence of ZnS can be observed as a large absorbance feature on the recorded spectra. However, as the probe light lacks these spectral components (i.e., below 450 nm), our focus shifted to the characteristic absorption of CdSe. Furthermore, the pump energy used in this experiment does not induce transitions to the higher energy bands attributed to the ZnS shell. These spectra suggest a slight blueshift with increasing Ga content, possibly indicating the thinning of the passivating shell.

Before performing temperature-dependent TAS experiments, it is crucial to assess the heat stability of the systems. **Figure 19B** shows the UV-Vis absorption spectra of CdSe/ZnS and CdSe:2.5% Ga/ZnS QD dispersion before and after high temperature conditioning (130 °C, t=1 hour). It is apparent from these measurements that the optical properties of all these samples remained unchanged for the pristine and the CdSe:2.5% Ga/ZnS samples in the temperature range of the TAS measurements presented later.

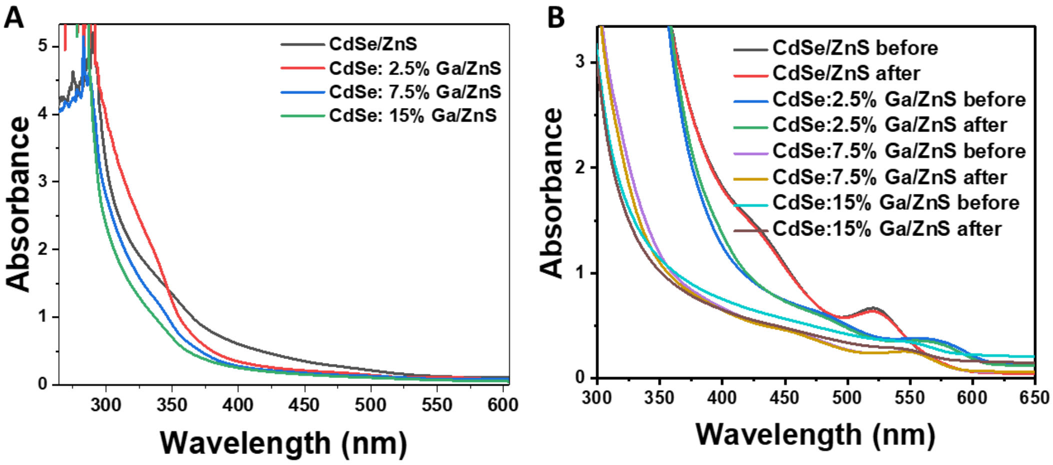

Figure 19. A: Static UV-Vis absorption spectra of the investigated samples in the full spectral range of interest. The spectra include the excitonic peaks associated with QD transitions and the characteristic absorption edges of the core and shell materials. **B:** Steady-state UV-Vis spectra of the QD samples before and after 130 °C heating for 1h to check the stability of the systems.

In **Figure 20A**, the individual UV-Vis spectra for each composition are shown, focusing on the excitonic transition regime. **Figure 20B** shows the normalized absorbance spectra, where the peak positions at 520 nm, which matches the typical excitonic transitions of the base material.[118] When 2.5% Ga is incorporated, the peak shifts to 574 nm, showing that even a small amount of alloying changes the band structure. At 7.5% alloying, the excitonic peak shifts further to 598 nm. However, at 15% alloying, the peak shifts back slightly to 584 nm. This reverse shift can be the result of structural disorder induced by the Ga incorporation or saturation effects. We can see that alloying allows us to tune the excitonic properties of the material, but higher concentration may introduce unwanted effects.

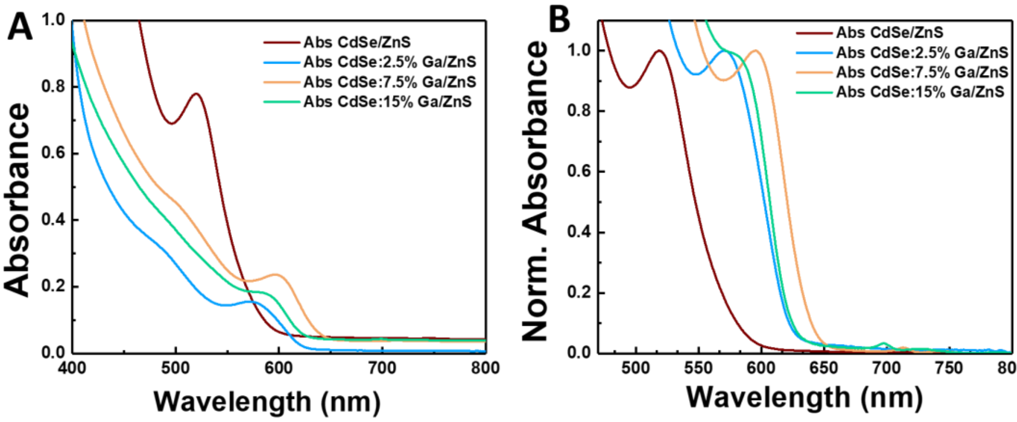

Figure 20. A: UV-Vis spectra and **B:** normalized UV-Vis spectra of CdSe/ZnS, CdSe:2.5% Ga/ZnS, CdSe:7.5% Ga/ZnS, and CdSe:15% Ga/ZnS samples.

PL spectroscopy was carried out to evaluate the light emission properties of the QD samples. **Figure 21A** shows the normalized PL spectra of the Ga alloyed QD samples, which were recorded with 467 nm excitation. All PL spectra have similar shapes, suggesting that band-edge emission dominates in all samples. The pristine sample shows emission at ~530 nm. In the case of Ga alloying, the PL peak shifts to longer wavelengths: ~585 nm for 2.5%, ~600 nm for 7.5%, followed by a slight blueshift to ~584 nm in the 15% sample. This trend suggests that an increasing Ga content may cause an initial bandgap narrowing. At higher doping levels, there is a break in the trend, possibly due to alloying-induced disorder or phase separation, as also discussed in the UV-Vis properties of the alloyed samples. Interestingly, the sample alloyed with 15% Ga exhibited an additional peak at lower wavelengths, which is attributed to some pristine CdSe/ZnS remaining in the dispersion rather than to additional transitions, such as the 1Pe–1Ph transition, prompted by the complete filling of the $1S_e$ energy level.[119] **Figure 21B** compares the normalized absorbance and PL spectra of pristine and 2.5% Ga-alloyed samples. Both spectra exhibit a redshift upon alloying. This confirms that Ga incorporation modifies the electronic structure by lowering the bandgap. No additional absorption peaks at longer wavelengths were observed, signaling that the impurity states were likely filled. These results show that Ga alloying can shift both the absorption and emission spectra, but too much Ga can trigger other effects that stop further redshift.

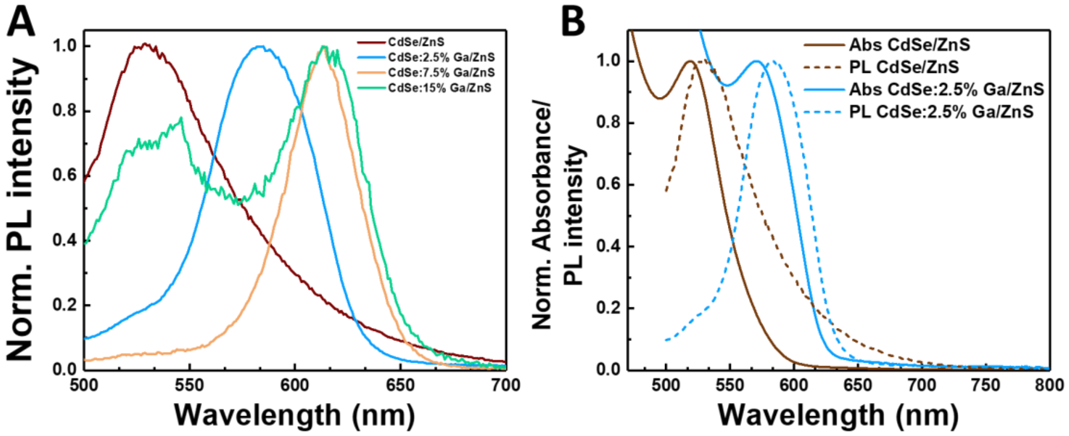

Figure 21. A: The normalized PL intensity of CdSe/ZnS, CdSe:2.5% Ga/ZnS, CdSe:7.5% Ga/ZnS, and CdSe:15% Ga/ZnS samples. **B:** Comparison of the normalized absorbance and the normalized PL intensity.

To elucidate the lifetime of photo-excited charge carriers PL lifetime measurements were carried out, as shown in **Figure 22A**. We recorded the decay traces at the respective PL peak maxima of the samples. To characterize the average PL lifetime of the samples, the PL decay curves were fitted with a tri-exponential function. The obtained fitting parameters are summarized in **Table A1**. The Ga content dependence of the calculated intensity-weighted average lifetime is shown in **Figure 22B**. The untreated CdSe/ZnS samples exhibited a multiexponential decay pattern, indicating either an incomplete passivation of surface trap states in these samples or the influence of multicarrier processes due to the diminutive size of the QDs. The PL lifetime was notably shorter in the CdSe/ZnS QDs compared to the Ga-containing samples. The sample containing 7.5% of Ga displayed the longest PL lifetime. Based on the properties of CdSe QDs, this effect can be attributed to the convolution of three separate processes: (i) the addition of the Ga precursor to the synthesis mixture can passivate the surface trap states before the ZnS shell is deposited, (ii) the presence of Ga-related occupied impurity states facilitates the formation of negative trions in these samples, and (iii) size changes related to the increasing CdSe core size with the incorporated Ga. The length of the PL lifetime is first and foremost determined by increasing QD sizes and the concomitant decrease in trapping depths.[120] Size affects the trion's Auger decay in a similar manner, which explains the longer PL lifetime in Ga-alloyed CdSe QDs.[121]

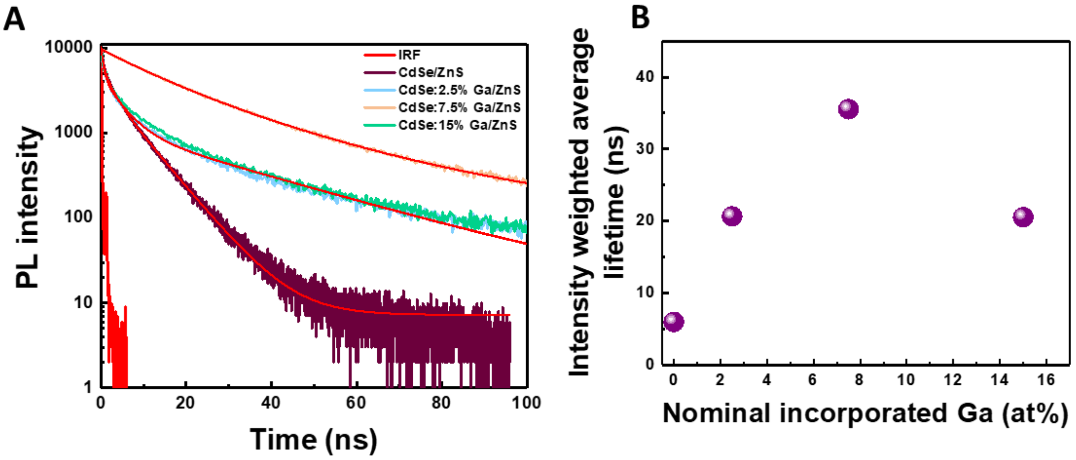

Figure 22. A: PL decay curves of CdSe:Ga/ZnS samples at 467 nm excitation. **B:** The intensity weighted average lifetime of the pristine, the CdSe:2.5% Ga/ZnS, the CdSe:7.5% Ga/ZnS and the CdSe:15% Ga/ZnS samples.

To assess the size of the prepared QD samples, high-resolution transmission microscopy (HR-TEM) measurements were performed. The recorded images, shown in **Figure 23,** indicate that the average core size increased with Ga content. **Table 3** shows the average core size with standard deviation. The pristine CdSe/ZnS QDs had an average diameter of 3.9 nm. When alloyed with 2.5% Ga, the size increased to 4.3 nm, and further to 5.4 nm and 6.1 nm for the 7.5% and 15% Ga samples, respectively.

Table 3. The determined sizes and their standard deviation in case of CdSe/ZnS pristine, CdSe:2.5% Ga/ZnS, CdSe:7.5% Ga/ZnS, CdSe:15% Ga/ZnS samples.

	CdSe/ZnS	CdSe:2.5%Ga/ZnS	CdSe:7.5%Ga/ZnS	CdSe:15%Ga/ZnS
determined size	3.9	4.3	5.4	6.1
standard deviation	1.6	0.9	1.1	0.9

These size changes can be correlated with the redshift observed in the static UV-Vis absorption spectra, especially in the position of the $1S_e$–$1S_h$ transition. The larger QD cores show reduced quantum confinement, which can indicate a narrower bandgap and thus longer wavelength absorption and PL. Size distribution narrowing in alloyed samples suggests that Ga incorporation may also help control nucleation and growth during synthesis, and can ultimately yield more uniform nanocrystals. HR-TEM analysis thus confirms that the observed optical changes are induced not only by the electronic effects of Ga doping but also by the structural change of the QDs.

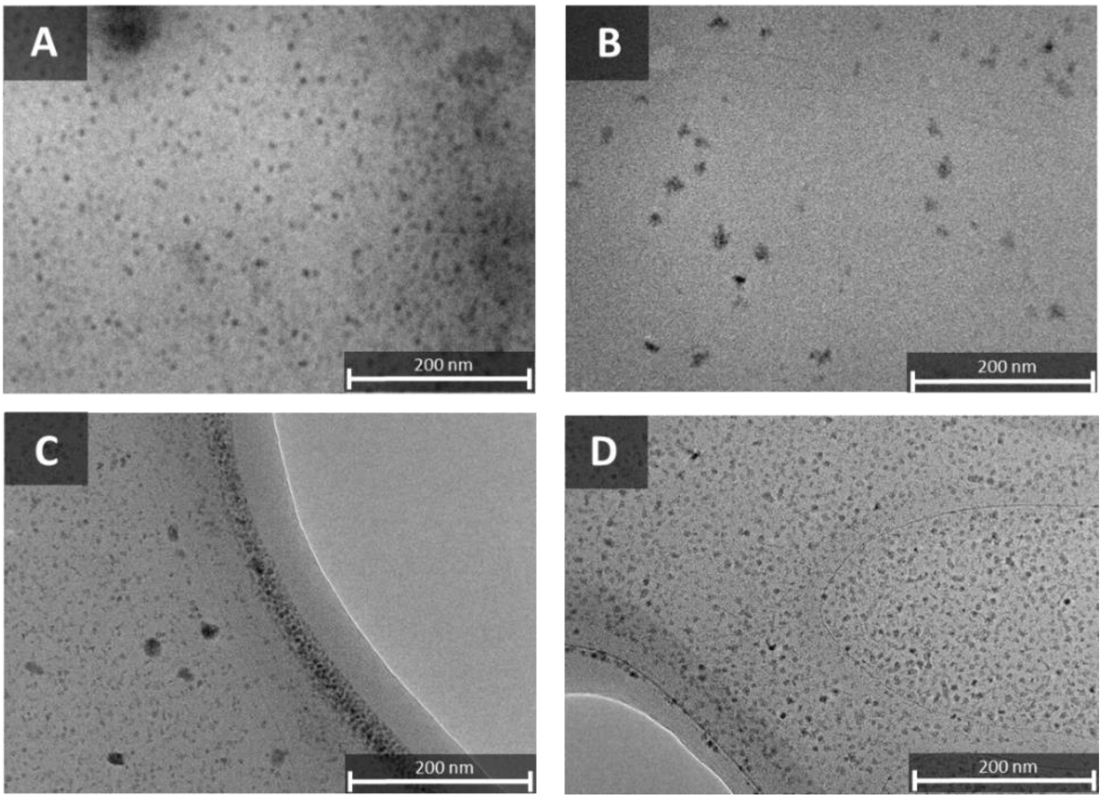

Figure 23. HR-TEM images of **A:** pristine CdSe/ZnS, **B:** CdSe:2.5% Ga/ZnS, **C:** CdSe:7.5% Ga/ZnS, **D:** CdSe:15% Ga/ZnS samples.

Size distribution graphs were obtained from HR-TEM images. These reveal the uniformity of the QD samples in each case and are shown in **Figure 24**. The pristine CdSe/ZnS sample had the widest size distribution. When we incorporated Ga into the structure, the size distributions became narrower. The determined average QD size for the 2.5% and 15% Ga samples both had a 0.9 nm standard deviation, while the value for the 7.5% sample was 1.1 nm. This shows that Ga reduces particle size distribution, which in turn leads to sharper absorption and emission peaks. The graphs confirm that Ga alloying not only changes the size but also improves size control during synthesis. All results are consistent with the previous studies.[74,104]

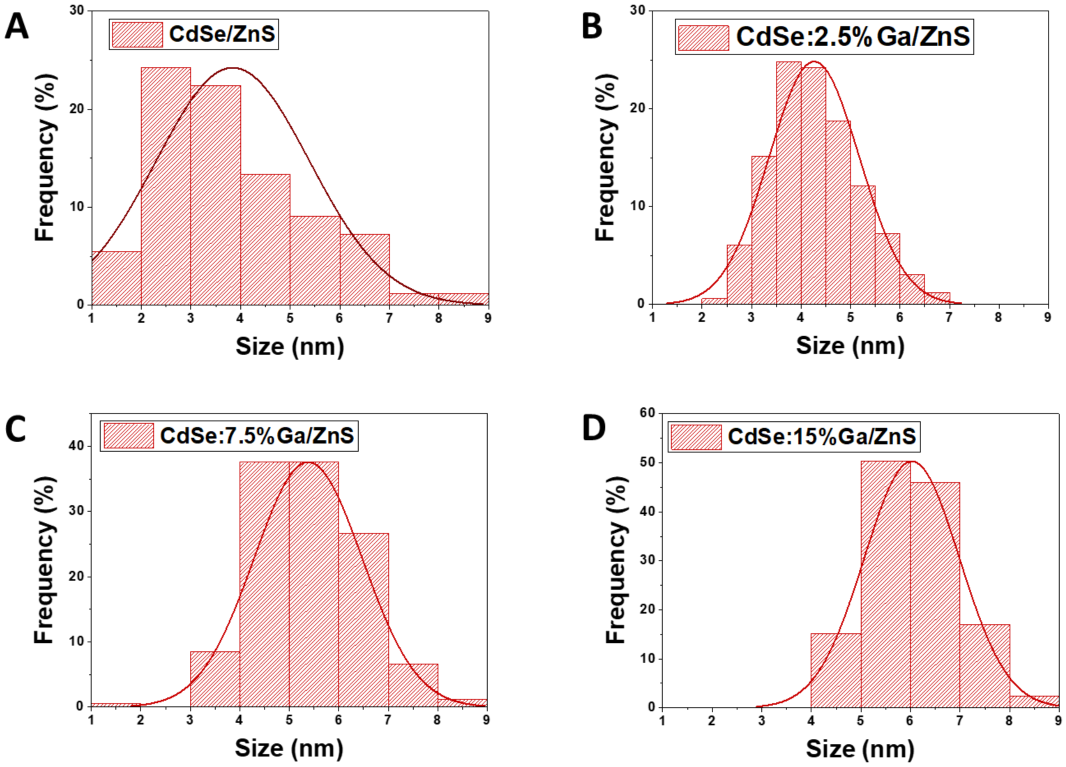

Figure 24. Size distribution of individual QDs (n=200) in **A:** CdSe/ZnS pristine, **B:** CdSe:2.5% Ga/ZnS, **C:** CdSe:7.5% Ga/ZnS, **D:** CdSe:15% Ga/ZnS samples.

Tauc analysis[122,123] can be used to determine the optical bandgap of a material based on its absorption spectrum. A Tauc plot typically involves plotting $(\alpha h\nu)^2$ against the photon energy $h\nu$ and extrapolating the linear portion of the curve to the x-axis intercept to determine the bandgap energy. If the exponent is 2, it indicates a direct allowed transition, while an exponent of ½ corresponds to an indirect allowed transition. Tauc plot equation for direct transition:

$$(\alpha h\nu)^2 = B(h\nu - E_g)\ , \tag{23}$$

where α is the absorption coefficient, $h\nu$ is the photon energy, E_g is the bandgap energy, and B is a material constant. **Figure 25A** shows the plot, where the linear portion of the curve was extrapolated to the x-axis intercept to determine the bandgap energy. **Figure 25B** shows the determined direct bandgap energies of different Ga-alloyed samples (2.5%, 7.5%, 15%).

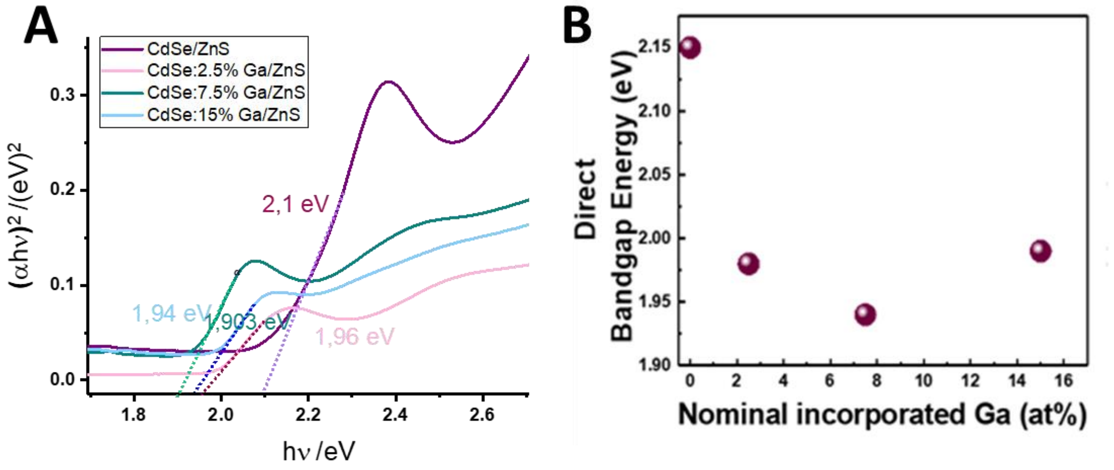

Figure 25. A: Tauc plots, where the $(\alpha h\nu)^2$ is plotted as a function of the photon energy $h\nu$ in the case of all samples. **B:** The determined direct bandgap energies of different Ga-alloyed samples (2.5%, 7.5%, 15%).

In a CdSe/ZnSe core-shell QD, saturation means that the electrons and holes reach their limit in number. Particles are packed closely together and therefore the interaction is weak. As a result, the special properties of QD become visible. Saturation can also change the energy levels and band edges, which affects how the material behaves electronically and optically. The emission characteristics of the quantum dot-bound light may change and influence factors such as emission efficiency or the spectrum of emitted light. Extreme carrier density may force QDs to aggregate, further changing the material's structure and properties. These effects can also alter the optical observability of quantum dot-bound particles, influencing the material's optical characteristics and chemical sensitivity. The observed shift tends to reach a saturation point beyond alloying levels of 7.5%. Additionally, these measurements suggest that the energy levels associated with Ga alloying are filled, as there are no extra absorption features visible in the UV-Vis spectra at longer wavelengths, which are typical of unoccupied midgap states.

4.1.2 Temperature-dependent TAS of CdSe/ZnS QDs alloyed with Ga

To observe the effect of Ga incorporation on the deactivation of the excited state at short timescales we conducted TAS measurements in xylene at five different temperatures ranging from 30 °C to 130 °C, as shown in **Figure 26.** Prior to the measurements, the UV-Vis absorbance of the QD dispersions was adjusted to ~ 0.5, and the pump wavelength was set to 515 nm to ensure a similar number of excited carriers in all cases.

Figure 26A shows the TA spectrum of the pristine CdSe/ZnS QDs recorded at 3 ps. The GSB signal is centered around 560 nm and exhibits a relatively sharp and well-defined peak, indicative of the narrow size distribution and homogeneous nature of the unalloyed QD sample. As temperature increases from 30 °C to 130 °C, a redshift is observed, moving the bleach maximum to longer wavelengths. This can be caused by the thermal reduction of the bandgap in CdSe, which is a well-known semiconductor property. Bleach intensity becomes stronger with increasing temperature, due to the thermal promotion of the $1S_e$–$1P_e$ state, which increases excited-state population in pristine QDs. **Figure 26B** shows the GSB peaks of 2.5% Ga-alloyed system, which is near 580 nm but shows a noticeably broader profile than the pristine case. The bleach maximum is shifted further to the red. This shift is mainly attributed to the slight increase in QD size due to Ga incorporation. Here, the GSB is broader than in the pristine case due to slight inhomogeneities caused by alloying. Although a redshift is still seen with increasing temperature, it is much less significant compared to the pristine sample. Bleach intensity decreases with increasing temperature, because Ga-related impurity levels release electrons into the CB, leading to state-filling and reduced excitation probability at the CB edge. **Figure 26C** shows the 7.5% Ga-alloyed sample. Here, the GSB maximum is shifted even further to the red, close to 590 nm, consistent with a larger average QD size. Signal broadening is also more significant, which aligns with increased heterogeneity due to higher Ga incorporation. With temperature increase, the bleach maximum shows a slight shift toward the red, but less than in the pristine case. The reduction in bleach intensity is more dramatic than in the 2.5% sample, reflecting more extensive state-filling and carrier trapping as Ga levels become more dominant in the electronic structure.

Figure 26D shows the most heavily alloyed system, with 15% Ga content. The GSB maximum is now located near 600 nm and is the broadest among all samples, confirming substantial size variation and alloying inhomogeneity. The observed broadening of the signal is more pronounced, consistent with enhanced structural heterogeneity resulting from higher Ga content. The GSB intensity continuously decreases with temperature, due to the enhanced Coulomb blockade and carrier delocalization effects. The presence of heavily occupied impurity states suppresses photoinduced bleaching by blocking access to the CB edge.

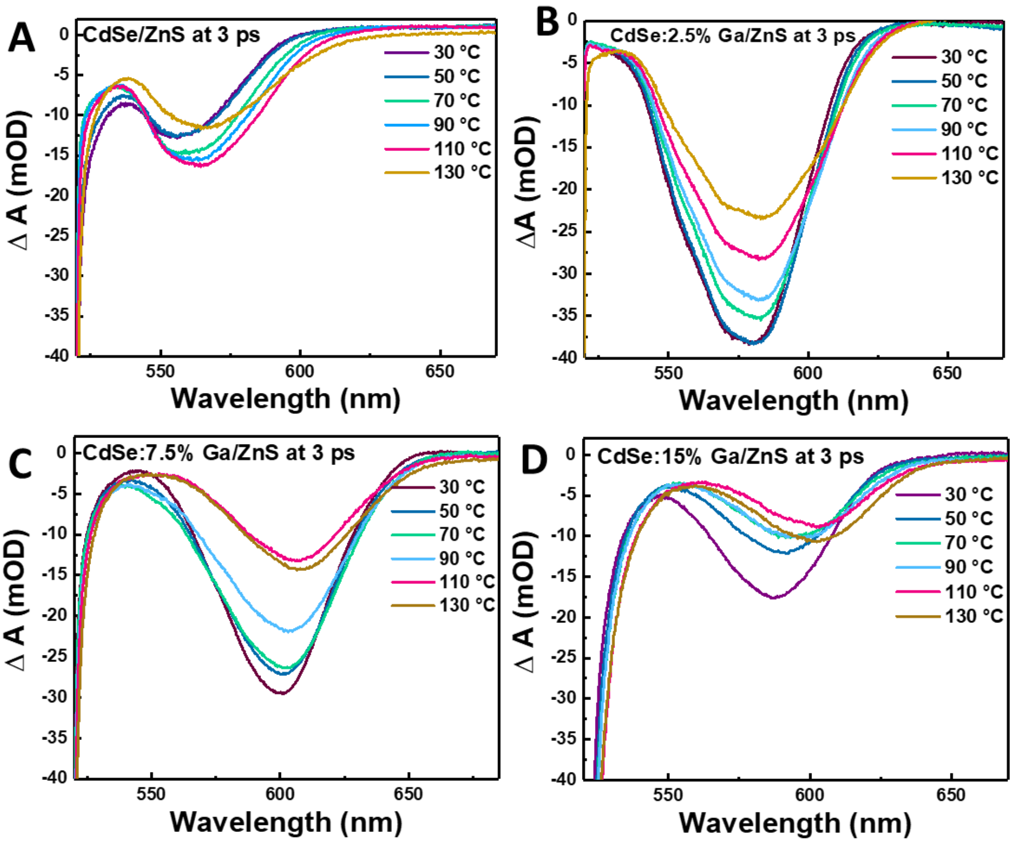

Figure 26. TA spectra at 3 ps delay to investigate the temperature dependence of GSB intensity in the 30–130 °C regime is shown. **A:** of the pristine samples **B:** of CdSe:2.5% Ga/ZnS QDs **C:** TA spectra of CdSe:7.5% Ga/ZnS QDs and **D:** of CdSe:15% Ga/ZnS QDs.

The previously discussed observations regarding the Ga-content and temperature on the key properties of the GSB (maximum absorbance and wavelength) are summarized in **Figure 27.** From the temperature-controlled TA spectra it can be determined that for every alloyed sample, the maximum of the GSB signal decreases by 30 to 40% when the system is heated from 30°C to 130°C (**Figure 27A**). The only exception is observed in the unalloyed system, where the GSB signal increases due to the sample heating. This suggests that elevated temperatures facilitate the promotion of electrons from the occupied Ga impurity levels to the CB of CdSe QDs. Electrons in the CB effectively hinder the excitation of electrons to the CB edge, thereby reducing the bleaching intensity of the samples. Conversely, pristine CdSe samples lacking Ga alloying levels exhibit the opposite behavior. In these samples, increasing temperature can promote the $1S_e$-$1P_e$ excited-state transition (0.2 eV).[119] This in turn further increases the population of the excited state, which results in an increase in the magnitude of the GSB signal. Apart from the maximum GSB intensity, the position of the GSB was also affected by the incorporation of Ga into the samples (**Figure 27B**). With increasing Ga content, a similar shift to a higher wavelength was observed as determined from the static UV-Vis spectra in **Figures 19 and 20**. Hence, we deduce that this can be predominantly attributed to the alterations in the QD size. At elevated temperatures, the GSB maximum shifts towards longer wavelengths. This shift aligns with the temperature-dependent excitability of semiconductors, where an increase in temperature leads to a reduction in the bandgap. Consequently, the decrease in the energy barrier between the Ga impurity level and the CB edge of CdSe facilitates electron transfer to the CdSe core.[117]

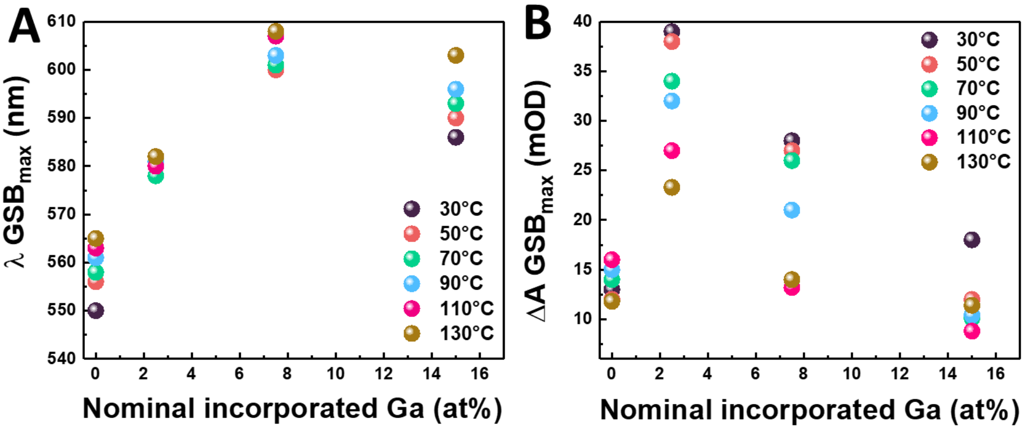

Figure 27. The effect of Ga incorporation on the bleaching signal for the different QD samples at different temperatures **A:** on the wavelength and **B:** on the maximum GSB intensity.

To better understand how temperature affects the charge carrier dynamics of systems, we recorded the TAS spectra in the 1–1650 ps time range. **Figure 28** shows the 2D TAS plots for pristine and 2.5% Ga alloyed CdSe/ZnS samples at 50 °C. The 2D plot facilitates the exploration of relationships between different parameters, providing valuable insights into the underlying mechanisms of a system or process. These plots suggest that after the evolution of the GSB signal, no additional features appear in the studied time range. At longer timescales, the steady but incomplete decay of the GSB signal is observed.

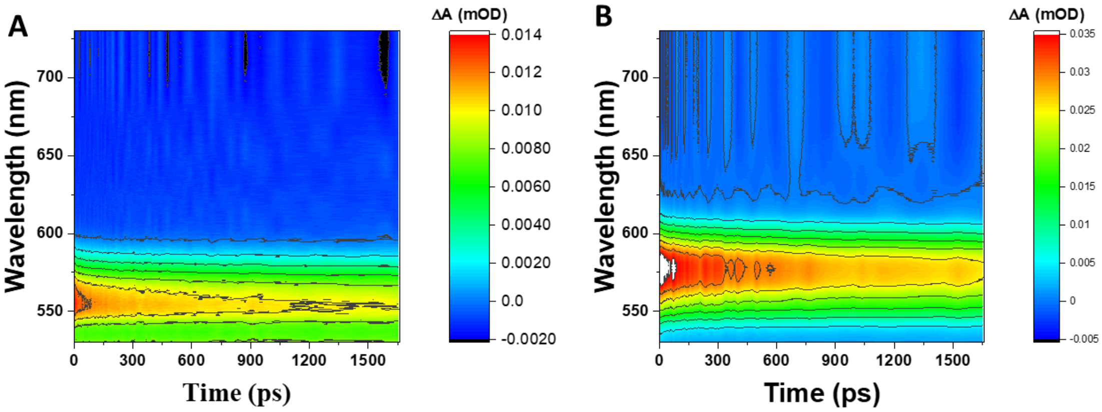

Figure 28. A: The 2D TAS plot of the bleach signal decay recorded at 50 °C in the 0–1600 ps time range for A: pristine, and **B:** 2.5% Ga alloyed CdSe/ZnS samples.

Figure 29A shows the extracted TAS spectra for the CdSe:2.5% Ga/ZnS sample at 30 °C. The GSB signal fully develops within 2 ps; by 1000 ps, the maximum GSB signal decreases by approximately 30%. **Figure 29B** shows the TAS spectra of the same sample at 130 °C. In this case a more rapid excited-state relaxation can be observed, where the GSB intensity decreases by 50% in the same timescale.

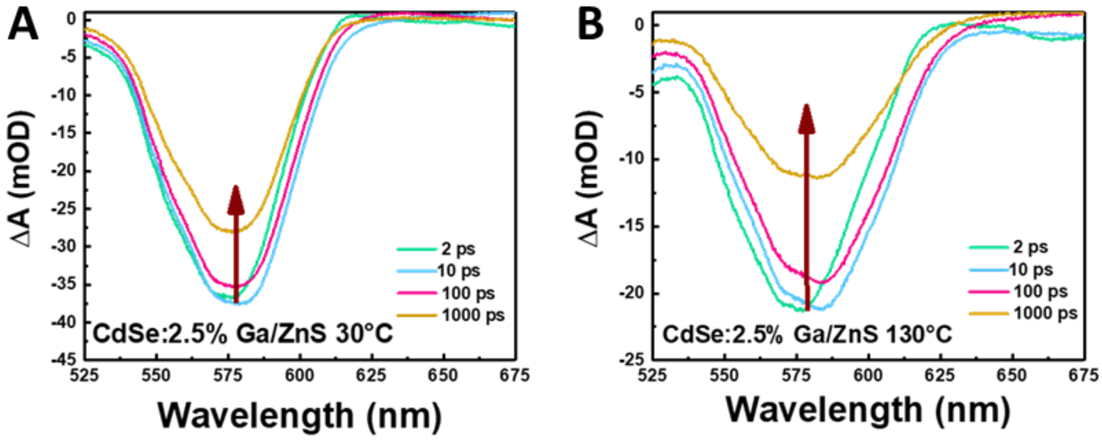

Figure 29. A: Time-dependent TAS spectra of the CdSe:2.5% Ga/ZnS QDs at **A:** 30 °C and **B:** at 130 °C, both cases with 515 nm pump.

4.1.3 Qualitative observations on the effect of temperature on the recombination kinetics

In the following section, we studied the effect of temperature on the recombination kinetics through the analysis of the kinetic curves obtained from the time-dependent TAS measurements. From the fitting of the kinetic curves, we determined the lifetimes and contributions of the different photophysical processes. In the pristine sample, the GSB signal decays relatively slowly and exhibits temperature dependence, as shown in **Figure 30A**. The decay follows a biexponential behavior where the fast component can be attributed to hot electron relaxation, and the slower component to shallow trap-mediated recombination. Upon introducing 2.5% Ga, shown in **Figure 30B**, the decay becomes faster and more sensitive to temperature. This acceleration is due to thermally activated electron transfer from Ga-induced impurity states to the CB and the emergence of trion-related recombination pathways, which reduce the bleach signal more rapidly at elevated temperatures. **Figure 30C** shows the situation for the 7.5% alloyed sample: the decay profile becomes more complex and noisier, yet it shows an overall faster recovery. The process described by the slower component becomes longer-lived, indicating enhanced trion stability. Temperature-dependence is more striking in the amplitudes of the decay components than in their characteristic times, reflecting a shift in the dominant relaxation pathways. **Figure 30D** shows the 15% Ga sample: the signal decay approaches a monoexponential form dominated by a slow component extending beyond the observed time window, suggesting a reduced role of intermediate trap states and a simplified carrier relaxation scheme.

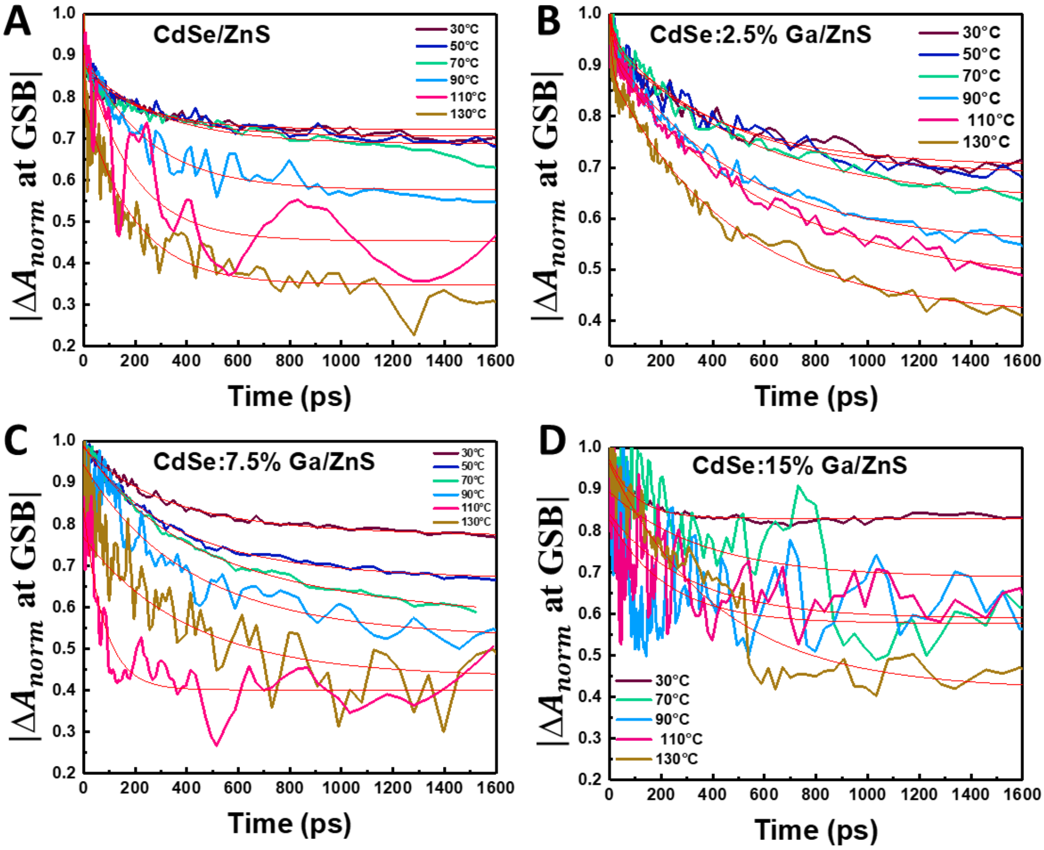

Figure 30. Temperature-dependent normalized decay traces at the GSB maximum for CdSe:Ga/ZnS QDs with increasing Ga content. **A:** pristine CdSe/ZnS; **B:** 2.5% Ga alloyed CdSe/ZnS; **C:** 7.5% Ga alloyed CdSe/ZnS; **D:** 15% Ga alloyed CdSe/ZnS. The decay curves are normalized at time zero and recorded at temperatures between 30 °C and 130 °C.

4.1.4 Quantitative results of the kinetic analysis

To elucidate how temperature affects carrier dynamics within these systems, we fitted the curves with a biexponential function (except for the highest Ga-content sample). The obtained fitting parameters are summarized in **Tables A2 to A5**. When comparing the lifetimes of pristine and 2.5% Ga-alloyed CdSe/ZnS QDs, we can observe the differences in the relaxation of charge carriers. **Figure 31A, B** shows the extracted t_1 and t_2 lifetimes of pristine CdSe/ZnS and CdSe:2.5% Ga/ZnS samples at different temperatures. In the pristine sample, the decay occurs on two distinct, well-resolved timescales: a fast one (t_1) of approximately 4.7 ps, corresponding to hot-electron relaxation, and a slower one (t_2) of 257 ps, related to recombination through shallow trap states. These lifetimes remain relatively constant with temperature, indicating that the relaxation processes in the pristine QDs are stable. In the 2.5% Ga-alloyed sample, both decay times become significantly longer: t_1 increases to 15.3 ps, and t_2 to 530 ps. This shows that Ga-alloying introduces new processes that slow down the relaxation time of excited charge carriers. The longer t_1 suggests that it takes more time for electrons to cool down to the band edges after excitation, possibly because of the Pauli spin blockade effect. The increase in t_2 is attributed to the formation of trions (charged excitons), which recombine more slowly and are formed because of the Ga-related impurity states. While the actual lifetime values do not change significantly with temperature (for a given sample), the relative weight of the different decay processes does. This is true especially for the alloyed samples, where higher temperatures shift more carriers into slower, trion-related relaxation paths. In the 7.5% Ga-alloyed CdSe/ZnS QDs, shown in **Figure 31C**, the determined decay times become even longer than in the 2.5% sample. The t_1 component increases further to 16.9 ps, and t_2 to 700 ps. This strong extension of both lifetimes suggests that trion recombination and long-lived charge-separated states are even more dominant at this alloying level. The gallium content introduces more impurity states that trap electrons, which slows down both the initial relaxation and the final recombination. These lifetimes also remain fairly constant across temperatures, similar to those in the lower-alloyed samples. The relative contribution of the slower component becomes more significant at higher temperatures, indicating that thermal energy facilitates the transition of more carriers into these longer-lived pathways. At 15% Ga content, shown in **Figure 31D**, the behavior changes noticeably. Instead of two distinct lifetimes, the decay can be described by a single slow process. The fitted lifetime becomes 1124 ps, which is the longest among all samples. This means that the fast relaxation channels are almost entirely suppressed, due to strong Coulomb blockade effects that prevent carriers from quickly recombining. These QDs store charge carriers for longer, and this dominant, slow decay remains relatively unchanged with temperature.

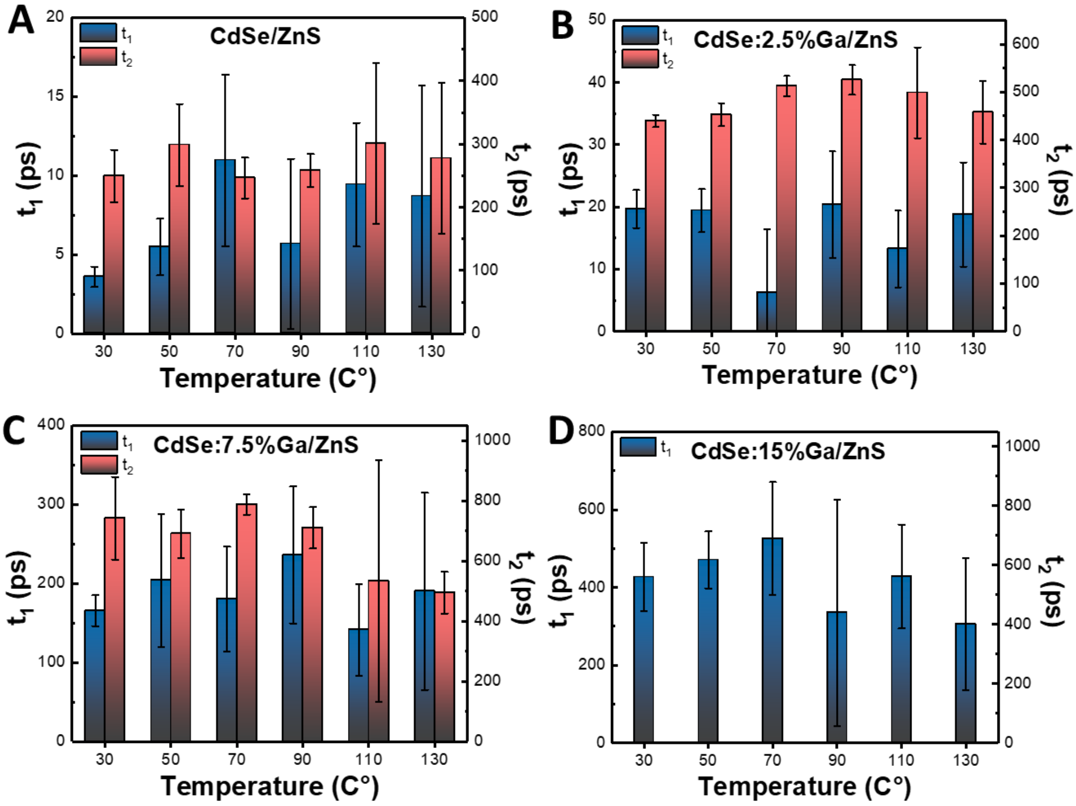

Figure 31. The t_1 and t_2 lifetimes at different temperatures **A:** of pristine CdSe/ZnS **B:** of CdSe:2.5% Ga/ZnS, **C:** of CdSe:7.5% Ga/ZnS and **D:** of CdSe:15% Ga/ZnS QDs.

Although the lifetimes themselves stay constant, the relative importance of each channel changes, as hot electrons cool faster and traps become more populated or thermally depopulated. **Figure 32A** shows the contribution of the different decay processes to the GSB recovery in pristine CdSe/ZnS QDs at various temperatures. We extracted the parameters A_1, A_2, and y_0 from bi- or monoexponential fits of the TA decay curves. Here, A_1 corresponds to the fast component related to hot electron relaxation (green), A_2 shows the slower trapping or trion-related decay (pink), while y_0 represents long-lived charge carriers that do not contribute to the recovery of the bleach signal (brown). These charge carriers will participate in longer processes such as radiative recombination. At 30 °C, the fast and slow components have similar contributions. As the temperature increases, recombination through shallow trap states becomes more prominent, as more charge carriers relax through the slower, trap-related pathway. This is accompanied by a decrease in the fraction of charge carriers that remain in their separated state, due to thermally assisted escape from traps without immediate recombination. Interestingly, hot carrier relaxation processes are relatively unaffected by temperature and are the least prominent route in the excited-state relaxation process. The data confirm that even in pristine QDs, the decay pathway distribution is influenced by temperature. **Figure 32B** shows the contribution of decay components in the 2.5% Ga-alloyed CdSe/ZnS QDs. A similar situation arises as in the case of the pristine samples. The contribution of trap-assisted or trion-related (A_2) pathways increases with temperature at the expense of processes that fall outside the measurement time window (radiative recombination). In this case, y_0 decreases with increasing temperature, similar to previous observations, while A_1 remains nearly constant and does not become the dominant relaxation pathway. **Figure 32C** presents the contribution of the different processes for the 7.5% Ga QDs. The trap-assisted recombination and trion decay components remain dominant, similar to the 2.5% sample. In this case, y_0 decreases significantly with increasing temperature, indicating more complete bleach recovery. This trend is accompanied by a marked increase in the contribution of A_2, the slower trapping or trion-related process, while A_1, the fast hot electron relaxation component, remains nearly constant. **Figure 32D** shows the decay components in the 15% Ga QDs, where monoexponential behavior is observed, and relaxation is governed by a single, slow process. In this case, y_0 decreases slightly with increasing temperature, indicating a reduction in the population of long-lived, nonrecombining carriers. Meanwhile, A_1 shows a slight increase, suggesting an enhancement of hot electron relaxation at elevated temperatures. The long-lived component is so dominant that no additional decay channels can be observed. This confirms that at high Ga content, the relaxation dynamics are governed by a Coulomb blockade and the impurity states.

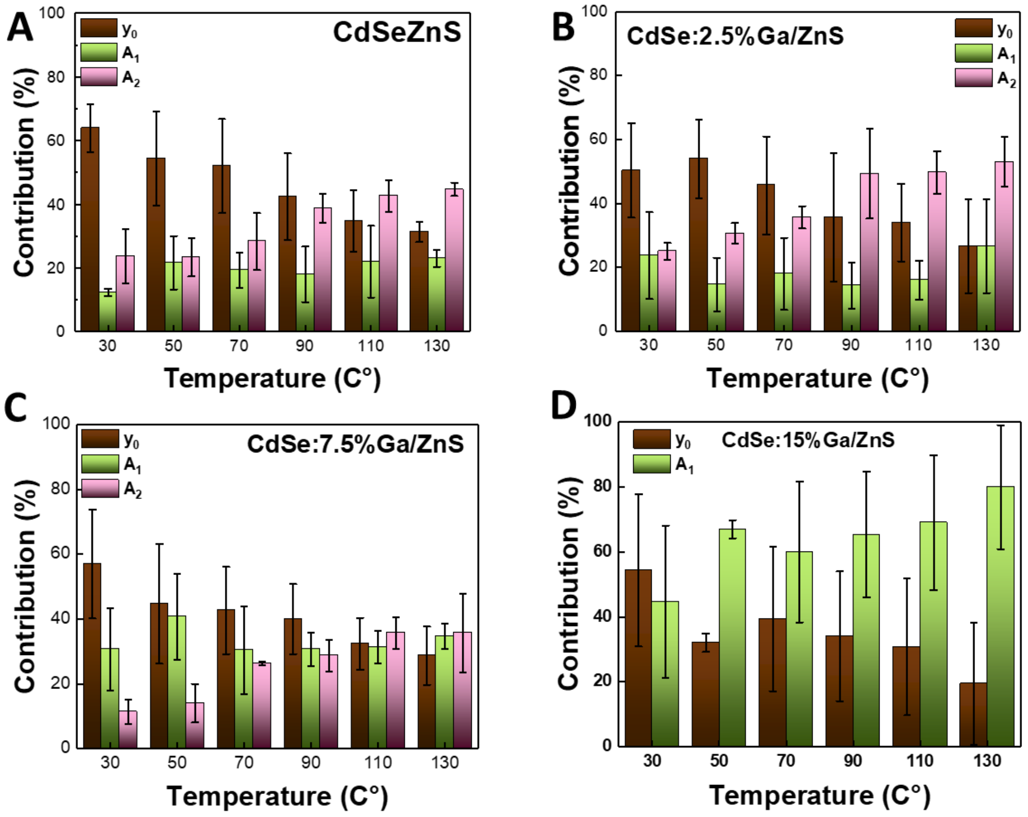

Figure 32. The temperature dependence of the contribution of distinct decay components in **A:** the pristine QD sample, **B:** 2.5% Ga-alloyed CdSe/ZnS QDs. **C:** 7.5% Ga-alloyed CdSe/ZnS QDs, and **D:** 15% Ga-alloyed CdSe/ZnS QDs. The green bars represent hot-carrier relaxation, the pink bars correspond to recombination through shallow trap states, while the brown bars show the fraction of charge carriers that remain separated throughout the measurement window. Error bars represent the standard deviation of three independent measurements.

It is important to confirm that the temperature increase does not introduce additional trap states in the QD samples. We examined the decay traces of CdSe:7.5% Ga/ZnS QDs before and after heating the sample to 130 °C, as shown in **Figure 33.** The overlap of the two traces through the entire time range indicates that the carrier relaxation dynamics remained unchanged after thermal cycling. This result confirms that no irreversible damage occurred during the high-temperature measurements, and the electronic properties (e.g., trap states, doping level, and recombination channels) were unaffected. The minimal difference between the curves also suggests that the Ga-induced impurity states and trion-related processes are thermally robust.

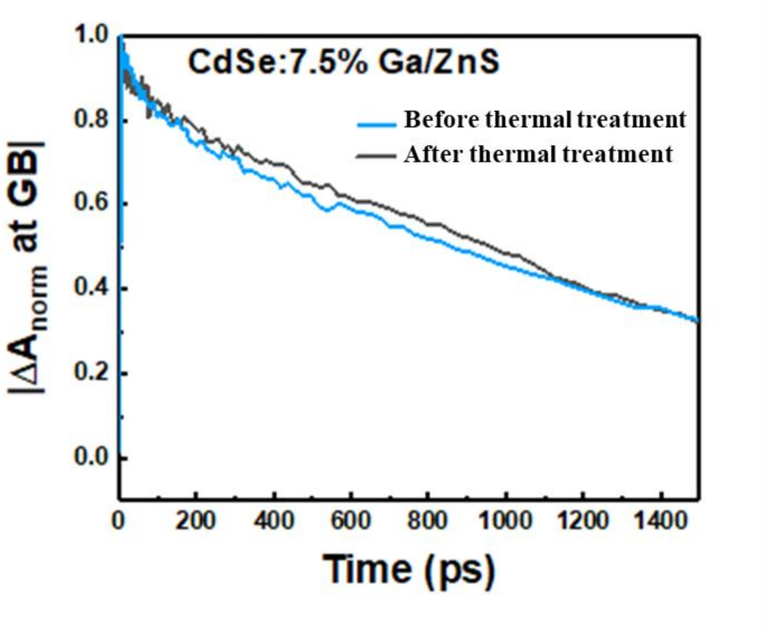

Figure 33. The decay trace of CdSe:7.5% Ga/ZnS before and after thermal treatment, performed between 30 °C and 130 °C. At each temperature step, the sample was held for at least 20 minutes to allow thermal stabilization.

Figure 34 shows the temperature-dependent contribution of long-lived charge carriers y_0 for the four different QD samples. Each bar represents a single sample at a specific temperature. These charge carriers do not recombine quickly and will participate in radiative recombination on longer timescales. At 30 °C, all four samples show relatively high y_0 values, meaning that a large portion of the carriers stay separated after excitation. As the temperature increases, the y_0 values decrease in every sample. This trend suggests that higher temperatures help the carriers to recombine faster or escape from their localized states. The additional thermal energy can activate alternative relaxation pathways that were less available at lower temperatures. The pristine QD sample shows the highest y_0 at almost all temperatures, while the 15% Ga sample shows the lowest contribution from long-lived separated carriers. This means that alloying reduces the fraction of carriers that can remain separated, which is the direct consequence of the Ga-induced impurity states that act as additional recombination or trapping channels for charge carriers. This behavior is consistent across all doping levels and supports the idea that both temperature and gallium content control the duration for which the carriers remain active in the system.

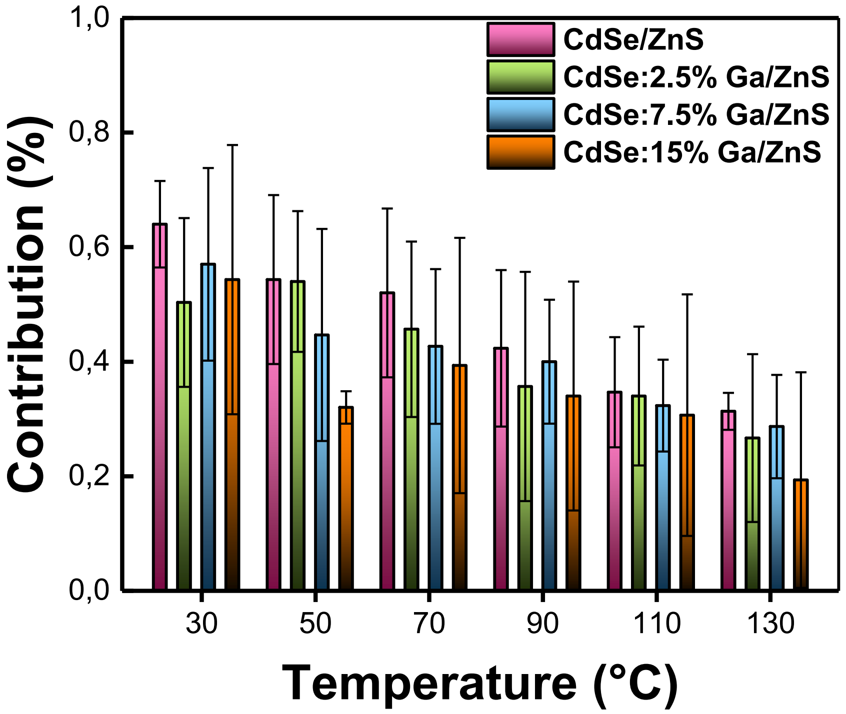

Figure 34. The temperature-dependence of the contribution of long-lived charge carriers (y_0) to the overall charge carrier dynamics of all investigated samples.

4.1.5 Conclusion of the temperature-dependent photophysics in Ga-alloyed CdSe/ZnS QDs

To summarize, we investigated the temperature-dependent TAS characteristics of CdSe/ZnS and Ga-alloyed core-shell QD systems by varying the amount of Ga alloying. We measured the optoelectronic characteristics using steady-state UV-Vis and PL spectroscopy methods. Time-resolved PL measurements revealed a fast emission decay in the unalloyed QDs compared to the alloyed samples. We investigated the impact of temperature and Ga content on carrier dynamics by performing temperature-dependent TAS measurements. The excited state recovered faster in the CdSe/ZnS samples than in the ones with gallium. Based on our experimental results, we can conclude that Ga-alloying facilitates the formation of trions in the samples, thereby prolonging the hot-electron lifetime. While temperature had minimal effects on the determined time constants, it influenced the fraction of charge carriers in distinct recombination channels. In conclusion, our results demonstrate that temperature-dependent TAS measurements provide a powerful tool for observing carrier relaxation processes via various relaxation pathways. The proposed mechanism is illustrated in **Scheme 1.**

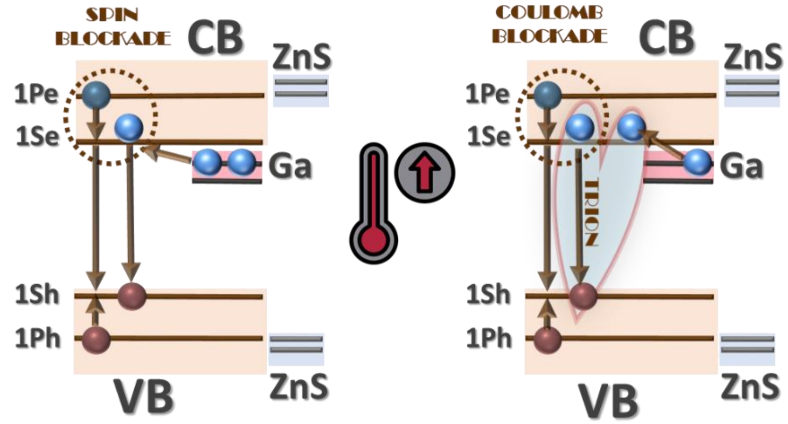

Scheme 1. Schematic illustration of Ga-alloyed CdSe/ZnS core-shell QDs before and after heating the sample.

4.2 Exciton dynamics in MoS_2/pentacene and WSe_2/pentacene heterojunctions

4.2.1 Evaluation of hole transfer in MoS_2/pentacene heterojunctions

We examined how the presence of pentacene films influences the exciton dynamics in MoS_2 monolayers. To elucidate the differences between the systems, apart from the heterostructures, the constituent materials were also studied. The samples were prepared and provided by P. Markeev et al.[124] We developed a TRS system (described in the Experimental section) to follow the carrier dynamics in the heterostructures after photoexcitation.

The time-dependent 2D TR plot of a 20 nm pentacene thin film deposited on gold and measured after photoexcitation at 515 nm are shown in **Figure 35A.** We observe a strong GSB signal at 688 nm, corresponding to the singlet exciton in pentacene. Two smaller bleach features also appear at 635 nm and 597 nm. These peaks result from Davydov splitting (splitting of exciton energy levels due to interactions between non-identical positions of molecules in the crystal), caused by the two nonequivalent pentacene molecules in the crystal unit cell. **Figure 35B** shows the kinetic trace extracted from the main bleach region of the pentacene films (675–695 nm). The signal is long-lived and stable for over 1 ns, indicating that the excited state remains populated.

Although pentacene is known for very fast singlet fission (sub-150 fs), this ultrafast process was not captured in this measurement due to the limited temporal resolution.

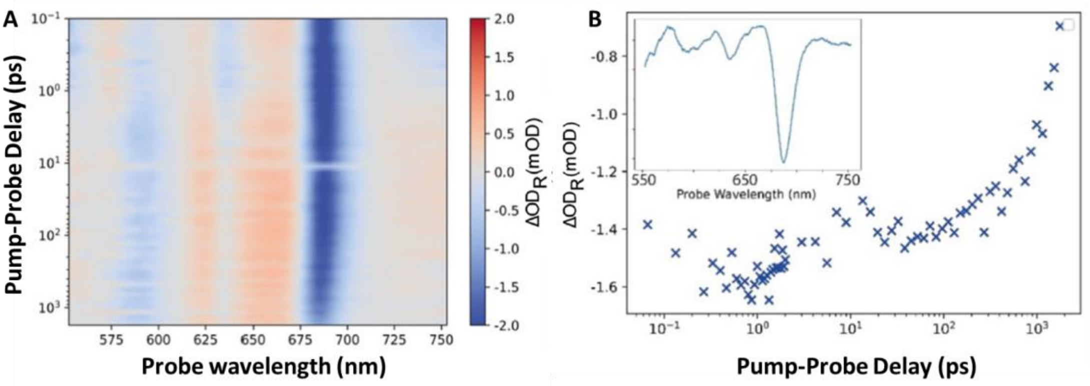

Figure 35. A: 2D TR spectra of a 20 nm pentacene film on a gold substrate and **B:** the kinetic trace of the main feature at 675−695 nm from the averaged spectra in A. The small inset represents the spectrum at 0.53 ps delay time.

To understand how pentacene affects the optical response of MoS_2, we compared the TR spectra of bare and pentacene-covered MoS_2 monolayers. **Figure 36A** presents the 2D TR plot of bare monolayer MoS_2 on a gold substrate. Two distinct bleach peaks appear at 615 nm and 662 nm, which correspond to the B and A excitons of MoS_2, respectively. These peaks confirm the strong excitonic nature of the monolayer sample. **Figure 36B** shows the same MoS_2 crystal, now covered with a 20 nm pentacene layer. Here, the bleach features broaden and partially overlap. We still observe the MoS_2 A exciton near 670 nm, but the nearby pentacene bleach at 688 nm also contributes.

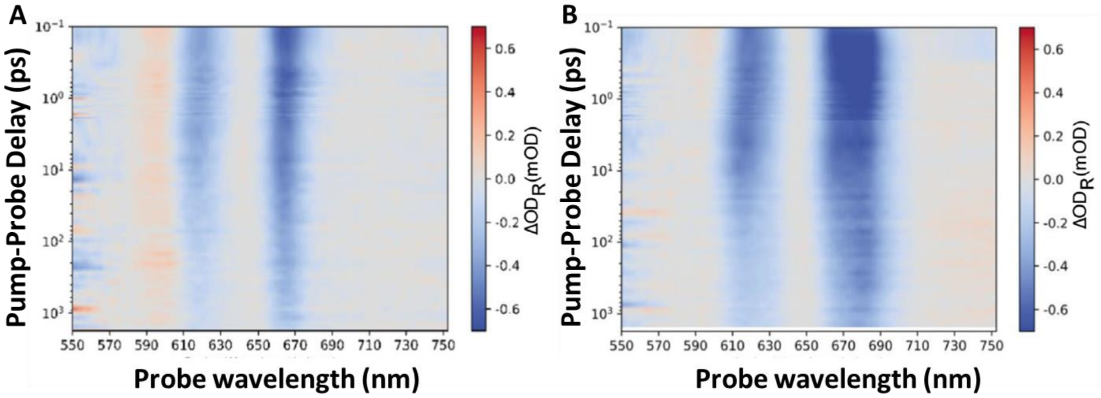

Figure 36. A: 2D TR spectra of MoS_2 monolayer crystals transferred to a gold substrate and **B:** similar MoS_2 monolayer crystals on gold covered by a pentacene thin film.

In **Figure 37A,** we directly compare three samples: pure MoS_2 (blue), pure pentacene (green), and the MoS_2/pentacene heterostructure (yellow). The transient spectra were recorded 0.53 ps after excitation. The spectra clearly show that the heterostructure includes both MoS_2 and pentacene signals. The strongest bleach in pentacene was recorded at 688 nm, and it overlaps with the A exciton bleach of MoS_2. We also observed a slight redshift of the A exciton bleach compared to the bare MoS_2. This shift can result from the interface interactions or screening effects caused by the organic overlayer. The combined spectrum appears broader than either of the individual spectra, which supports the idea of state hybridization or band alignment effects at the interface. These observations further confirm that the pentacene layer does not simply lie on top of MoS_2 but actively modifies its electronic response on ultrafast timescales. **Figure 37B** shows the decay trace of A exciton (at 662 nm) in MoS_2. When comparing its decay in pristine MoS_2 and the MoS_2/pentacene heterostructure, we observe a slight difference in the decay dynamics; the parameters are shown in **Table 4.**

Table 4. Fitted decay parameters for A exciton dynamics in MoS_2 and MoS_2/pentacene samples

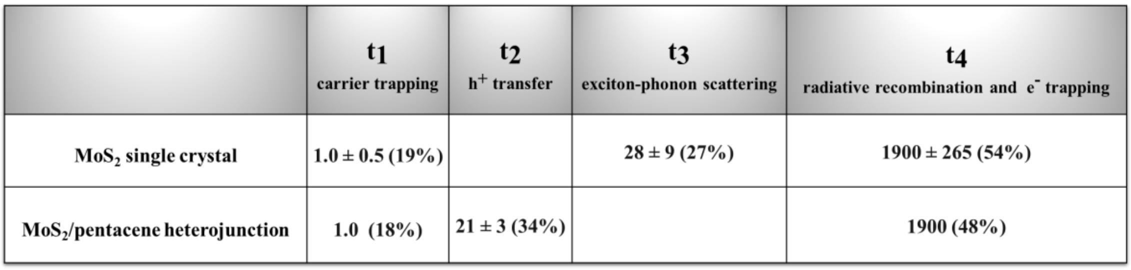

	t_1 carrier trapping	t_2 h^+ transfer	t_3 exciton-phonon scattering	t_4 radiative recombination and e^- trapping
MoS_2 single crystal	**1.0 ± 0.5 (19%)**		**28 ± 9 (27%)**	**1900 ± 265 (54%)**
MoS_2/pentacene heterojunction	**1.0 (18%)**	**21 ± 3 (34%)**		**1900 (48%)**

In the pristine sample, the decay can be fitted with three components: $t_1 = 1 \pm 0.5$ ps, $t_2 = 28 \pm 9$ ps and $t_3 = 1900 \pm 265$ ps. Lifetime t_1 belongs to the carrier trapping, the intermediate exciton relaxation belongs to exciton–phonon scattering and a long-lived component attributed to radiative recombination and electron trapping. In the heterostructure, the decay includes ultrafast defect-assisted trapping t_1=1 ps, an intermediate component t_2=21 ± 3 ps attributed to hole transfer from pentacene to MoS_2, and a long-lived decay t_3=1900 ps associated with radiative recombination and electron trapping, similar to the pristine case. The table also reveals that a triexponential fit was applied in both cases. This change shows that the pentacene layer introduces a fast decay channel, which shortens the exciton's lifetime. We associate this fast component with the hole transfer from pentacene to MoS_2. **Figure 37C** shows the normalized decay traces of the B exciton in MoS_2 monolayers, both with and without the pentacene overlayer. The measurements were recorded at 615 nm, corresponding to the B exciton transition in MoS_2. The two decay curves of pure MoS_2 and the MoS_2/pentacene heterostructure overlap. This result shows that the presence of pentacene does not significantly change the decay dynamics of the B exciton. Consequently, only the A exciton interacts with the pentacene layer, while the B exciton remains mostly unaffected.

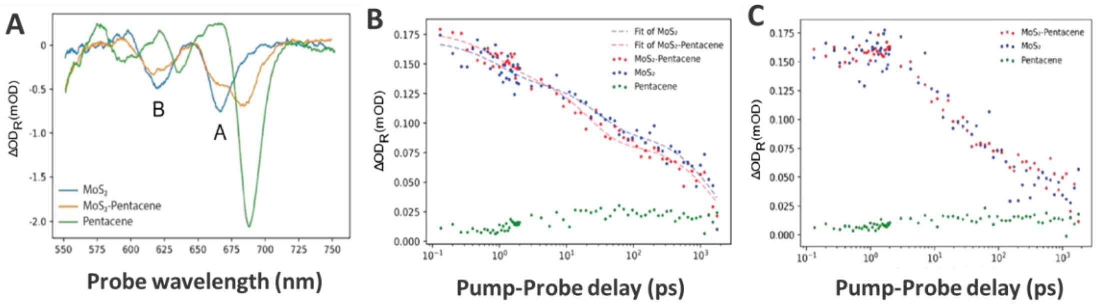

Figure 37. A: TR spectra of a MoS_2 monolayer (blue), a MoS_2-pentacene junction (yellow), and a pentacene thin film (green). All samples were deposited on Au substrates, and we probed at 0.53 ps. Normalized decay traces in a MoS_2 monolayer and in a MoS_2-pentacene junction for the **B:** A exciton probed at 662 nm, and **C:** B exciton probed at 615 nm.

4.2.2 Evaluation of hole transfer in WSe_2/pentacene heterojunctions

The TR spectra for three samples: a WSe_2 monolayer (blue), a WSe_2/pentacene heterojunction (yellow), and a pure pentacene thin film (green) are shown in **Figure 38A**. Similarly to MoS_2, all samples were deposited on gold substrates and measured at 0.53 ps after excitation. The A exciton peak was outside our detection window and was therefore not analyzed in this study. In the WSe_2/pentacene sample, the B exciton peak of WSe_2 shifted from 621 nm to 615 nm. This small blueshift results from screening effects caused by the pentacene overlayer, which slightly reduces the exciton's binding energy. **Figure 38B** compares the kinetic decay traces of B excitons in the uncovered WSe_2 monolayer and the WSe_2/pentacene heterostructure, fitted lifetimes are shown in **Table 5.**

Table 5. Fitted decay parameters for B exciton dynamics in WSe_2 and WSe_2/pentacene samples

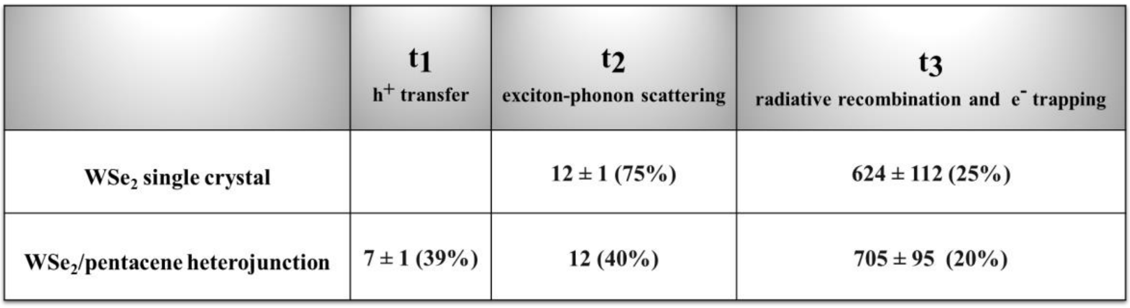

	t_1 h^+ transfer	t_2 exciton-phonon scattering	t_3 radiative recombination and e^- trapping
WSe_2 single crystal		12 ± 1 (75%)	624 ± 112 (25%)
WSe_2/pentacene heterojunction	7 ± 1 (39%)	12 (40%)	705 ± 95 (20%)

For the bare WSe_2, a biexponential decay fits the data well, with time constants $t_2 = 12 \pm 1$ ps and $t_3 = 624 \pm 112$ ps. These processes can be attributed to exciton–phonon scattering and radiative recombination, respectively. In the heterostructure, an extra fast component (t_1=7±1 ps) appears in the fit, because of hole transfer from pentacene to WSe_2. This additional decay path confirms that charge transfer occurs at the interface and influences the exciton lifetime. The intermediate decay component t_2 (12 ps, 40%) is attributed to exciton–phonon scattering, while the long-lived component t_3 (705 ± 95 ps, 20%) corresponds to radiative recombination and electron trapping. These results demonstrate that pentacene not only alters the spectral position of the B exciton but also introduces new ultrafast decay channels, most likely related to interlayer charge dynamics within the heterostructure.

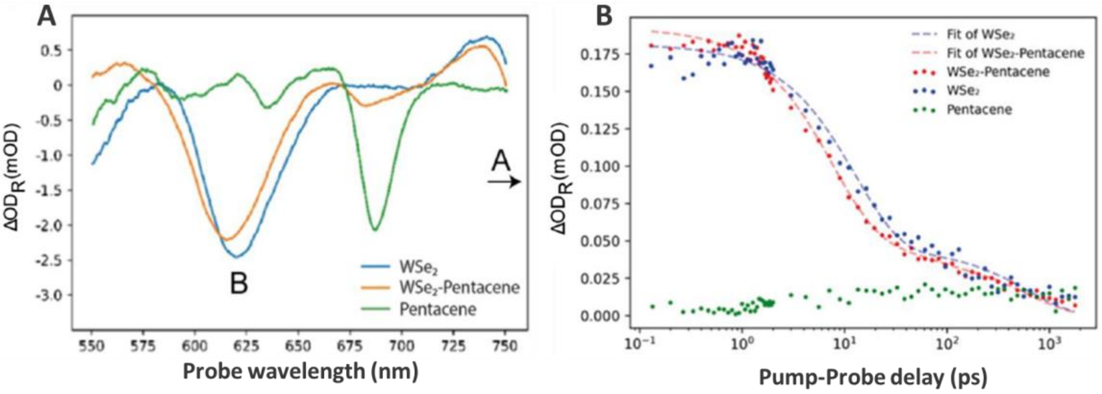

Figure 38. A: TR spectra recorded at 0.53 ps and **B:** decay traces of B excitons in WSe_2, pentacene, and their heterojunction.

4.2.3 Conclusion of hole transfer kinetics in TMDC/pentacene heterojunctions

To summarize, we compared the excited-state decay in monolayer MoS_2 and WSe_2 crystals, both bare and covered with a 20 nm pentacene film. We found that in both heterostructures the TR spectra exhibit mixed features, with observed spectral shifts indicating electronic coupling between the inorganic and organic materials. In the case of MoS_2, the A exciton decay becomes faster when pentacene is deposited. The fast decay component (21 ± 3 ps) appears, which signals hole transfer from pentacene to MoS_2. The B exciton decay remains unchanged, suggesting that only the A exciton is affected by the interface. In stark contrast for WSe_2, we observed the electronic coupling (t_1 = 7 ps) of pentacene to the B exciton (higher energy). A small spectral shift appears in the exciton bleach, and a fast decay component is observed only in the heterostructure. This also points to interlayer charge transfer.

4.3 THz generation and preparation for visible pump and THz probe TAS

4.3.1 Principles of THz generation via asymmetric two-color laser plasma

EO sampling is a widely used technique for detecting THz radiation, offering excellent time resolution due to its sub-picosecond gating, which is particularly effective for resolving ultrafast dynamics in systems probed by THz fields. The method works well with standard femtosecond lasers. Using a nonlinear crystal (e.g., ZnTe), the THz electric field can be directly measured in the time domain. This technique requires carefully aligned crystals, broadband phase matching, and often cryogenic or vibration-stable environments. The properties of the detection crystal limit the spectral range. Due to these limitations, all-air THz generation and detection schemes have garnered increasing attention. This setup configuration is based on plasma-generation processes in air, which removes the need for solid-state crystals. This approach combines the second-harmonic field of a femtosecond laser with its fundamental beam. This can accelerate charges within the air plasma produced by the focused laser pulses. The result is the emission of an intense THz pulse characterized by a broad frequency spectrum. [125] Utilizing this technique, a THz source operating at a 1 kHz frequency was demonstrated, delivering pulse energies exceeding 1 μJ, with an electric field intensity reaching approximately

1 MV/cm. The reported spectral bandwidth spans from 0.01 to 60 THz, showcasing the versatility and capabilities of this method.[126]

Before integrating a THz generation/detection arm into the TAS setup at ELI ALPS, we performed the initial experiment at the TeWaTi femtosecond laboratory at the University of Szeged with a multipass CPA Ti:Sapphire laser system. The experimental arrangement for generating THz pulses from an asymmetric air plasma is depicted in **Figure 39.** The used laser system can produce 20 fs laser pulses with a pulse energy of 1.2 mJ at a repetition rate of 200 Hz and a central wavelength of 800 nm. The dispersion of the femtosecond light pulses is controlled with an acousto-optic programmable dispersive filter, known as a Fastlite Dazzler, which can shape the spectral phase (e.g., GD and GDD) and the amplitude of ultrashort laser pulses.

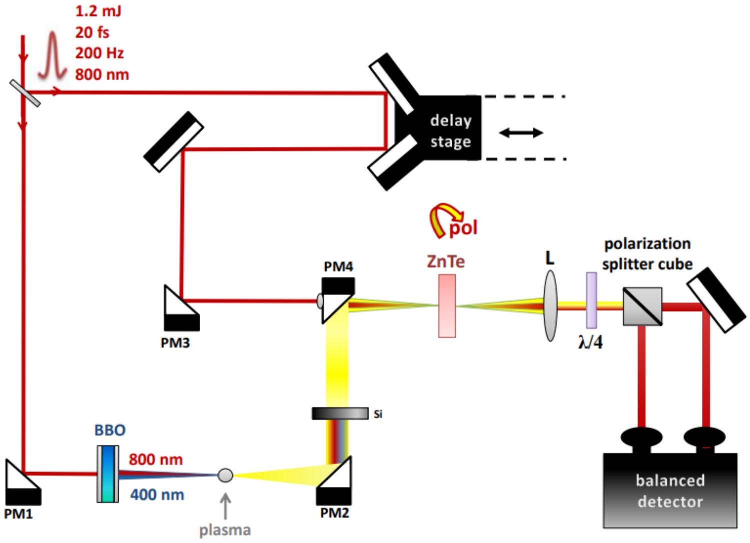

Figure 39. The experimental setup for two-color laser plasma generated THz radiation

The incoming beam is split into two using a beam splitter. Approximately 90% of the beam's intensity is directed toward THz generation. This beam travels in air through an off-axis parabolic mirror (PM1) with a focal length of 6 inches. A BBO crystal is positioned between the parabolic mirror and the focal point for SHG via type I phase-matching. The combination of the two waves produces an asymmetric waveform when the phase difference between them is correct (π/2). When these two beams are focused simultaneously, an asymmetric air plasma is generated, in which accelerated electrons produce radiation in the THz regime. The THz beam propagates conically and is collimated by a suitably sized (1-inch diameter and 4-inch focal length) gold-coated, off-axis parabolic mirror (PM2). A 0.5 mm thick silicon wafer is placed after THz generation to eliminate the Vis and NIR components from the THz beam. In our experiments, we employed the EO sampling to detect both the phase and amplitude of the electric field of the coherent THz light. The THz and reference beams spatially and temporally overlapped on a 1 mm thick 110-cut wedged ZnTe EO crystal. The THz beam was focused by a holey off-axis parabolic mirror (PM4) with a focal length of 2 inches, while the probe beam was focused by another off-axis parabolic mirror (PM3) with a focal length of 6 inches, through the mentioned hole. The THz field induced polarization rotation in the reference beam, and the changes in polarization were recorded through balanced detection. Before the measurement, and in the absence of the THz field, the signals in the two photodiodes were balanced using a polarization beamsplitting cube and a properly aligned quarter-wave plate. Following prealignment, the programmable delay stage scanned the weak probe pulses in the temporal domain during the THz pulse generation event. A lock-in amplifier (Ametek 5210) with a 100 Hz reference signal and a 300 ms integration time was used to acquire the signal for a given position of the delay stage.

4.3.2 The impact of phase matching and dispersion on THz generation

During the generation and measurement of THz radiation, several experimental factors can significantly change the shape, polarity, or intensity of the THz signal. One key source of distortion is the relative phase mismatch between the fundamental (ω) and second-harmonic (2ω) pulses, which can change the polarity of the emitted THz waveform. Another important factor is the chirp (GDD), which can stretch the pulse in time and affect the dynamics of the ionization current that drives THz emission. Temporal or spatial misalignment between the pump and probe beams can lead to a loss of signal or incorrect timing. Dispersion and absorption in detection crystals (e.g., ZnTe), as well as environmental noise and mechanical instability, can degrade the measured signal. In the following section, I focus on how phase delay and chirp influence the THz waveform in air-plasma-based generation systems.

Figure 40A shows the measured THz time-domain signals for two different BBO crystal positions: 7 mm (blue) and 19 mm (green). At 7 mm, the THz signal exhibits a clear positive peak of approximately 4.5 (a.u.) electric field, while at 19 mm, the signal flips, producing a negative peak of approximately –2.5 (a.u.) electric field. This demonstrates that changing the position of the BBO crystal and thus the relative phase between the fundamental (ω) and second-harmonic (2ω) pulses, inversion of the THz field polarity, and alteration to the shape and intensity of the THz waveform can be achieved. In some positions, the waveform is mostly positive, while in others it is negative or even symmetric. **Figure 40B** summarizes this effect by plotting the peak value of the THz signal as a function of the BBO position. The blue points represent measured values, while the red curve is a sinusoidal regression. The electric field maximum oscillates between 5.2 (a.u.) and 2.7 (a.u.) over a full phase cycle. The fitted curve yields a phase sensitivity of 60 mrad/mm, which is in correlation with the theoretical calculations. This indicates that the BBO position directly influences the relative phase and can be used as a precise control parameter for tuning THz waveforms. The graph shows a smooth, oscillating trend, which means that the THz generation process is phase-sensitive. The periodic behavior originates from the phase shift that we expect from the changing optical path in the BBO. This shows that we can precisely control the polarity and strength of the THz pulse by adjusting the phase between the *ω* and *2ω* fields. These findings demonstrate that phase tuning is a simple and effective method for shaping THz radiation, without requiring any mechanical adjustments to the rest of the setup.

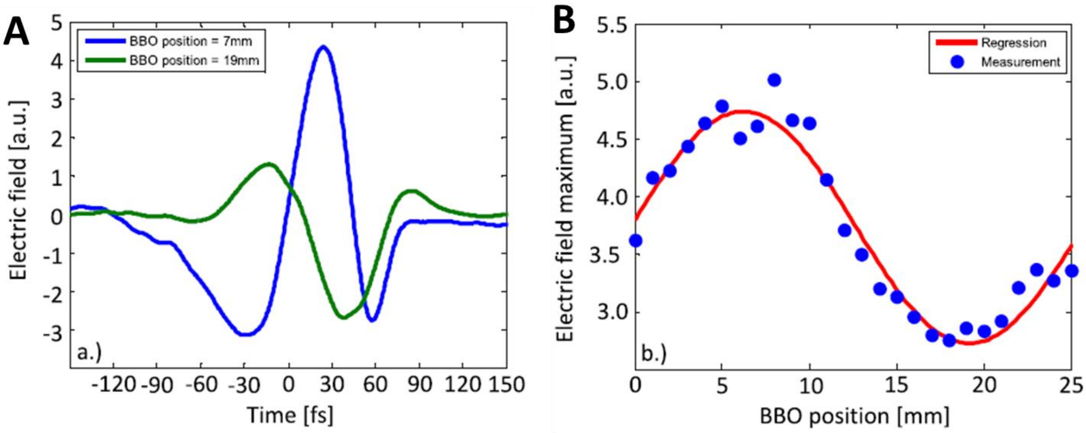

Figure 40. A: Time-domain THz waveforms measured at different BBO crystal positions, showing the effect of phase variation between the fundamental and second-harmonic pulses. The polarity and shape of the THz signal change systematically with the relative phase. **B:** Peak amplitude of the THz signal as a function of BBO position. The oscillating trend confirms the phase sensitivity of the THz generation process in air plasma using two-color excitation.

Figure 41 illustrates how both the chirp (GDD) and relative phase between the fundamental and second-harmonic pulses affect the amplitude of the generated THz signal. The experimental results with the THz peak amplitude as a function of the applied GDD and the relative phase (controlled via BBO position) are shown in **Figure 41A.** The plot reveals that the THz signal is the strongest when the GDD is close to zero and the relative phase is optimized. As the GDD increases in either direction, the THz amplitude decreases significantly. This is because chirped pulses stretch in time, which leads to a slower buildup of the ionization current that drives THz generation. The relative phase also modulates signal strength and polarity, in agreement with the earlier observations in **Figure 40.** The corresponding simulation results using the photocurrent model are shown in **Figure 41B.** The simulated map reproduces the key trends observed in the experiment, including a maximum amplitude near zero GDD and a strong phase dependence. The similarity between the experiments and simulations confirms that the main mechanisms of THz generation are described well by the model, despite its use of simplified assumptions. The main conclusion is that both temporal pulse shaping (via GDD) and phase control offer ways to tune the strength and direction of THz emission from air plasma. We can state that optimizing both parameters is essential for generating high-quality, stable THz pulses in all-air systems.

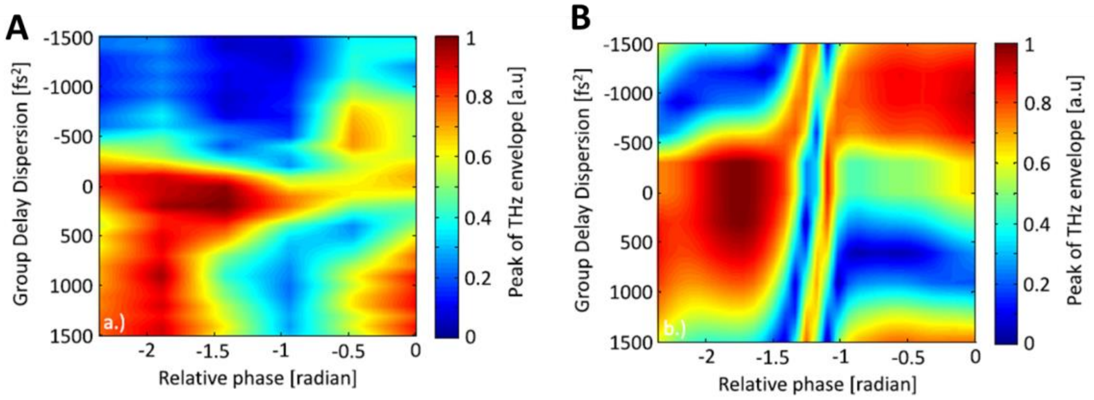

Figure 41. Dependence of the peak THz envelope on GDD and relative phase between the fundamental and second-harmonic pulses. **A**: Experimental measurements confirm the same trend, with maximum THz output near zero GDD and optimized relative phase. **B:** Numerical simulation using a photocurrent model shows that the THz amplitude decreases with increasing GDD and varies periodically with phase. Both maps demonstrate that temporal chirp and phase delay are effective control parameters for shaping THz waveforms in air plasma.

4.3.3 Implementation of THz probe in ELI ALPS

Figure 42 shows the interface of the LabVIEW software for the measurements, which is synchronized with the following electronic devices: mechanical chopper, delay stage, lock-in amplifier, and balance detector. On this surface, the scanning range, including initial and end positions, step size, resolution, and speed, can be adjusted. Every setting – external reference trigger input, manual phase, signal input, sensitivity, time constant, and filter – of the lock-in amplifier is adjustable from this interface. The measured THz signal from the balanced detector appears in red in the graph below.


External Reference Trigger Input (0: 50OHMS) 50OHMS 0
Manual Phase (0: Degree) 0
Signal Input (0: Voltage) Voltage 0
Sensitivity (0: 1 V (uA)) Auto Scale -1
Voltage Input Mode (0: A) A 0
Time Constant (10: 100 ms) 100 ms 10
Filter Slope (0: 6 dB/oct) 24 dB/oct 3
Sync Filter (0: OFF) OFF
VISA resource name USB0::0xB506:
Reference Source (0: Internal) External 1
External Reference Trigger (0: Sine Zero Crossing) Positive TTL 1
Auto Phase (0: Disabled) Enabled
Voltage Input Coupling (0: AC) AC 0
Voltage Input Shields (0: Float) Float 0
Voltage Input Range (0: 1V) 1V 0
Advanced Filter (0: OFF) OFF
Single Lock-in Parameter (0: X output) R output 2
THz signal 0,000422913
C:\THz measurements\2020.09.25\afterOOS 9
Initial THz pos (mm) 85,000
Current THz pos (mm) 91,160
THz resolution (mm) 0,010000
Final THz pos (mm) 92,000
Speed 1,25
Initial pump pos (mm) 3,0000
Current pump pos (mm) 3,0000
pump resolution (mm) 0,10000
Final pump pos (mm) 8,0000
error in (no error) status code 0 source

Figure 42. Front panel of the custom-built LabVIEW software used for THz time-domain measurements. Users can set the scanning range, step size, resolution, and speed, as well as configure all lock-in amplifier parameters. The red curve displays the measured THz signal as a function of the probe delay.

Figure 43 shows the measured THz time-domain signal using EO sampling with a ZnTe crystal. The graph shows the THz electric field (in arbitrary units) as a function of the delay stage position, which controls the temporal overlap between the visible probe and the THz pulse. The main peak around 90 mm corresponds to the point of maximum temporal overlap, where the THz-induced birefringence in the ZnTe crystal is strongest. The smaller peak near 87 mm may indicate a weak prepulse or a reflection. The signal outside these regions shows the noise floor. The prepulse can be caused by reflections at the front and back surfaces of the silicon plate, which is used because it is transparent to THz radiation but partially reflective or absorptive for visible light. This enables the separation of the probe and THz beams in a pump–probe setup. This plate can cause internal reflections and can generate multiple THz pulses arriving at different times, resulting in distinct features in the measured signal. Currently, the signal-to-noise ratio (S/N) of our setup is approximately 10:1, indicating that although the THz signal is detectable, noticeable background noise remains. Improving this ratio is important for obtaining more accurate and reliable data, especially for sensitive samples or low-intensity signals. S/N is strongly affected by several experimental parameters. Based on our observations, the most critical factor is the spatial and temporal overlap between the pump and probe beams at the EO crystal. Precise alignment in both space and time is crucial for maximizing the induced birefringence and, consequently, the measured THz signal. Even slight misalignments can result in a significant drop in signal amplitude or an increase in noise levels. Further improvements can be achieved by optimizing the beam focus, crystal thickness, and lock-in amplifier settings, as well as by minimizing stray reflections and vibrations in the optical path. These steps are essential for stabilizing the measurement and enhancing the sensitivity of the system**.**

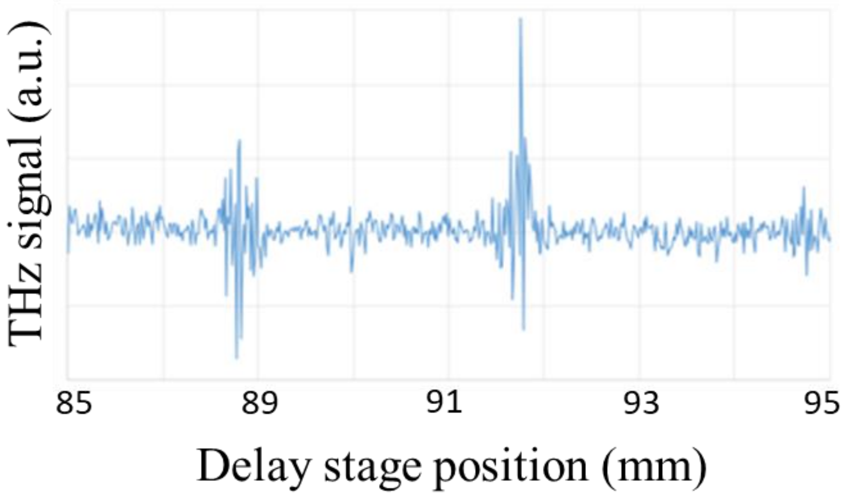

Figure 43. The measured THz time-domain signal using electrooptic sampling with a ZnTe crystal. The main peak is at 90 mm delay stage position, where the THz-induced birefringence in the ZnTe crystal is strongest. The smaller peak near 87 mm may indicate a weak prepulse or a reflection.

5. Conclusion

During my PhD work, I was primarily interested in understanding ultrafast processes in nanostructured materials, particularly those related to charge carrier dynamics in QDs and two-dimensional semiconductors. I focused on how external parameters (e.g., temperature, composition, and interface interactions) influence carrier relaxation, recombination, and transfer mechanisms on femto- to picosecond timescales. I was also motivated by the challenge of developing and adapting experimental setups for these studies, including the implementation of temperature control in TAS, extending TAS to thin-film geometries, and exploring the integration of THz probing, taking advantage of the capabilities of ELI ALPS' high-repetition-rate (100 kHz), carrier-envelope-phase (CEP) stable laser system. My goal was not only to study fundamental physical processes, but also to enable new types of measurements that could offer deeper insight into technologically relevant materials.

By using ELI ALPS' infrastructure, particularly the capabilities of the high-repetition-rate (HR) laser system, we aimed to establish a TAS setup that is not only scientifically powerful but also flexible and user-friendly. The system is suitable for a broad range of sample types, and allows for hassle-free changes of the pump and probe sources, and rapid reconfiguration to meet specific user demands—making it ideally suited for serving the international user community of the ELI ALPS facility.

A temperature-controlled TAS setup was developed and implemented at the ELI ALPS facility. This modified system enabled stable and reproducible TAS measurements in CdSe/ZnS QD dispersions over the temperature range of 30–130 °C. We ensured no thermal degradation of the samples and performed precise tracking of temperature-dependent changes in charge carrier populations. Initial results confirmed that while the characteristic excited-state lifetimes remained largely unchanged (with $t_1 \approx 5$ ps and $t_2 \approx 250$ ps), the relative amplitudes of the decay components shifted significantly with temperature. This indicated that elevated temperatures primarily affect the distribution of carriers among different recombination channels, likely through enhanced nonradiative relaxation or trion formation. These findings demonstrate that the TAS system is well-suited for probing thermal effects on QD dynamics. The QD dispersion's high thermal stability and reproducibility were key to resolving subtle changes in population dynamics across the measured temperature range.

To further explore how composition influences relaxation dynamics, Ga-alloyed CdSe/ZnS QDs were investigated at three doping levels: 2.5%, 7.5%, and 15% Ga. Steady-state optical measurements revealed redshifted absorption and emission, while TAS data showed significantly prolonged decay times in the alloyed systems. Specifically, the excited-state lifetimes increased to $t_1 \approx 250$ ps and $t_2 \approx 750$ ps for the 7.5% Ga sample. The redistribution of decay amplitudes of the fast component A_1 decreases with growing temperature and a concurrent increase in A_2 suggests a growing role for trion-related processes in the presence of Ga. This is consistent with the onset of Coulomb blockade effects, where the accumulation of charges alters the potential landscape and slows carrier relaxation. These observations underscore the importance of compositional engineering in tailoring QD properties for specific optoelectronic applications. The findings suggest that Ga incorporation not only affects optical properties but also significantly modifies the carrier relaxation pathways, which confirms the relevance of alloying strategies in device optimization.

By altering the detection geometry of the setup, I extended the capabilities of the TAS setup at ELI ALPS to perform TRS measurements. The developed technique was used to reveal the exciton dynamics in different TMDC/pentacene thin film samples. While in liquid samples the probe light passes through the sample, in thin films, the reflected probe light must be collected effectively. The MoS_2 and WSe_2 monolayers were deposited on a gold substrate and covered with a 20 nm thick pentacene layer. TRS measurements successfully captured a 21 ± 3 ps decay component in MoS_2/pentacene heterojunctions associated with hole transfer. In the case of MoS_2/pentacene and WSe_2-pentacene heterojunctions, the presence of the pentacene film moderately influenced the decay kinetics of A and B excitons. The challenge in identifying specific decay components in the WSe_2 system highlights the complexity of carrier dynamics at TMDC/pentacene interfaces and suggests that further research is needed to fully understand them. Compared to TAS, the TRS approach required the development of new spatial filtering and alignment strategies to efficiently collect the reflected signal from the sample surface. This allowed us to study charge transfer and excitonic behavior in solid-state heterostructures with high sensitivity.

I studied how fundamental beam dispersion affects THz generation and found that controlling GDD and phase mismatch can optimize THz intensity. This is a key step for the future development of the TAS-THz probing setup. I studied the impact of GDD and phase mismatch on THz generation from two-color laser-induced air plasma. I demonstrated that optimal THz yield can be achieved by precisely controlling these parameters. The key findings showed that the THz intensity changed with the BBO crystal position and that GDD significantly affected both the shape and strength of the THz pulses. These insights are crucial for efficient THz radiation generation in the TAS setup at ELI ALPS, as the tunability of THz radiation is valuable for probing ultrafast carrier dynamics. The results revealed that GDD is a critical parameter in shaping the THz waveform and enhancing its intensity.

6. Magyar nyelvű összefoglaló

Az elmúlt években a kvantummechanika gyakorlati alkalmazása – különösen a fény és anyag kölcsönhatásának manipulálása – új kapukat nyitott az anyagtudományban és a fotonikában. A ultrarövid lézerimpulzusok keltésére és vizsgálatára alkalmas technológiák fejlődése lehetővé tette, hogy komplex fotofizikai és fotokémiai folyamatokat vizsgáljunk néhány femtoszekundumtól akár a nanoszekundumos időskáláig. Ezzel párhuzamosan az elektromágneses spektrum egyre több régióját sikerült vizsgálhatóvá tenni: míg korábban a látható és infravörös tartomány dominált, ma már a hosszú ideig technikailag elérhetetlen terahertzes (THz) frekvenciatartományban is képesek vagyunk precíz mérésekre. Érzékenysége miatt a THz-es sugárzás különösen alkalmas az alacsony energiájú kollektív gerjesztések, töltéshordozó-kölcsönhatások és sávszerkezet-dinamikák feltérképezésére, így fontos kiegészítője lett a modern spektroszkópiai módszereknek.

Doktori munkám során elsősorban a nanoszerkezetű anyagokban végbemenő ultragyors folyamatok megértésére törekedtem, különös tekintettel a töltéshordozó-dinamikára kvantumpontokban és kétdimenziós félvezetőkben. Azt vizsgáltam, hogy akülső paraméterek (pl. hőmérséklet, összetétel, határfelületi-kölcsönhatások) hogyan befolyásolják a töltéshordozók relaxációját, rekombinációját és átviteli mechanizmusait a femto- és pikoszekundumos időtartományban. Fő motivációm volt egy olyan kísérleti rendszer fejlesztése, ami képes különböző hőmérsékleteken a tranziens abszorpciós spektroszkópiai (TAS) mérések kivitelezésére. Ez az eszköz a pumpa–próba módszeren alapul, mely során egy rövid, intenzív pumpaimpulzus gerjeszti a vizsgált rendszert, míg egy késleltetett, széles sávú próbaimpulzus feltérképezi a keletkező gerjesztett állapotok időbeli lefolyását. A TAS különösen alkalmas olyan gyors fotofizikai folyamatok kinetikai jellemzőinek vizsgálatára, mint a töltéshordozók keletkezése és rekombinációja, gerjesztett állapotok relaxációja, elektron- és lyukcsapdázódás, ionizáció.

Kutatómunkám során egy olyan multifunkcionális mérőmódszert fejlesztettem ki, ami alkalmas lehet különböző vékonyrétegek vizsgálatára is, tehát nemcsak transzmisszióban, hanem reflexióban is – a minta felszínéről – is tud információt gyűjteni. Az új geometriai elrendezéssel és térszűréssel kiegészítve létrehoztam a rendszer tranziens reflexiós spektroszkópiai (TRS) üzemmódját. A műszer további fejlesztésének részeként az eddigi látható próbaforrás mellé kiépítettem egy THz-es tartományú próbakart is, amely lehetővé teszi, hogy a rendszer különböző hullámhosszakon – így a THz-es tartományban is – képes legyen mintavételezést végezni. Ez a bővítés jelentősen növeli a mérési módszer alkalmazhatóságát többféle anyagvizsgálati feladathoz.

Az ELI ALPS nagyismétlési frekvenciájú (HR, 100 kHz), CEP-stabil lézerrendszerének adottságai – mint a kiváló jel-zaj arány és a precíz időzítés – lehetővé teszik a TAS módszer hatékony alkalmazását még gyenge jelek esetén is. Ennek köszönhetően az általunk fejlesztett TAS nem csupán egy ismert mérési technika, hanem annak egy újgenerációs, továbbfejlesztett, felhasználóbarát változata, amely az ELI ALPS infrastruktúrája révén teljesen új kutatási területek megnyitására is alkalmas. A rendszer rugalmasan alakítható: a pumpa- és próbaforrások könnyen cserélhetők, a mintatípusok széles skálája vizsgálható, így ideálisan alkalmazható a felhasználói igények kiszolgálására a nemzetközi kutatóközösség számára.

A doktori képzésem alatt az ELI ALPS létesítményben kifejlesztésre és megvalósításra került egy hőmérsékletszabályozott TAS rendszer. Ez az átalakított eszköz lehetővé tette stabil és reprodukálható TAS mérések végzését CdSe/ZnS kvantumpont-diszperziókban, 30–130 °C hőmérséklet-tartományban. A mérések során elértük, hogy a minták ne szenvedjenek hőkárosodást, és pontosan nyomon követtük a hőmérsékletfüggő töltéshordozó-populáció változását. Az eredmények azt mutatták, hogy bár a gerjesztett állapotok élettartamai alapvetően nem változtak ($t_1 \approx 5$ ps és $t_2 \approx 250$ ps), a relatív hozzájárulásuk jelentősen megváltoztak a hőmérséklet emelkedésével. Ez arra utal, hogy a magasabb hőmérséklet elsősorban a töltéshordozók eloszlását befolyásolja a különböző rekombinációs csatornák között, feltehetően a nem-radiatív relaxáció vagy a trionképződés fokozódása révén. Ezek az eredmények igazolják, hogy a TAS rendszer alkalmas a kvantumpontok hőmérsékletfüggő dinamikájának vizsgálatára.

Annak érdekében, hogy az összetétel relaxációs dinamikára gyakorolt hatását is megértsük, gallium-ötvözött CdSe/ZnS kvantumpontokat vizsgáltam három különböző (2,5%, 7,5% és 15%) adalékolással. Az előzetes optikai mérések vörös eltolódást mutattak az abszorpciós és emissziós spektrumokban, míg a TAS adatok jelentősen hosszabb rekombinációs időket jeleztek az ötvözött rendszerekben. A 7,5%-os Ga-tartalmú minta esetén a gerjesztett állapotok élettartamai $t_1 \approx 250$ ps és $t_2 \approx 750$ ps értékre nőttek. A hőmérséklet hatására a rekombinációs amplitúdók eloszlása is módosult: a gyors komponens (A_1) aránya csökkent a, míg a lassú komponensé (A_2) nőtt, ami a trionok szerepének erősödésére utal a Ga jelenlétében. Ez összhangban van az ún. Coulomb-blokád kialakulásával, ahol a töltések felhalmozódása lassítja a relaxációt. Az eredmények alátámasztják, hogy a kvantumpontok anyagi összetételének hangolása meghatározó tényező az optoelektronikai alkalmazások szempontjából

A mérési rendszer geometriájának módosításával sikerült kiterjesztenem az ELI ALPS TAS rendszerének képességeit TRS mérések végzésére. Az így kialakított technikával különböző átmenetifém-dikalkogenid/pentacén vékonyrétegek exciton dinamikáját vizsgáltam. Míg folyadékmintáknál a próbafény áthalad a mintán, vékonyrétegeknél a visszaverődött fényt kell hatékonyan összegyűjteni. Kísérleteink során aranybevonatú hordozóra felvitt, 20 nm pentacén réteggel borított MoS_2 és WSe_2 monorétegeket vizsgáltunk. A TRS mérések sikeresen kimutattak egy 21 ± 3 ps időállandójú rekombinációs komponenst a MoS_2/pentacén heteroátmenetben, amelyet a lyuktranszferrel hoztunk összefüggésbe. A pentacén réteg mind a MoS_2/pentacén, mind a WSe_2/pentacén rendszerekben mérsékelten befolyásolta az A és B excitonok rekombinációs dinamikáját. A WSe_2 rendszerben egyes komponensek azonosításának nehézségei rámutatnak a átmenetifém-dikalkogenid/pentacén határfelületek töltéshordozó-dinamikájának komplexitására, amelyek további vizsgálatokat indokolnak.

Kutatómunkám során továbbá azt vizsgáltam, hogyan befolyásolja az alapvető nyalábdiszperzió a THz-es sugárzás keltés hatékonyságát. Kimutattam, hogy a GDD (Group Delay Dispersion) és a fázisillesztés szabályozásával optimalizálható a THz-es intenzitás. Ez kulcsfontosságú lépés a TAS–THz próba rendszer jövőbeli fejlesztéséhez. Kétszínű lézer által létrehozott plazmában keltett THz-es sugárzást vizsgáltam, és megmutattam, hogy a BBO kristály pozíciójának, illetve a GDD értékének pontos beállításával maximalizálható a keltett THz-es sugárzás. Az eredmények rávilágítottak arra, hogy a GDD jelentősen befolyásolja a THz-es impulzusok alakját és intenzitását. Ezek az ismeretek kulcsfontosságúak a TAS rendszerbe integrált hatékony THz-es sugárzás előállításához, mivel a THz-es sugárzás hangolhatósága kiemelten fontos az ultragyors töltéshordozó-dinamikai vizsgálatokban.

7. Acknowledgement

I would like to thank my supervisors, who have shaped my thinking and work ethic over the years. I am especially grateful to **Prof. Viktor Chikán,** whose trust from the very beginning gave me hope and opened the door to the ELI family. His scientific excellence, personal integrity and belief in me continue to inspire me both professionally and personally.

I am also sincerely thankful to **Dr. Gergely Samu**, who guided me through the final stages of this journey. His humility, precision, and generous support have had a lasting impact on me. I learn from him every day, and his experience and energy continue to shape how I see the future.

I am grateful to **Dr**. **Pavel A. Markeev**, who was our first user and a key collaborator in a highly successful measurement campaign, which gave me hands-on experience and to **Dr. Christopher Tuinenga**, whose careful sample preparation laid the groundwork for several of the results presented in this thesis.

I am also deeply indebted to my institutional supervisors, **Prof. Katalin Varjú** and **Prof. Péter Dombi**, for their support and for the opportunity to pursue my degree. I would also like to thank **Dr. Károly Mogyorósi**, whose kindness and support as a close colleague meant a lot to me. I would like to extend my sincere thanks to **Dr. Barnabás Gilicze, Dr. Roland Flender, Dr. Ádám Börzsönyi, Imre Seres**, and **Zsolt Bengery**, from whom I have learned not only precision but also practical problem-solving. I am truly thankful to **Judit Zelena** for her thoughtful and meticulous proofreading, and for her encouraging presence throughout the final stages of this work. I am deeply thankful to **Zita Váradi**, who took me under her wings and supported me with genuine care throughout my research career. I would also like to express my gratitude to **Vera Horváth** for always encouraging my scientific creativity. My heartfelt thanks go to all my **friends** and **colleagues** for their support and encouragement, especially to my close companions **Júlia Dudás**, **Izabella Zala**, **Dr. Csaba Vass**, and **Bálint Tóth**, whose motivation and friendship meant a great deal throughout this journey.

My heartfelt thanks go to my **husband**, whose love, patience, and insight gave me strength throughout. Working in a similar field, he truly understood the challenges I faced. I am also grateful to my **parents**; they never pressured me when the progress was slow but were always proud when I moved forward, and that meant the world to me.

8. References

1. Dowling, J. P. & Milburn, G. J. Quantum technology: the second quantum revolution. *Philosophical Transactions of the Royal Society of London. Series A: Mathematical, Physical and Engineering Sciences* **361**, 1655–1674 (2003).
2. Bawendi, M. G., Steigerwald, M. L. & Brus, L. E. The Quantum Mechanics of Larger Semiconductor Clusters ("Quantum Dots"). *Annu Rev Phys Chem* **41**, 477–496 (1990).
3. Steigerwald, M. L. & Brus, L. E. Synthesis, Stabilization, and Electronic Structure of Quantum Semiconductor Nanoclusters. *Annual Review of Materials Science* **19**, 471–495 (1989).
4. Hecht, J. Short history of laser development. *Optical Engineering* **49**, 091002 (2010).
5. Michelson, A. A. & Morley, E. W. On the relative motion of the Earth and the luminiferous ether. *Am J Sci* **s3-34**, 333–345 (1887).
6. Einstein, A. Zur Theorie der Lichterzeugung und Lichtabsorption. *Ann Phys* **325**, 199–206 (1906).
7. MAIMAN, T. H. Stimulated Optical Radiation in Ruby. *Nature* **187**, 493–494 (1960).
8. Szipöcs, R., Spielmann, C., Krausz, F. & Ferencz, K. Chirped multilayer coatings for broadband dispersion control in femtosecond lasers. *Opt Lett* **19**, 201 (1994).
9. Strickland, D. & Mourou, G. Compression of amplified chirped optical pulses. *Opt Commun* **55**, 447–449 (1985).
10. Krausz, F. & Ivanov, M. Attosecond physics. *Rev Mod Phys* **81**, 163–234 (2009).
11. Flash photolysis and spectroscopy. A new method for the study of free radical reactions. *Proc R Soc Lond A Math Phys Sci* **200**, 284–300 (1950).
12. Zewail, A. H. Femtochemistry: Atomic-Scale Dynamics of the Chemical Bond. *J Phys Chem A* **104**, 5660–5694 (2000).

13. Ragan, R., Min, K. S. & Atwater, H. A. Direct energy gap group IV semiconductor alloys and quantum dot arrays in SnxGe1−x/Ge and SnxSi1−x/Si alloy systems. *Materials Science and Engineering: B* **87**, 204–213 (2001).

14. Trindade, T., O'Brien, P. & Pickett, N. L. Nanocrystalline Semiconductors: Synthesis, Properties, and Perspectives. *Chemistry of Materials* **13**, 3843–3858 (2001).

15. Andrade, P. H. M. *et al.* Band gap analysis in MOF materials: Distinguishing direct and indirect transitions using UV–vis spectroscopy. *Appl Mater Today* **37**, 102094 (2024).

16. Geng, W. *et al.* Nonlinear photonics on integrated platforms. *Nanophotonics* **13**, 3253–3278 (2024).

17. Li, F., Zhang, Z., Wan, T., Zhang, H. & Chen, C. Synthesis of white laser source based on nonlinear frequency conversion with stimulated Raman adiabatic passage. *Opt Commun* **502**, 127427 (2022).

18. Cui, C., Liang, F., Lu, D., Yu, H. & Zhang, H. Phase-matching condition in rotatory nonlinear optics. *Phys Rev A (Coll Park)* **105**, 023512 (2022).

19. Ganeev, R. A., Kulagin, I. A., Ryasnyansky, A. I., Tugushev, R. I. & Usmanov, T. Characterization of nonlinear optical parameters of KDP, LiNbO3 and BBO crystals. *Opt Commun* **229**, 403–412 (2004).

20. Cui, C., Liang, F., Lu, D., Yu, H. & Zhang, H. Phase-matching condition in rotatory nonlinear optics. *Phys Rev A (Coll Park)* **105**, 023512 (2022).

21. Bhar, G. C., Chaudhary, A. K., Kumbhakar, P., Rudra, A. M. & Sabarwal, S. C. A comparative study of laser-induced surface damage thresholds in BBO crystals and effect of impurities. *Opt Mater (Amst)* **27**, 119–123 (2004).

22. Poudel, C. & Kaminski, C. F. Supercontinuum radiation in fluorescence microscopy and biomedical imaging applications. *Journal of the Optical Society of America B* **36**, A139 (2019).

23. Dudley, J. M., Genty, G. & Coen, S. Supercontinuum generation in photonic crystal fiber. *Rev Mod Phys* **78**, 1135–1184 (2006).

24. Geints, Y. E., Bulygin, A. D., Kompanets, V. O. & Chekalin, S. V. Supercontinuum saturation of a femtosecond laser filament in pressurized gases. *Opt Lett* **49**, 6033 (2024).

25. Grigutis, R., Tamošauskas, G., Jukna, V., Risos, A. & Dubietis, A. Supercontinuum generation and optical damage of sapphire and YAG at high repetition rates. *Opt Lett* **45**, 4507 (2020).

26. Kauranen, M. Freeing Nonlinear Optics from Phase Matching. *Science (1979)* **342**, 1182–1183 (2013).

27. Ashcom, J. B., Gattass, R. R., Schaffer, C. B. & Mazur, E. Numerical aperture dependence of damage and supercontinuum generation from femtosecond laser pulses in bulk fused silica. *Journal of the Optical Society of America B* **23**, 2317 (2006).

28. Campagnola, P. Second Harmonic Generation Imaging Microscopy: Applications to Diseases Diagnostics. *Anal Chem* **83**, 3224–3231 (2011).

29. Campagnola, P. J. & Loew, L. M. Second-harmonic imaging microscopy for visualizing biomolecular arrays in cells, tissues and organisms. *Nat Biotechnol* **21**, 1356–1360 (2003).

30. Born, M. *et al. Principles of Optics*. (Cambridge University Press, 1999). doi:10.1017/CBO9781139644181.

31. Cui, Y. *et al.* Spectral phase effects and control requirements of coherent beam combining for ultrashort ultrahigh intensity laser systems. *Appl Opt* **55**, 10124 (2016).

32. Schnedermann, C. *et al.* Ultrafast Tracking of Exciton and Charge Carrier Transport in Optoelectronic Materials on the Nanometer Scale. *J Phys Chem Lett* **10**, 6727–6733 (2019).

33. Gorostiza, P. & Isacoff, E. Y. Optical Switches for Remote and Noninvasive Control of Cell Signaling. *Science (1979)* **322**, 395–399 (2008).

34. Choi, J., Yang, C., Kim, J. & Ihee, H. Protein Folding Dynamics of Cytochrome *c* Seen by Transient Grating and Transient Absorption Spectroscopies. *J Phys Chem B* **115**, 3127–3135 (2011).

35. Berera, R., van Grondelle, R. & Kennis, J. T. M. Ultrafast transient absorption spectroscopy: principles and application to photosynthetic systems. *Photosynth Res* **101**, 105–118 (2009).

36. Liebel, M., Toninelli, C. & van Hulst, N. F. Room-temperature ultrafast nonlinear spectroscopy of a single molecule. *Nat Photonics* **12**, 45–49 (2018).

37. Borrego-Varillas, R., Ganzer, L., Cerullo, G. & Manzoni, C. Ultraviolet Transient Absorption Spectrometer with Sub-20-fs Time Resolution. *Applied Sciences* **8**, 989 (2018).

38. Donaldson, P. M., Strzalka, H. & Hamm, P. High sensitivity transient infrared spectroscopy: a UV/Visible transient grating spectrometer with a heterodyne detected infrared probe. *Opt Express* **20**, 12761 (2012).

39. Di Cicco, A. *et al.* Broadband optical ultrafast reflectivity of Si, Ge and GaAs. *Sci Rep* **10**, 17363 (2020).

40. Kaindl, R. A., Carnahan, M. A., Hägele, D., Lövenich, R. & Chemla, D. S. Ultrafast terahertz probes of transient conducting and insulating phases in an electron–hole gas. *Nature* **423**, 734–738 (2003).

41. Montanaro, A. *et al.* Visible pump–mid infrared pump–broadband probe: Development and characterization of a three-pulse setup for single-shot ultrafast spectroscopy at 50 kHz. *Review of Scientific Instruments* **91**, (2020).

42. Attar, A. R. *et al.* Femtosecond x-ray spectroscopy of an electrocyclic ring-opening reaction. *Science (1979)* **356**, 54–59 (2017).

43. Calegari, F. *et al.* Ultrafast electron dynamics in phenylalanine initiated by attosecond pulses. *Science (1979)* **346**, 336–339 (2014).

44. Li, S. *et al.* Attosecond-pump attosecond-probe x-ray spectroscopy of liquid water. *Science (1979)* (2024) doi:10.1126/science.adn6059.

45. Liu, J., Li, Y., Hou, Y., Wu, J. & Yuan, J. Transient responses of double core-holes generation in all-attosecond pump-probe spectroscopy. *Sci Rep* **14**, 1950 (2024).

46. Di Palo, N. *et al.* Attosecond absorption and reflection spectroscopy of solids. *APL Photonics* **9**, (2024).

47. Lin, M.-F. *et al.* Carrier-Specific Femtosecond XUV Transient Absorption of PbI_2 Reveals Ultrafast Nonradiative Recombination. *The Journal of Physical Chemistry C* **121**, 27886–27893 (2017).

48. Schultze, M. *et al.* Attosecond band-gap dynamics in silicon. *Science (1979)* **346**, 1348–1352 (2014).

49. Fresch, E. *et al.* Two-dimensional electronic spectroscopy. *Nature Reviews Methods Primers* **3**, 84 (2023).

50. Collini, E. Spectroscopic signatures of quantum-coherent energy transfer. *Chem Soc Rev* **42**, 4932 (2013).

51. Vossmeyer, T. *et al.* CdS Nanoclusters: Synthesis, Characterization, Size Dependent Oscillator Strength, Temperature Shift of the Excitonic Transition Energy, and Reversible Absorbance Shift. *J Phys Chem* **98**, 7665–7673 (1994).

52. Liptay, T. J. & Ram, R. J. Temperature dependence of the exciton transition in semiconductor quantum dots. *Appl Phys Lett* **89**, (2006).

53. Dai, Q. *et al.* Size-Dependent Temperature Effects on PbSe Nanocrystals. *Langmuir* **26**, 11435–11440 (2010).

54. Milot, R. L., Eperon, G. E., Snaith, H. J., Johnston, M. B. & Herz, L. M. Temperature-Dependent Charge-Carrier Dynamics in $CH_3NH_3PbI_3$ Perovskite Thin Films. *Adv Funct Mater* **25**, 6218–6227 (2015).

55. Gélvez-Rueda, M. C., Renaud, N. & Grozema, F. C. Temperature Dependent Charge Carrier Dynamics in Formamidinium Lead Iodide Perovskite. *The Journal of Physical Chemistry C* **121**, 23392–23397 (2017).

56. Mehmood, A., Silfies, M. C., Durden, A. S., Allison, T. K. & Levine, B. G. Simulating ultrafast transient absorption spectra from first principles using a time-dependent configuration interaction probe. *J Chem Phys* **161**, (2024).

57. Sauter, E., Abrosimov, N. V., Hübner, J. & Oestreich, M. Temperature dependence of the band gap of <math> <mmultiscripts> <mi>Si</mi> <mprescripts/> <none/> <mn>28</mn> </mmultiscripts> </math> :P at very low temperatures measured via time-resolved optical spectroscopy. *Phys Rev Res* **5**, 013182 (2023).

58. Sauter, E., Abrosimov, N. V., Hübner, J. & Oestreich, M. Low Temperature Relaxation of Donor Bound Electron Spins in <math display="inline"> <mrow> <mmultiscripts> <mrow> <mi>Si</mi> </mrow> <mprescripts/> <none/> <mrow> <mn>28</mn> </mrow> </mmultiscripts> <mo>:</mo> <mi mathvariant="normal">P</mi> </mrow> </math>. *Phys Rev Lett* **126**, 137402 (2021).

59. Utterback, J. K., Ruzicka, J. L., Hamby, H., Eaves, J. D. & Dukovic, G. Temperature-Dependent Transient Absorption Spectroscopy Elucidates Trapped-Hole Dynamics in CdS and CdSe Nanorods. *J Phys Chem Lett* **10**, 2782–2787 (2019).

60. Sabatini, R. P. *et al.* Temperature-Induced Self-Compensating Defect Traps and Gain Thresholds in Colloidal Quantum Dots. *ACS Nano* **13**, 8970–8976 (2019).

61. Rowland, C. E. *et al.* Elevated Temperature Photophysical Properties and Morphological Stability of CdSe and CdSe/CdS Nanoplatelets. *J Phys Chem Lett* **9**, 286–293 (2018).

62. Wilson, W. L., Szajowski, P. F. & Brus, L. E. Quantum Confinement in Size-Selected, Surface-Oxidized Silicon Nanocrystals. *Science (1979)* **262**, 1242–1244 (1993).

63. Murray, C. B., Norris, D. J. & Bawendi, M. G. Synthesis and characterization of nearly monodisperse CdE (E = sulfur, selenium, tellurium) semiconductor nanocrystallites. *J Am Chem Soc* **115**, 8706–8715 (1993).

64. Ahn, N. *et al.* Electrically driven amplified spontaneous emission from colloidal quantum dots. *Nature* **617**, 79–85 (2023).

65. color of QDs.

66. Tvrdy, K., Frantsuzov, P. A. & Kamat, P. V. Photoinduced electron transfer from semiconductor quantum dots to metal oxide nanoparticles. *Proceedings of the National Academy of Sciences* **108**, 29–34 (2011).

67. Efros, Al. L. *et al.* Band-edge exciton in quantum dots of semiconductors with a degenerate valence band: Dark and bright exciton states. *Phys Rev B* **54**, 4843–4856 (1996).

68. Morgan, D. P. & Kelley, D. F. What Does the Transient Absorption Spectrum of CdSe Quantum Dots Measure? *The Journal of Physical Chemistry C* **124**, 8448–8455 (2020).

69. Sercel, P. C. & Efros, A. L. Band-Edge Exciton in CdSe and Other II–VI and III–V Compound Semiconductor Nanocrystals − Revisited. *Nano Lett* **18**, 4061–4068 (2018).

70. Vong, A. F., Irgen-Gioro, S., Wu, Y. & Weiss, E. A. Origin of Low Temperature Trion Emission in CdSe Nanoplatelets. *Nano Lett* **21**, 10040–10046 (2021).

71. Pandya, R. *et al.* Fine Structure and Spin Dynamics of Linearly Polarized Indirect Excitons in Two-Dimensional CdSe/CdTe Colloidal Heterostructures. *ACS Nano* **13**, 10140–10153 (2019).

72. Norris, D. Electronic Structure in Semiconductor Nanocrystals. in *Nanocrystal Quantum Dots, Second Edition* 63–96 (CRC Press, 2010). doi:10.1201/9781420079272-c2.

73. Keene, J. D., Freymeyer, N. J., McBride, J. R. & Rosenthal, S. J. Ultrafast spectroscopy studies of carrier dynamics in semiconductor nanocrystals. *iScience* **25**, 103831 (2022).

74. Tuinenga, C. J. *INDIUM, TIN, AND GALLIUM DOPED CDSE QUANTUM DOTS*. (2004).

75. Luo, H. *et al.* Synthesis and characterization of gallium-doped CdSe quantum dots. *Journal of Physical Chemistry C* **119**, 10749–10757 (2015).

76. Lenngren, N. *et al.* Hot electron and hole dynamics in thiol-capped CdSe quantum dots revealed by 2D electronic spectroscopy. *Physical Chemistry Chemical Physics* **18**, 26199–26204 (2016).

77. Honarfar, A. *et al.* Photoexcitation Dynamics in Electrochemically Charged CdSe Quantum Dots: From Hot Carrier Cooling to Auger Recombination of Negative Trions. *ACS Appl Energy Mater* **3**, 12525–12531 (2020).

78. Guo, J. *et al.* Ultrafast carrier dynamics in CdS@CdSe core-shell quantum dot heterostructure. *Opt Mater (Amst)* **128**, (2022).

79. Hines, M. A. & Guyot-Sionnest, P. *Synthesis and Characterization of Strongly Luminescing ZnS-Capped CdSe Nanocrystals*. (1996).

80. Owen, J. & Brus, L. Chemical Synthesis and Luminescence Applications of Colloidal Semiconductor Quantum Dots. *Journal of the American Chemical Society* vol. 139 10939–10943 Preprint at https://doi.org/10.1021/jacs.7b05267 (2017).

81. Barak, Y., Meir, I., Shapiro, A., Jang, Y. & Lifshitz, E. Fundamental Properties in Colloidal Quantum Dots. *Advanced Materials* vol. 30 Preprint at https://doi.org/10.1002/adma.201801442 (2018).

82. Pandey, A. & Guyot-Sionnest, P. Slow electron cooling in colloidal quantum dots. *Science (1979)* **322**, 929–932 (2008).

83. Liang, Z. *et al.* Effects of Tellurium Doping on Environmental Stability and Luminous Performance of $CsPbBr_3$ Quantum Dots. *ACS Omega* **7**, 21800–21807 (2022).

84. Dabbousi, B. O. *et al.* (CdSe)ZnS Core−Shell Quantum Dots: Synthesis and Characterization of a Size Series of Highly Luminescent Nanocrystallites. *J Phys Chem B* **101**, 9463–9475 (1997).

85. Zhang, L., Xiang, W. & Zhang, J. Thick-Shell Core/Shell Quantum Dots. in 197–218 (2020). doi:10.1007/978-3-030-46596-4_6.

86. Tian, Y., Newton, T., Kotov, N. A., Guldi, D. M. & Fendler, J. H. Coupled Composite CdS−CdSe and Core−Shell Types of (CdS)CdSe and (CdSe)CdS Nanoparticles. *J Phys Chem* **100**, 8927–8939 (1996).

87. Danek, M., Jensen, K. F., Murray, C. B. & Bawendi, M. G. Synthesis of Luminescent Thin-Film CdSe/ZnSe Quantum Dot Composites Using CdSe Quantum Dots Passivated with an Overlayer of ZnSe. *Chemistry of Materials* **8**, 173–180 (1996).

88. Youn, H. C., Baral, S. & Fendler, J. H. Dihexadecyl phosphate, vesicle-stabilized and in situ generated mixed cadmium sulfide and zinc sulfide semiconductor particles: preparation and utilization for photosensitized charge separation and hydrogen generation. *J Phys Chem* **92**, 6320–6327 (1988).

89. Kortan, A. R. *et al.* Nucleation and Growth of CdSe on ZnS Quantum Crystallite Seeds, and Vice Versa, in Inverse Micelle Media. *J Am Chem Soc* **112**, 1327–1332 (1990).

90. Shockley, W. & Queisser, H. J. Detailed Balance Limit of Efficiency of *p-n* Junction Solar Cells. *J Appl Phys* **32**, 510–519 (1961).

91. Nelson, C. A., Monahan, N. R. & Zhu, X.-Y. Exceeding the Shockley–Queisser limit in solar energy conversion. *Energy Environ Sci* **6**, 3508 (2013).

92. Ross, R. T. & Nozik, A. J. Efficiency of hot-carrier solar energy converters. *J Appl Phys* **53**, 3813–3818 (1982).

93. Yu, X.-Y., Liao, J.-Y., Qiu, K.-Q., Kuang, D.-B. & Su, C.-Y. Dynamic Study of Highly Efficient CdS/CdSe Quantum Dot-Sensitized Solar Cells Fabricated by Electrodeposition. *ACS Nano* **5**, 9494–9500 (2011).

94. Yu, J. & Chen, R. Optical properties and applications of two-dimensional CdSe nanoplatelets. *InfoMat* **2**, 905–927 (2020).

95. Sippel, P. *et al.* Femtosecond Cooling of Hot Electrons in CdSe Quantum-Well Platelets. *Nano Lett* **15**, 2409–2416 (2015).

96. Wang, J. *et al.* Spin blockade and phonon bottleneck for hot electron relaxation observed in n-doped colloidal quantum dots. *Nat Commun* **12**, 550 (2021).

97. Hopper, T. R. *et al.* Ultrafast Intraband Spectroscopy of Hot-Carrier Cooling in Lead-Halide Perovskites. *ACS Energy Lett* **3**, 2199–2205 (2018).

98. Chen, J., Messing, M. E., Zheng, K. & Pullerits, T. Cation-Dependent Hot Carrier Cooling in Halide Perovskite Nanocrystals. *J Am Chem Soc* **141**, 3532–3540 (2019).

99. Li, M. *et al.* Slow cooling and highly efficient extraction of hot carriers in colloidal perovskite nanocrystals. *Nat Commun* **8**, 14350 (2017).

100. Yang, Y. *et al.* Observation of a hot-phonon bottleneck in lead-iodide perovskites. *Nat Photonics* **10**, 53–59 (2016).

101. Yang, J. *et al.* Acoustic-optical phonon up-conversion and hot-phonon bottleneck in lead-halide perovskites. *Nat Commun* **8**, 14120 (2017).

102. Roy, S. *et al.* Progress toward producing n-type CdSe quantum dots: Tin and indium doped CdSe quantum dots. *Journal of Physical Chemistry C* **113**, 13008–13015 (2009).

103. Roy, P. & Srivastava, S. K. In situ deposition of Sn-doped CdS thin films by chemical bath deposition and their characterization. *J Phys D Appl Phys* **39**, 4771–4776 (2006).

104. Tuinenga, C., Jasinski, J., Iwamoto, T. & Chikan, V. In situ observation of heterogeneous growth of CdSe quantum dots: Effect of indium doping on the growth kinetics. *ACS Nano* **2**, 1411–1421 (2008).

105. Perna, G., Capozzi, V., Minafra, A., Pallara, M. & Ambrico, M. Effects of the indium doping on structural and optical properties of CdSe thin films deposited by laser ablation technique. *European Physical Journal B* **32**, 339–344 (2003).

106. Wang, L. *et al.* Observation of a phonon bottleneck in copper-doped colloidal quantum dots. *Nat Commun* **10**, 4532 (2019).

107. Lott, K. *et al.* High-temperature investigation of ZnS:Ga and CdSe:Ga. in *Physica B: Condensed Matter* vols. 376–377 764–766 (2006).

108. Yang, G. *et al.* Size-dependent Auger recombination in CdSe quantum dots studied by transient absorption spectroscopy. *Journal of the Chinese Chemical Society* **68**, 2054–2059 (2021).

109. Wang, X., Yu, J. & Chen, R. Optical Characteristics of ZnS Passivated CdSe/CdS Quantum Dots for High Photostability and Lasing. *Sci Rep* **8**, 17323 (2018).

110. de Mello Donegá, C., Bode, M. & Meijerink, A. Size- and temperature-dependence of exciton lifetimes in CdSe quantum dots. *Phys Rev B* **74**, 085320 (2006).

111. Alexeev, E. M. *et al.* Imaging of Interlayer Coupling in van der Waals Heterostructures Using a Bright-Field Optical Microscope. *Nano Lett* **17**, 5342–5349 (2017).

112. Wang, T. *et al.* Hot Carrier Cooling and Trapping in Atomically Thin WS $_2$ Probed by Three-Pulse Femtosecond Spectroscopy. *ACS Nano* **17**, 6330–6340 (2023).

113. Das, S., Wang, Y., Dai, Y., Li, S. & Sun, Z. Ultrafast transient sub-bandgap absorption of monolayer MoS2. *Light Sci Appl* **10**, 27 (2021).

114. Cui, Q., Ceballos, F., Kumar, N. & Zhao, H. Transient Absorption Microscopy of Monolayer and Bulk WSe $_2$. *ACS Nano* **8**, 2970–2976 (2014).

115. Charalambidis, D. *et al.* The Extreme Light Infrastructure—Attosecond Light Pulse Source (ELI-ALPS) Project. in 181–218 (2017). doi:10.1007/978-3-319-64840-8_10.

116. Hädrich, S. *et al.* Carrier-envelope phase stable few-cycle laser system delivering more than 100 W, 1 mJ, sub-2-cycle pulses. *Opt Lett* **47**, 1537 (2022).

117. Cumberland, S. L. *et al.* Inorganic Clusters as Single-Source Precursors for Preparation of CdSe, ZnSe, and CdSe/ZnS Nanomaterials. *Chemistry of Materials* **14**, 1576–1584 (2002).

118. Thupakula, U., Khan, A. H., Bal, J. K., Ariga, K. & Acharya, S. Size Selective Excitonic Transition Energies in Strongly Confined CdSe Quantum Dots. *J Nanosci Nanotechnol* **11**, 7709–7714 (2011).

119. Wang, C., Wehrenberg, B. L., Woo, C. Y. & Guyot-Sionnest, P. Light Emission and Amplification in Charged CdSe Quantum Dots. *J Phys Chem B* **108**, 9027–9031 (2004).

120. Vishnu, E. K., Kumar Nair, A. A. & Thomas, K. G. Core-Size-Dependent Trapping and Detrapping Dynamics in CdSe/CdS/ZnS Quantum Dots. *The Journal of Physical Chemistry C* **125**, 25706–25716 (2021).

121. Cohn, A. W., Rinehart, J. D., Schimpf, A. M., Weaver, A. L. & Gamelin, D. R. Size Dependence of Negative Trion Auger Recombination in Photodoped CdSe Nanocrystals. *Nano Lett* **14**, 353–358 (2014).

122. Tauc, J., Grigorovici, R. & Vancu, A. Optical Properties and Electronic Structure of Amorphous Germanium. *physica status solidi (b)* **15**, 627–637 (1966).

123. Roy, D., Samu, G. F., Hossain, M. K., Janáky, C. & Rajeshwar, K. On the measured optical bandgap values of inorganic oxide semiconductors for solar fuels generation. *Catal Today* **300**, 136–144 (2018).

124. Markeev, P. A. *et al.* Exciton Dynamics in MoS $_2$ -Pentacene and WSe $_2$ -Pentacene Heterojunctions. *ACS Nano* **16**, 16668–16676 (2022).

125. Kim, K. Y., Taylor, A. J., Glownia, J. H. & Rodriguez, G. Coherent control of terahertz supercontinuum generation in ultrafast laser–gas interactions. *Nat Photonics* **2**, 605–609 (2008).

126. Kim, K.-Y., Glownia, J. H., Taylor, A. J. & Rodriguez, G. High-Power Broadband Terahertz Generation via Two-Color Photoionization in Gases. *IEEE J Quantum Electron* **48**, 797–805 (2012).

9. Appendix

Table A1. Parameters of a tri-exponential function fitted to the PL decay curves of CdSe/ZnS QDs in pristine, CdSe:2.5% Ga/ZnS, CdSe:7.5% Ga/ZnS and CdSe:15% Ga/ZnS alloyed samples.

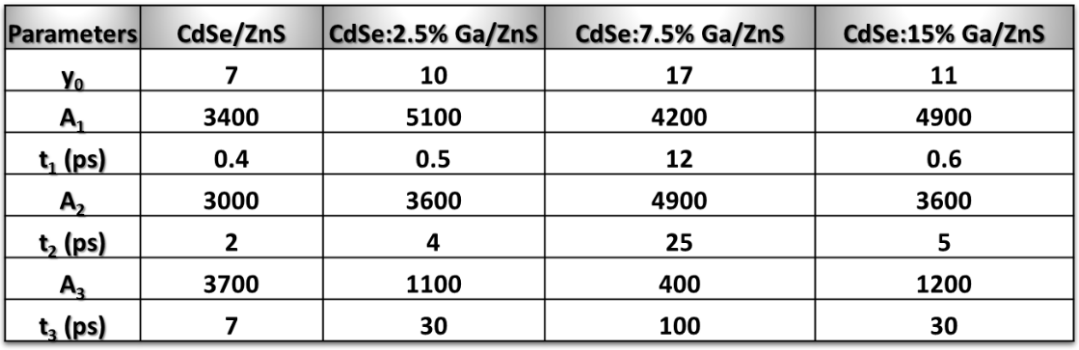

Parameters	CdSe/ZnS	CdSe:2.5% Ga/ZnS	CdSe:7.5% Ga/ZnS	CdSe:15% Ga/ZnS
y_0	7	10	17	11
A_1	3400	5100	4200	4900
t_1 (ps)	0.4	0.5	12	0.6
A_2	3000	3600	4900	3600
t_2 (ps)	2	4	25	5
A_3	3700	1100	400	1200
t_3 (ps)	7	30	100	30

Table A2. Parameters of a biexponential function fitted TAS decay trace of CdSe/ZnS QDs.

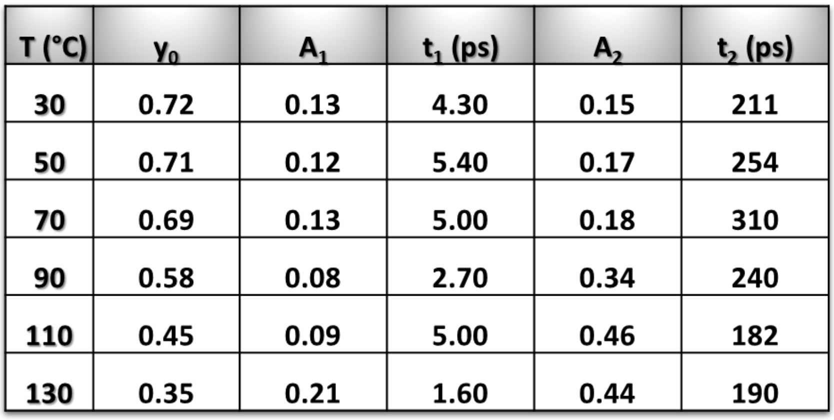

T (°C)	y_0	A_1	t_1 (ps)	A_2	t_2 (ps)
30	0.72	0.13	4.30	0.15	211
50	0.71	0.12	5.40	0.17	254
70	0.69	0.13	5.00	0.18	310
90	0.58	0.08	2.70	0.34	240
110	0.45	0.09	5.00	0.46	182
130	0.35	0.21	1.60	0.44	190

Table A3. Parameters of a biexponential function fitted to the TAS decay trace of CdSe:2.5% Ga/ZnS QDs.

T(°C)	y_0	A_1	t_1 (ps)	A_2	t_2 (ps)
30	0.70	0.06	17.00	0.23	425
50	0.68	0.05	22.9	0.26	455
70	0.63	0.05	18.00	0.31	528
90	0.54	0.06	10.50	0.38	492
110	0.47	0.09	19.00	0.44	608
130	0.40	0.11	9.17	0.47	476

Table A4. Parameters of a biexponential function fitted to the TAS decay trace of CdSe:7.5% Ga/ZnS QDs.

T (°C)	y_0	A_1	t_1 (ps)	A_2	t_2 (ps)
30	0.76	0.17	288	0.05	1230
50	0.66	0.24	300	0.08	784
70	0.56	0.15	251	0.26	769
90	0.52	0.25	336	0.16	641
110	0.40	0.22	79.0	0.21	79.0
130	0.43	0.16	372	0.16	455

Table A5. Parameters of a monoexponential function fitted to the TAS decay trace of CdSe:15% Ga/ZnS QDs.

T(°C)	y_0	A_1	t_1 (ps)
30	0.79	0.14	274
70	0.68	0.2	363
90	0.57	0.24	227
110	0.58	0.25	310
130	0.41	0.54	417